Locality and fluctuation effects in ionic liquids

Dissertation
zur
Erlangung des Doktorgrades (Dr. rer. nat.)
der
Mathematisch-Naturwissenschaftlichen Fakultät
der
Rheinischen Friedrich-Wilhelms-Universität Bonn

vorgelegt von

Wenbo Dong

aus
Panjin, China

Bonn
2025

Angefertigt mit Genehmigung der Mathematisch-Naturwissenschaftlichen Fakultät der
Rheinischen Friedrich-Wilhelms-Universität Bonn

Gutachterin/Betreuerin:	Prof. Dr. Barbara Kirchner
Gutachter:	Prof. Dr. Thomas Bredow

Tag der Promotion: 28.08.2025

Erscheinungsjahr: 2025

Me: Through scientific research,
I can always see the world with fresh eyes, even in the monotony of life.

Publications

Parts of this thesis have already been published in peer-reviewed journals:

1. **W. Dong**, V. Alizadeh, J. Blasius, L. Wylie, L. Dick, Z. Fan, B. Kirchner, "Locality in Amino-Acid Based Imidazolium Ionic Liquids", *Phys. Chem. Chem. Phys.* **2023**, *25*, 24678-24685, DOI:10.1039/D3CP02671J.

2. **W. Dong**, J. Blasius, Z. Fan, L. Wylie, "Vibrational Spectra Simulations in Amino Acid-Based Imidazolium Ionic Liquids", *J. Phys. Chem. B* **2024**, *128*, 6560–6566, DOI:10.1021/acs.jpcb.4c02555.

3. **W. Dong**, P. R. Batista, J. Blasius, B. Kirchner, "Aromatic-Aromatic Interactions and Hydrogen Bonding in Amino Acid Based Ionic Liquids", *Phys. Chem. Chem. Phys.* **2025**, *27*, 4457-4466, DOI:10.1039/D4CP04385E.

Presentations and posters on conferences and workshops:

1. Poster on "Locality and Fluctuation Effects in Amino Acid Based Ionic Liquids" at *Exploring Reactivity with Spectroscopy, ExpRes 2021.* online

2. Poster on "Locality and Fluctuation Effects in Amino Acid (AA) Based Ionic Liquids (ILs)," at *Advanced Catalysis and Materials for Energy Conversion, ACAMEC 2023.* in Muelheim, 2023

3. Poster on "Locality and Fluctuation Effects in Amino Acid (AA) Based Ionic Liquids (ILs)," at *Spectroscopy and Electronic Structure of Transition Metal Complexes* in Gelsenkirchen, 2023

4. Poster on "Locality and Fluctuation Effects in Amino-Acid Based Imidazolium Ionic Liquids" at *The International Symposium on Machine Learning in Quantum Chemistry MolSim2022* in Uppsala, 2023

Abstract

Amino acid (AA) based imidazolium ionic liquids (ILs) have shown broad application potential in biocatalysis, electrochemistry, drug delivery and green solvents due to their low volatility, high thermal stability and good solubility. However, the microstructure and interactions of ILs are complex, involving charge transfer, polarization effects, hydrogen bonds (HB), and π-π interactions between ions. Therefore, accurate characterization of their physical and chemical properties is crucial to optimizing their performance. The traditional classical force field molecular dynamics (MD) method has limitations in describing electronic polarization and charge transfer, while the *ab initio* molecular dynamics (AIMD) based on first principles has become a powerful tool for studying the polarization, spectral and structural properties of ILs since it can dynamically simulate electronic structure. This paper combines three part studies to systematically explore the application of AIMD in the study of AA-ILs, focusing on analyzing their polarization behavior, vibrational spectral characteristics, and intermolecular interaction mechanisms.

AA-ILs exhibit a more complex charge distribution compared with traditional imidazolium ILs due to the presence of amino acid side chains. In Chapter 3, AIMD is used in combination with different charge distribution schemes (Wannier function, Blöchl, Löwdin and Mulliken charge schemes and Voronoi tessellation) to calculate the electronic polarization effect. The results show that the Wannier localization method can more accurately describe the charge transfer phenomenon, while the Mulliken and Voronoi partitioning methods have different performances in different ion combinations. Through comparative analysis of multiple ILs systems, the study found that the π-electron cloud distribution of the cationic imidazolium ring plays a key role in the polarization process, while anions have relatively small contributions to the overall charge rearrangement due to their low polarizability.

Infrared (IR) and Raman spectroscopy are important experimental methods for studying the intermolecular forces and structural information of ILs, but traditional calculation methods have certain errors in the prediction of peak positions and intensities. In Chapter 4, the time-dependent dipole moment autocorrelation function of ILs is calculated by AIMD to simulate the IR spectrum, and the maximum localized Wannier function and Voronoi method are used to optimize the accuracy of spectral calculation. The study found that the two methods have good consistency in the relative intensity of characteristic peaks and overall profiles, but the Voronoi method reduces unstable factors during time evolution, making its calculation results smoother and easier to match with experimental data. In addition, the C-H stretching vibration of the imidazolium ring, the CO vibration of the AA side chain, and the vibration mode of the hydrogen bond (HB) inside ILs were clearly analyzed, providing a new theoretical basis for the

molecular recognition, interaction and environmental response of ILs.

The physicochemical properties of ILs are largely affected by their intermolecular interactions. In Chapter 5, AIMD was used to calculate the radial distribution functions (RDFs) and the combine distribution functions (CDF), and the short-range and long-range interaction patterns of imidazolium ILs were systematically analyzed. The results show that the HB between cations and anions (such as N-H···O and C-H···F) plays a decisive role in the stability of the system, while the π-π stacking effect of the imidazole ring significantly affects the structural order and fluidity of ILs. In addition, the presence of different amino acid side chains leads to differences in the local structure of ILs. For example, ILs with carboxyl groups tend to form a stable HB network, while ILs with phenyl side chains show a strong intermolecular stacking effect due to the π-π interaction. These structural features not only affect the viscosity, diffusivity and solvation ability of ILs, but also play an important role when ILs act as protein stabilizers or catalytic mediators.

This thesis combines three parts to systematically analyze the polarization effect, vibrational spectral characteristics and intermolecular interactions of AA-ILs, demonstrating the importance of AIMD in ILs research. Through high-precision calculation methods, we revealed the microscopic mechanism of electronic polarization in ILs systems, optimized spectral calculation methods, and deeply explored key interactions such as HB and π-π stacking. These research results not only provide contribute to the fundamental theoretical understanding of ILs, but also provide important references for their application design in biochemistry, electrochemistry and materials science.

Contents

1. Introduction

1.1. Ionic liquids

In the past three decades of development, due to the diversification of material applications, ionic liquids (ILs) have gradually been used as an optimal and designable solvent, rather than just a substitute for traditional organic solvent media.[1–3] ILs are defined as salts with melting temperatures below 100 °C, and are comprised entirely of cations and anions.[4,5] The initial report of a room-temperature molten salt dates back to 1914.[6,7] Ethylammonium nitrate was found to have a melting point of 12 °C. Later the widespread interest of ILs started from organic chloroaluminates, which have limited applicability since the starting materials and IL products are moisture sensitive.[8] Organic chloroaluminates are usually considered to be the first generation ILs. During the mid-to-late 20th century, ILs were extensively investigated especially as electrolytes in batteries.[9,10] Here, heterocyclic cations such as pyridinium and imidazolium were combined with tetrachloroaluminate anions to produce liquid salts. During the 1990s, the most commonly found salts (with hexafluorophosphate, tetrafluoroborate, nitrate or methanesulfonate as the anion) were prepared, characterized and evaluated, which comparing to products from decades ago did not need the moisture-related considerations.[11–13] In 1996, the first industrial process incorporating ILs was announced, the Texas Eastman Division of Eastman Chemical Company isomerized 3,4-epoxy-1-butene into 2,5-dihydrofuran, and since then research on ILs has boomed.[14,15] Until now, the categories of ILs are generally aprotic ILs (which make up the majority); protic ILs (formed by transfer of protons from pure acids and bases); inorganic ILs (which can be obtained in both aprotic and protic forms) and solvated ILs.[13] Currently, the more commonly studied ILs include imidazolium, pyridinium, pyrrolidinium, tetraalkylammonium and tetraalkylphosphonium as cations, and trifluoromethanesulfonate, dicyanamide, p-toluenesulfonate, tetrafluoroborate and hexafluorophosphate as anions.[16]

ILs can be comprised of many combinations of cations and anions, they offer a high degree of customization for individual applications, with an estimated potential of at least 1 million binary and 10^{18} ternary ILs combinations.[17] Simultaneously, the ability to design ILs to satisfy the different physical properties required for each application by selecting appropriate cations and anions has made the study of ILs extremely attractive over the past three decades.[18] ILs are becoming increasingly popular both within academic research and industrial applications.[19] Their unique properties, including low volatility, make them advantageous for applications in diverse fields such as synthesis, catalysis, biocatalysis, separation technology, electrochemistry, analytical chemistry, and nanotechnology.[18] Currently, many countries and regions are increasingly focusing on research into ILs, driven by the growing demand for environmental protection

and sustainable resource management. In the field of sustainable chemistry, research into ILs has significant potential and many relevant applications.[20,21] Since ILs are nonvolatile and non-flammable, they can be used as effective solvents with the advantages of high recyclability, easy control and product recovery.[18] Therefore, it is important to understand the physical properties of ILs so that they can be used as suitable solvents in various situations.

ILs exhibit strong ionic interactions as a fundamental characteristic, which distinguishes them from high-temperature molten salts.[22] ILs can display distinctive characteristics compared to conventional solvents,[23] particularly their propensity to engage in a variety of attractive interactions, including van der Waals forces,[24] dispersion forces[25] and solvophobic effects,[26] as well as specific and anisotropic forces such as hydrogen bonds (HB),[27] halogen bonding,[28] dipole–dipole interactions,[29] and magnetic dipole interactions. In ionic compounds, the main force of interaction between anions and cations is Coulombic attraction.[30] In addition, HB and dispersion forces are crucial to elucidating the unique properties of ILs.[5] The strong anion-cation interactions present in these Coulombic fluids manifest through notable low vapor pressures and high enthalpies of vaporization.[31–33] It is observed that the magnitude of the interaction energy between ions is highly dependent on the charge density.[34] Charge density, in turn, depends on the size and distribution of charges associated with both anions and cations.

Understanding the properties of ILs at the molecular level will greatly promote the application of ILs in rational design and other directions. However, understanding ILs at the molecular level is a huge challenge because the charge and molecular electronic structures of ions give rise to complex molecular interactions. To gain a fundamental understanding, theoretical calculations are often applied on the liquid-gas interface of different solutions (including ILs). These studies have analyzed a variety of different properties,[35–39] such as structure analysis of the liquid-gas interface in the IL ($[C_4C_1Im][PF_6]$) in a study by Bhargava *et al.*[40] or the surface tension of the liquid-vapor interface for alcohols.[41] With the exponential growth of available computer resources, the interest in molecular dynamics (MD) and Monte Carlo (MC) simulations has grown in recent decades, making them an indispensable standard method in computational chemistry today.[42–44] Computational chemistry can simulate complex and realistic chemical systems and even provide insights into properties that are not accessible experimentally. Historically, MD simulation has played a key role in confirming fluid state theories as one of the most powerful tools in engineering and science in understanding the behavior of fluids and materials at the atomistic level.[45,46] Computational simulation can provide a molecular level view into the relationship between macroscopic and microscopic properties, and provide deeper insights into the ILs properties.[47] Given the limitations of experiments, molecular simulations are well suited to explore the properties and structural interactions of ILs at the molecular level.[48] Both the thermodynamics and kinetics of reactions conducted in ILs exhibit differences when compared to those observed in conventional molecular solvents.[18] Several previous studies have employed the density functional theory (DFT) based *ab initio* molecular dynamics (AIMD) method to investigate ILs and compute their key physical properties.[49–51] In particular, the calculated physical properties have included the study of the structure of the liquid gas-interface.[52] In addition, the electric dipole moment of an ion serves as a physical indicator of its electronic structure in ILs

with electric dipole moment fluctuations being dependent on polarization.[53]
A vast majority of amino acids (AAs) are chiral, has two chemically active centers suitable for modification, and has strong HB ability. These properties make AA-ILs more suitable as chiral solvents to dissolve and stabilize biomolecules than traditional ILs, which is crucial in medicine, synthesis, and medicinal chemistry.[54–58] Several AA-ILs have been identified, particularly those derived from the 20 natural L-AAs. Typically, the cations in AA-ILs are chosen including tetrabutylphosphonium,[59] tetrabutylammonium,[60] cholinium,[61] 1-butyl-3-methylimidazolium[62] and 1-ethyl-3-methylimidazolium.[63,64] MD simulations and quantum chemical calculations provide a deep understanding of the microstructure, interaction mechanism, and thermodynamic properties of AA-ILs. Herrera *et al.* have studied IL mixtures containing AA anions through MD simulations, analyzed HB, molecular arrangements, and solvation properties, and have revealed the structural characteristics of the mixtures.[65] This thesis mainly focus on systems of several different AAs as varying anions, while 1-ethyl-3-methylimidazolium ($[C_2C_1Im]$) was kept consistent as the cation, and analyzes the system from three aspects: polarizability, spectroscopy, and molecular structure.

1.2. Molecular dipole moments

The nonuniform distribution of positive and negative charges on each atom gives most molecules their characteristic dipole moment.[66] Dipole moments exist in common molecules such as water, and also in biological molecules such as proteins.[67,68] Some polar compounds such as hydrogen fluoride have unequal electron density between atoms. As a result, the molecule's dipole forms an electric dipole with an inherent electric field. The first scientist to extensively study molecular dipoles was the physical chemist Peter J. W. Debye,[69] and the unit of dipole moment was named Debye in his honor. The dipole moment can provide insight into the nature of chemical bonding (such as non-bonding electron pairs). In addition, finite differences of the dipole moment can be used to determine the magnitude of the polarizability.[70]
To obtain the dipole moment of a single molecule, maximally localized Wannier functions (MLWFs) is an effective method.[71–74] In 1937, Gregory Wannier introduced an alternative representation of localized orbitals, the "Wannier function (WF)".[71] Before this work, the electronic ground state of periodic systems was usually described by extended Bloch orbitals.[71,75] WF is different to Bloch functions, it is not eigenstates of the Hamiltonian, and need to make a trade-off between energy localization and spatial localization. After 1937, various methods have been developed that allow to iteratively transform extended Bloch orbitals from first-principles calculations into a unique set of maximally local WF, thereby constructing local molecular orbitals.[75] In the earlier chemistry literature, which the "local molecular orbitals (LMO)" have played an important role in the development computational chemistry.[76,77] However, due to the strong non-uniqueness of WF, the implementation of Wannier calculations in the Kohn-Sham framework of density DFT,[78] that is, first-principles electronic structure calculations, has been slow to develop. In 1997, a "maximum localization (ML)" criterion (similar to the method used for LMO construction in chemistry) was introduced to identify a unique set of WFs for a

given crystal by Marzari and Vanderbil.[79] Since then, the computational electronic structure community has begun to construct MLWFs and use it for different purposes, such as theoretical analysis of phonons, photonic crystals, cold-atom lattices and the local dielectric responses of insulators. The MLWFs center allows to assign each orbital to a molecule, which requires a lot of computational resources for positioning, which is more intensive than the calculation of electronic structure. According to the classical definition, the dipole moment can be calculated by summing the point charges at the nucleus and the center of the WF, then the electronic structure calculations are repeated with an external electric field in each time step and the polarizability is obtained by finite differences of the dipole moments.[70]

When convergence is slow, WF can easily take up a large portion of the total computation time for systems with hundreds of atoms, making simulations of infrared (IR) and Raman spectra very time-consuming. Although it is possible to assign WF to individual molecules based on their locality, it is not necessary to assign all orbitals to molecules, as the total electron density alone is sufficient to calculate the dipole moment. Therefore, any partitioning scheme that divides the electron density intrinsic to each time step into molecular contributions should be equally applicable to obtain molecular dipole moments and polarizabilities. Various approaches (such as the non empirical atoms-in-molecules (AIM) method[80] and Hirshfeld partitioning[81]) are primarily used to assign partial atomic charges in molecules. In addition, distinct boundaries between atoms can be obtained by topological analysis of the electron density, as in Bader's molecular atomic theory.[82] The Voronoi tessellation is purely geometric criteria, which can account for different atom sizes by shifting the boundary planes.[83] This is the method which has been used for the calculation of atomic partial charges.[84] The decisive parameters in the radical Voronoi tessellation are the radii assigned to the atoms.[83]

For theoretical studies in ILs, the electric dipole moment of ions are considered a physical indicator of its electronic structure since ILs have strong intermolecular interactions due to their ionicity.[53] In the study of Carlos *et al.*, with the analysis of ILs (dimethyl imidazolium chloride) using localized Wannier orbitals, the probability distributions of the ionic dipole moments for an isolated ion and for ions in solution compared.[85] Wendler *et al.* conducted Car-Parrinello simulations of three different imidazolium-based ILs and found that all systems have a broad distribution of ionic dipole moments and associated highly localized behavior. Except for the imidazolium-based system, even for the protic ILs monomethyl ammonium nitrate, the same characteristics are present.[86] In addition, the molecular electromagnetic moments resulting from the rational molecular separation in the bulk phase due to the van der Waals radius can be readily used to calculate the vibrational spectra of bulk systems from AIMD simulations, including IR,[87,88] Raman,[70] vibrational circular dichroism (VCD),[89] Raman optical activity (ROA),[90] and resonance Raman spectroscopy.[91]

Altering the dipole moment can influence the physical properties of ILs. For example, increasing the dipole moment in cations can lead to a reduction in the melting point.[92] Chapter 3 aims to provide a deeper understanding of the key molecular properties of unique ILs combinations. To achieve this, it is essential to first examine the liquid dynamics, including localities and fluctuations. In this study, we investigated these properties by conducting AIMD simulations of

AA-ILs.

1.3. Vibrational spectra

In the case of vibration spectra, the precise prediction of vibration spectra holds paramount importance in computational chemistry, particularly when employing theoretical methods to pre-screen experimental outcomes. Vibrational spectroscopy (like IR and Raman) has been recognized as a fundamental tool to characterize and understand the chemical state, structure and dynamics of molecules and their environment for a long time.[93] IR spectroscopy is one of the most important analytical techniques, since almost any sample can be studied in various states (liquids, solutions, pastes, powders, films, fibers, gases and surfaces).[94] It can be used for classification of various physical properties, determination of compound structures, and many other areas. This is a non-destructive analysis since the sample can usually be recovered for other uses and is suitable for trace samples (down to the sub-microgram range).[95] Extracting the information contained in IR spectra with the help of theoretical calculations and simulations can provide insights into the structure and dynamics of molecules of all sizes.
DFT is increasingly applied to studies of chemical and biological systems.[96–98] Nowadays, DFT can obtain a wide range of spectroscopic parameters, including quantities related to IR and optical spectra, X-ray absorption, Mössbauer, as well as all magnetic properties related to electron paramagnetic resonance spectroscopy except relaxation times.[99–102] In 1997, Silvestrelli *et al.* evaluated the IR spectrum of liquid water using Car-Parrinello MD to examine the effects of quantum corrections on IR absorption.[103] Compared to alternative approaches such as vibrational self-consistent fields (VSCF)[104,105] and perturbation corrections to the harmonic approximation,[106] AIMD simulation is characterized by its ability to sample conformations in phase space and to treat the electronic structure of molecular systems using the Born-Oppenheimer approximation.[107] In recent years, IR and Raman spectroscopy have provided crucial insights into the characterization of ILs.[108–111] A study by Wulf *et al.* combined theoretical DFT calculations and experimental methods to investigate the spectral properties of imidazolium-based ILs.[109] Furthermore, the review by Paschoal *et al.* showed the application of computationally calculated vibrational spectroscopy to study phase transitions in ILs.[108] Similarly, the power spectrum can be obtained through performing a Fourier transformation of the particle velocities autocorrelation.[112]
IR and Raman spectroscopy require the autocorrelation of the dipole moment and the molecular polarizability. In a previous study, the power spectra of several imidazolium-based ILs derived from AIMD simulations have been presented.[53] In chapter 4, we investigated both IR and Raman spectroscopy under AIMD simulations for several different AA with varying anions, while 1-ethyl-3-methylimidazolium ($[C_2C_1Im]$) was kept consistent as the cation. In this part, the consistency between the spectral experimental data and the theoretical data is also considered.

1.4. Structural analyses

For structural analyses, ILs are also excellent systems which can exhibit unique properties to standard solvents.[23] Among these are their properties to be involved in various attractive interactions, namely: van der Waals,[24] dispersion force[113] and solvophobic,[26] as well as specific and anisotropic forces, these being: HB,[27] halogen bond,[28] dipole–dipole[29] and magnetic dipole interactions. Both the structural considerations of the respective ions and the type, strength and number of interactions can effect the degree of anion–cation contact, which is the major factor determining the lattice energies, melting point, conductivity, viscosity and general behavior of ILs.[114–117]

Given the limitations of experiments, molecular simulations are well suited to explore the structure of ILs at the molecular level. The structure and dynamics of ILs were studied by MD simulations, revealing that there are long-range spatial correlations between ions and that the main contribution to the configurational energy comes from electrostatic interactions, which lead to charge ordering effects.[118] Radial pair distribution functions (RDFs) and combined distribution functions (CDFs) serve as essential tools for characterizing and comprehending the interactions within these intricate systems. The RDFs is highly dependent on the state of matter and can vary significantly between solids, gases and liquids.[119,120] In equations, RDFs are measured using g(r) and defines the probability of encountering a particle at a distance r from another observed particle. CDFs can offer a distinctive representation of the coordination geometry, serving as a fingerprint for characterization purposes.[121] In this case, Hardacre *et al.* made outstanding contributions to both computational and experimental aspects of ILs, such as the study of 1,3-dimethylimidazolium chloride by neutron diffraction, the structure of ILs, and the comparison of solute-solvent interactions and heat transfer.[122–124]

In the study of molecular interactions in ILs, π-interactions (such as anion/cation/lone pair electron-π and π-π interactions) play an important role in the structure.[125,126] When focusing on the AA-ILs, since the imidazole ring constitutes the basic unit of most ILs cations, both the stacking and T-shaped structures are important for understanding the properties of the system.[127] In addition, the physical properties are related to the structural formation of ILs. If it is assumed that HB strengthens the structure of ILs, it will lead to behavior similar to that of molecular liquids. It also can be seen from IL melting points, viscosities and vaporization enthalpies, HB has a significant effect on the structure and properties of ILs.[18] In chapter 5, we focus on investigating the bulk structure, aromatic-aromatic interactions and HB through AIMD simulations in different AA-ILs. The comprehensive analyses presented here provides valuable insight into the full spatial configuration of the systems under investigation, as well as the interactions that contribute to their structural stability.

2. Methodologies

2.1. The TRAVIS program package

Within molecular dynamics (MD) simulations, the most important output is the trajectory, which contains all atoms coordinates in every simulation step. In a system, if N particles are simulated, the trajectory can be viewed as a path through the 6N-dimensional phase space of the system, which is not directly accessible for interpretation and extraction of chemical characteristics.[128] Dimensionality reduction algorithms must be applied to transform the input data into a two-dimensional or three-dimensional dataset that can be more easily interpreted and visualized. At present, some methods like: radial pair distribution functions (RDFs), which provide insights into the system structure can be used in structural analyses easily.
One unified program package, TRAVIS (Trajectory Analyzer and Visualizer), contains all common analysis types that can be applied to a trajectory and will simplify rationalize and simplify the process of evaluating trajectories.[128] TRAVIS is not currently parallelized and runs on a single central processing unit (CPU) core. The latest version is currently available on the website http://www.travis-analyzer.de. The objective of TRAVIS is to combine a comprehensive array of analysis within a single program, creating a powerful tool and making it unnecessary to use multiple software applications in the evaluation of simulations.[128] TRAVIS can read many different input trajectory formats, such as: XYZ, PDB, mol2, DL_POLY,[129] LAMMPS, Amber,[130] Gaussian Cube and compressed BQB trajectories.[131] In the unit cell geometry, it can be read directly from the trajectory, then very large systems containing hundreds of thousands of atoms can be easily handled. When creating charts and visualizations, TRAVIS does not directly produce image files, instead, it generates input files for visualization programs (like: VMD,[132] xmgrace,[133] Gnuplot, Povray,[134] and Mathematica).
TRAVIS only reads information such as atom labels, positions and optional velocities from the input trajectory, and ignores any topological information: molecules, bonds, *et al.*. It takes a more sophisticated approach based on spatial domain decomposition. Domain decomposition and similar methods are commonly used in computational chemistry, but are rarely applied to trajectory post-processing.[135] In the case of structural analysis, regarding the particle density histograms, TRAVIS can give the corresponding number integral curve to easily determine the first solvation shell.[135] If two observables are correlated, a multidimensional histogram can be created. TRAVIS also can contain dynamical analysis, which are defined as analyses that are not invariant under re-shuffling of the trajectory frames.[135] For spectroscopic analysis, many functions for predicting vibrational spectra have been implemented in TRAVIS. In this thesis, all algorithms mentioned are implemented in TRAVIS. We studied known methods in the literature

and evaluated their general applicability.

2.2. Molecular dynamics simulation

The basic assumption of MD is that atoms can be treated as classical particles under the Born-Oppenheimer approximation. The system's Hamiltonian only depends on the positions and momenta of the atoms. Energy interactions between atoms are modeled using potential functions of varying complexity.[45] The dynamics of the quantum system is described by the time-dependent Schrödinger equation:

$$i\hbar\frac{\partial\Phi(r^{(n)},R^{(N)};t)}{\partial t}=\mathcal{H}\Phi(r^{(n)},R^{(N)};t). \tag{2.1}$$

Here, the Φ is total wave function of the nuclei and the electrons.[136] The notation $\mathrm{r}^{(n)}$ is used as the complete set of positions of all the n electrons and $\mathrm{R}^{(N)}$ is for the positions of the N nuclei which can avoid the confusion of the position r in space. In the system, the Hamiltonian is

$$\begin{aligned}\mathcal{H}&=-\sum_{I=1}^{N}\frac{\hbar^2}{2M_I}\nabla_I^2-\sum_{i=1}^{n}\frac{\hbar^2}{2m_e}\nabla_i^2+\mathcal{V}_{n-e}(r^{(n)},R^{(N)})\\&=-\sum_{I}\frac{\hbar^2}{2M_I}\nabla_i^2+\mathcal{H}_e(r^{(n)},R^{(N)}).\end{aligned} \tag{2.2}$$

In this equation, $\mathcal{V}_{n-e}$ is the sum of all the Coulombic interactions: nuclei-nuclei, electrons-electrons and nuclei-electrons. M_I and m_e is the mass of nucleus I and electron respectively. $\mathcal{H}_e$ is the electronic system Hamiltonian. When using the *ab initio* molecular dynamics (AIMD) method to consider the approximation of equation 2.1, complete wave function Φ is factored into two parts: one is Ψ which depending on the electronic degrees of freedom, while the other is $\mathcal{X}$ which corresponds to the nuclei. For the approximation of quantum dynamics, the quantum mechanical systems time evolution of nuclei and electrons need to be considered. Equation 3 is the time-independent electronic Schrödinger equation, which can present the eigenfunctions of the electrons at a particular time t:

$$\mathcal{H}_e(r^{(n)},R^{(N)})\Psi_k(r^{(n)},R^{(N)})=E_K(R^{(N)})\Psi_k(r^{(n)},R^{(N)}). \tag{2.3}$$

In this equation, the $\mathrm{R}^{(N)}$ is a fixed configuration of the nuclei, $\mathcal{H}_e$ is defined as in equation 2 : the Hamiltonian for the electronic sub-system and the eigenfunctions Ψ_k are orthonormal, and E_K is the energy of the electronic system in the fixed field of nuclei.
When using the Born-Huang,[137] the total wave function can be expanded:

$$\Phi(r^{(n)},R^{(N)};t)=\sum_{\iota=0}^{\infty}\Psi_\iota(r^{(n)},R^{(N)})\chi_\iota(R^{(N)};t), \tag{2.4}$$

where the functions χ_ι are time-dependent. Substituting the equation 4 into 1, the Born-Oppenheimer (BO) approximation can be obtained:

$$\left[-\sum_I \frac{\hbar}{2M_I}\nabla_I^2 + E_k(R^{(N)})\right]\chi_k(R^{(N)};t) = i\hbar\frac{\partial\chi_k(R^{(N)};t)}{\partial t}, \tag{2.5}$$

which is the quantum-mechanical equation of nuclei motion. Here the χ are identified as the set of nuclear wave functions for the selected electronic state k. The corresponding equation for the electronic degrees of freedom is

$$\mathcal{H}_e\Psi(r^{(n)},R^{(N)};t) = i\hbar\frac{\partial\Psi(r^{(n)},R^{(N)};t)}{\partial t}. \tag{2.6}$$

Besides, the electronic wave function can be presented in the basis of electronic states:

$$\Psi(r^{(n)},R^{(N)};t) = \sum_{\iota=0}^{\infty} c_\iota(t)\Psi_\iota(r^{(n)},R^{(N)};t), \tag{2.7}$$

where the coefficients $c_\iota(t)$ are the occupation numbers.
AIMD can show three different ways to simplify the modest-sized condensed phase problems that is not a pragmatic approach. The first of these is BO dynamics. Here the equations of motion are:

$$M_I\ddot{R}_I(t) = -\nabla_I \min_{\Psi_0}\left\{\langle\Psi_0|\mathcal{H}_e|\Psi_0\rangle\right\}, \tag{2.8}$$

and

$$E_0\Psi_0 = \mathcal{H}_e\Psi_0. \tag{2.9}$$

In equations 2.8 and 9, Ψ_0 is the ground-state adiabatic wave function at all times. For equation 9, E_0 is obtained from the solution of the equation 2.1 from the ground state that is established at every step in the dynamics by diagonalizing the Hamiltonian $\mathcal{H}_e$. In a molecular system comprising N electrons and M nuclei, the Hamiltonian $\mathcal{H}_e$ typically incorporates the kinetic energy of the electrons $\mathcal{T}_e$, the kinetic energy of the nuclei $\mathcal{T}_n$, the Coulomb repulsion between the electrons $\mathcal{V}_{ee}$, the Coulomb attraction between the nuclei and the electrons $\mathcal{V}_{ne}$, and the Coulomb repulsion between the nuclei $\mathcal{V}_{nn}$:

$$\begin{aligned}\mathcal{H}_e &= \mathcal{T}_e + \mathcal{T}_n + \mathcal{V}_{ee} + \mathcal{V}_{ne} + \mathcal{V}_{nn}\\ &= -\sum_{i=1}^{N}\frac{\hbar}{2m_e}\nabla_i^2 - \sum_{A=1}^{M}\frac{\hbar}{2m_A}\nabla_A^2 + \frac{e^2}{4\pi\varepsilon_0}\left(\sum_{i=1}^{N}\sum_{j=i+1}^{N}\frac{1}{r_{ij}} - \sum_{i=1}^{N}\sum_{A=1}^{N}\frac{Z_A}{r_{iA}} + \sum_{A=1}^{M}\sum_{B=A+1}^{M}\frac{Z_AZ_B}{r_{AB}}\right).\end{aligned} \tag{2.10}$$

Here, M_A and Z_A denote the mass and atomic number of nucleus A, respectively. The terms r_{ij}=|r_i-r_j|, r_{iA}=|r_i-R_A| and r_{AB}=|R_A-R_B| represent the respective distances between electrons and nuclei. The coordinates of electron i and nucleus A are given by r_i and R_A, respectively.
In the second approach, Ehrenfest dynamics[138] can solve the quantum mechanical motion of the

electrons at each step in equation 6 and use the wave function to calculate the force on each nucleus I:

$$M_I \ddot{R}_I = -\nabla_I \int dr^{(n)} \Psi^* \mathcal{H}_e \Psi = -\nabla_I \langle \mathcal{H}_e \rangle, \tag{2.11}$$

and Ehrenfest dynamics is a mean-field method.
In the third approach, it considered $\langle \Psi_0 | \mathcal{H}_e | \Psi_0 \rangle$ as a functional of the set of orbitals ψ_i, which developed by Car and Parrinello (CP).[139] If considering to construct a Lagrangian:

$$\mathcal{L} = \sum_I \frac{1}{2} M_I \dot{R}_I^2 + \sum_i \mu \left\langle \dot{\psi}_i | \dot{\psi}_i \right\rangle - \langle \Psi_0 | \mathcal{H}_e | \Psi_0 \rangle + \{constraints\} \tag{2.12}$$

where μ is a fictitious mass controlling the dynamics of the orbitals. When including a set of constraints in the Lagrangian to keep the underlying orbitals orthogonal:

$$M_I \ddot{R}_I(t) = -\nabla_I \langle \Psi_0 | \mathcal{H}_e | \Psi_0 \rangle + \nabla_I \{constraints\} \tag{2.13}$$

$$\mu \ddot{\psi}_i(t) = -\frac{\delta \langle \Psi_0 | \mathcal{H}_e | \Psi_0 \rangle}{\delta \psi_i^*} + \frac{\delta}{\delta \psi_i^*} \{constraints\} \tag{2.14}$$

In these equations, $\delta / \delta \psi_i^*$ indicates a functional derivative. In the cases of both BO and CP dynamics, the force on the nuclei can be evaluated using the Hellmann-Feynman theorem:

$$-\nabla_I \langle \Psi_0 | \mathcal{H}_e | \Psi_0 \rangle \approx - \langle \Psi_0 | \nabla_I \mathcal{H}_e | \Psi_0 \rangle . \tag{2.15}$$

2.3. Density functional theory and the Kohn-Sham method

The approach of BO need a knowledge of the electronic wave function for the system ground state. The symmetry (to the exchange of two electrons) Ψ_0 can be included through the full wave function of the individual wave functions of every electrons n:

$$\Psi_0(\mathbf{r}^{(n)}) = \frac{1}{\sqrt{n!}} \begin{vmatrix} \psi_1(\mathbf{r}_1) & \psi_2(\mathbf{r}_1) & \cdots & \psi_n(\mathbf{r}_1) \\ \psi_1(\mathbf{r}_2) & \psi_2(\mathbf{r}_2) & \cdots & \psi_n(\mathbf{r}_2) \\ \vdots & \vdots & \ddots & \vdots \\ \psi_1(\mathbf{r}_n) & \psi_2(\mathbf{r}_n) & \cdots & \psi_n(\mathbf{r}_n) \end{vmatrix} \tag{2.16}$$

The electronic structure calculations for condensed phase systems can be determined by density functional theory (DFT). DFT is a widely used method for solving the electronic Schrödinger equation. In this context, the expectation value defines a functional, denoted as F_{HK}, of the ground-state electron density, ρ_0(r) which only depends on the spatial coordinate, r:

$$F_{HK}[\rho_0] = \left\langle \Psi_0[\rho_0] | \mathcal{H}_e^{'} | \Psi_0[\rho_0] \right\rangle . \tag{2.17}$$

For the $\mathcal{H}_e^{'}$ in equation 17:

$$\mathcal{H}_e^{'} = \mathcal{K}[\rho] + \mathcal{V}_{ee}[\rho], \tag{2.18}$$

here $\mathcal{K}$ is the quantum mechanical kinetic energy and $\mathcal{V}_{ee}$ is the potential energy between the electrons, respectively. The corresponding energy functional E[ρ] depends on the external field generated by the positively charged nuclei acting on the electrons:

$$E[\rho] = F_{HK}[\rho] + \int dr \mathcal{V}_{ext}(r)\rho(r, R^{(N)}). \tag{2.19}$$

The next is to calculate the universal functional F_{HK}. The Kohn-Sham method can replace the system of n interacting electrons by the auxiliary system of n independent electrons. When donating the non-interacting system by subscript s:

$$E_s = \mathcal{K}_s + \int dr \mathcal{V}_s \rho_s. \tag{2.20}$$

where the $\mathcal{V}_s(r)$ will be a particular local potential, and the ground state density ρ_0 is equal to ρ_s. When the equation is in the case of the degeneration of the ground state of the non-interacting systems, the sum is over the occupied orbitals:

$$\rho_0(r) = \sum_{i=1}^{occ} f_i |\psi_i(r)|^2, \tag{2.21}$$

and f_i is the occupancy number of the orbital. In addition, the single-particle orbitals can be obtained from the Schrödinger equation:

$$\mathcal{H}_{KS}\psi_i = \left[-\frac{\hbar^2}{2m_e}\nabla^2 + \mathcal{V}_s \right] \psi_i = \epsilon_i \psi_i, \tag{2.22}$$

and the total energy of the interacting system is:

$$E_{KS}[\rho_0] = \mathcal{K}_s[\rho_0] + \int dr \mathcal{V}_{ext}(r)\rho_0(r) + \frac{1}{2}\int\int dr dr' \frac{\rho_0(r)\rho_0(r')}{|r - r'|} + E_{XC}[\rho_0]. \tag{2.23}$$

This energy includes four terms: the first one is the non-interacting system kinetic energy:

$$\mathcal{K}_s[\rho_0] = -\frac{\hbar^2}{2m_e}\sum_{i=1}^{occ} f_i \left\langle \psi_i | \nabla^2 | \psi_i \right\rangle; \tag{2.24}$$

the second one is the energy of the electrons in the nuclei static field; the third is the classical Coulomb energy between the electrons and the fourth is the exchange-correlation energy. As a result, the classical Coulomb repulsion can be presented as:

$$J[\rho(r)] = \frac{1}{4\pi\varepsilon_0}\frac{1}{2}\int\int \frac{\rho(r_1)\rho(r_2)}{|r_1 - r_2|} dr_1 dr_2. \tag{2.25}$$

With equation 23, the single-particle potential can be given by:

$$\mathcal{V}_s(r) = \mathcal{V}_{ext}(r) + \int dr' \frac{\rho_0(r')}{|r - r'|} + \frac{\delta E_{xc}}{\delta \rho(r)}. \tag{2.26}$$

In this approach, E_{xc} needs to be known and is always represented with the local density approximation:

$$E_{xc}[\rho_0(r)] \approx \int dr \rho_0(r) \varepsilon_{xc}[\rho_0(r)]. \tag{2.27}$$

Here the ε_{xc} is the

$$E_{xc}^{GGA}[\rho_0(r)] \approx \int dr f_{xc}[\rho_0(r), \nabla\rho_0(r)] \tag{2.28}$$

According to the second Hohenberg–Kohn theorem, the Kohn–Sham orbitals are determined by minimizing the electronic energy with respect to the orbitals. This minimization is subject to the constraint that the orbitals must be orthonormal. By applying the method of Lagrange multipliers, this leads to the Kohn–Sham equations:

$$\left(-\frac{\hbar^2}{2m_e}\nabla^2 + \upsilon_{ext}(r) + \frac{1}{4\pi\varepsilon_0}\int \frac{\rho(r_1)}{|r-r_1|}dr_1 + \frac{\delta E_{XC}[\rho(r)]}{\delta\rho(r)}\right)\theta_i(r) = \epsilon\theta_i(r) \tag{2.29}$$

with the orbital energies ϵ_i.

2.4. Basis set expansion

The Kohn–Sham equation is typically solved by expressing the Kohn–Sham orbitals, θ_i(r), as linear combinations of a finite set of n known basis functions, ψ_j(r).

$$\theta_i(r) = \sum_{j=1}^{n} C_{ij}\psi_j(r). \tag{2.30}$$

This transformation allows the Kohn–Sham equations to be converted from their integro-differential form into a matrix representation:

$$\mathrm{KC} = \mathrm{SC}\epsilon, \tag{2.31}$$

here, K is defined as the Kohn–Sham matrix with the elements:

$$K_{ij} = \left\langle \psi_i(r)| -\frac{\hbar^2}{2m_e}\nabla^2 + \upsilon_{ext}(r) + \frac{1}{4\pi\varepsilon_0}\int \frac{\rho(r_1)}{|r-r_1|}dr_1 + \frac{\delta E_{XC}[\rho(r)]}{\delta\rho(r)}|\psi_j(r)\right\rangle, \tag{2.32}$$

and the S is defined as

$$S_{ij} = \langle\psi_i(r)|\psi_j(r)\rangle \tag{2.33}$$

which is the overlap matrix with the elements. Finally, C is the matrix of the coefficients C_{ij} in equation 30, and ϵ is the diagonal matrix with the orbital energies ϵ_i.
In quantum chemistry, the basic functions $\psi_i(r)$ can be proposed in a common method which are contracted Gaussian type orbitals (GTOs) of the general form:

$$\psi(r) = N\xi(r-r_0)\sum_{k=1}^{m} d_k exp(-\xi_k|r-r_0|^2). \tag{2.34}$$

It tries to mimic the atomic orbitals of the individual atoms. In this equation N is a normalization constant, $\xi(r-r_0)$ is the angular momentum dependence, and r_0 is the center of the basic function. The GTOs can show good results with small set sizes and the straight description of all electrons in the systems. In solid state physics, it is very common to use the plane wave basic sets since the periodicity of the crystal imposes the same periodicity on the electron density:

$$\psi(r) = \frac{1}{\sqrt{\Omega}} exp(iG \cdot r). \tag{2.35}$$

Here, Ω is the volume of the periodic cell and G is the wave vector which satisfies the periodic boundary conditions.

2.5. Dipole moments and polarizabilities

2.5.1. Maximally localized wannier functions

MLWFs have become an established tool for post-processing of electronic structure calculations. With periodic boundary conditions, the electronic-structure can be calculated. The one-particle effective Hamiltonian H commutes with T_R, the lattice-translation operator to make the Bloch orbitals $|\psi_n K\rangle$ as common eigenstates:

$$[H, T_R] = 0 \Rightarrow \psi_{nK}(r) = \mu_{nK}(r) e^{iK \cdot r}, \tag{2.36}$$

where $\mu_n K(r)$ is with the periodicity of the Hamiltonian. If choosing equal amplitudes across the Brillouin zone, we can obtain:

$$w_0 = \frac{V}{(2\pi)^3} \int_{BZ} dK \psi_{nK}(r), \tag{2.37}$$

where V is the real-space primitive cell volume. When inserting a phase factor $e^{-k \cdot R}$ into the integrand of this equation, here R is a real-space lattice vector which has the effect of translating the real-space WF by R. According to Dirac bra-ket notation that R_n refers to the WF w_{nR} in cell R associated with band n, WFs can be constructed through [71]

$$|Rn\rangle = \frac{V}{(2\pi)^3} \int_{BZ} dK e^{-iK \cdot R} |\psi_{nK}\rangle. \tag{2.38}$$

The inverse transform of this equation is:

$$|\psi_{nK}\rangle = \sum_R e^{iK \cdot R} |Rn\rangle. \tag{2.39}$$

In addition, the equivalence between the Bloch and Wannier representations can also be shown by expressing the projection operator P in both representations:

$$p = \frac{V}{(2\pi)^3} \int_{BZ} dK |\psi_{nK}\rangle\langle\psi_{nK}| = \sum_R |R_n\rangle\langle R_n|. \tag{2.40}$$

As we mentioned in the introduction, by employing the transformation of the Kohn-Sham orbitals, MLWFs can be calculated. For this method, the localization functional is defined as

$$\Omega = \sum_n [\langle 0n|r^2|0n\rangle - \langle 0n|r|0n\rangle^2] = \sum_n [\langle r^2\rangle_n - \bar{r}_n^2] \tag{2.41}$$

where the Ω is expressed in terms of the Bloch functions, with the sum of the quadratic spreads of the WFs in the home unit cell around their centers.[75] Currently, the challenge associated with poorly defined standard dipole operators in the context of applying periodic boundary conditions in AIMD simulations of liquids has been addressed. The Berry phase approach to polarization can offer the dipole moment of the whole simulation cell under periodic boundary conditions.[140] The calculation of the local Wannier function is achieved by utilizing AIMD simulations combined with the application of the block Jacobi method.[72] In Equation 42, the dipole moment for each molecule i is composed of two components: the sum of all Wannier function centers assigned to the molecule and the sum of nuclei with charges Z_A at the positions R_A:

$$\mu = -2e\sum_{i=1}^{N} r_i + e\sum_{A=1}^{M} Z_A R_A, \tag{2.42}$$

where e is the elementary charge. This summation method can approximate the total dipole moment of the cell. TRAVIS is able to take the resulting Wannier function centers as input to assign molecules and calculate dipole moments.
When recalling the dipole moment induced by an electric field E, the polarizabilities can be calculated by:

$$\mu_{ind} = \alpha E, \tag{2.43}$$

where α is the second-order polarizability tensor. Using the WF center for the dipole moment can provide an individual polarizability for each molecule.
When considering charge schemes such as Blöchl, Löwdin and Mulliken methods, the molecular dipole moment μ can be obtained through the classical definition:

$$\mu = \sum_{i=1}^{N} q_i \cdot \vec{r}_i \tag{2.44}$$

where the N shows the number of nuclei. The q_i and $\vec{r}_i$ are charge and position, respectively.

2.5.2. Voronoi tessellation of the electron density

For the method of MLWFs, especially in systems with several hundred atoms, it always takes much longer than the actual electronic structure calculation since the Wannier function centers assign each orbital to a molecule. A simple method to generally partition the space of a simulation cell is Voronoi tesselation. The Voronoi diagram[84] is a method of interpolating spatial data into a polygon around each point, where every location in the area around that point is closer to

that point than any other point. This method was invented by a professor at the University of Warsaw over 100 years ago and has been used in many scientific disciplines around the world. Voronoi tessellation[70] can divide the space of analog cells, it defines n Voronoi cells C_i as:

$$\mathrm{C_i} = \{\mathrm{x} \in \mathbb{R}^3 | \mathrm{r_i^2} \leq (\mathrm{x} - \mathrm{s_j})^2 - \mathrm{r_j^2} \forall \mathrm{j} \neq \mathrm{i}\}, \mathrm{i}, \mathrm{j} = 1, ..., \mathrm{n}. \tag{2.45}$$

This equation takes a set of n sites s_i as input, meaning that cell C_i contains all points that are closer to site s_i than any other site. The Voronoi tessellation assigns each point in space to precisely one cell. The cell faces are always positioned midway between two atoms. In the radical Voronoi tessellation method, which extends the partitioning scheme and makes it possible to keep the Voronoi sites at the atom positions, when radius r_i is assigned to each site, the cells C_i^r is determined according to:

$$C_i^r = \{x \in \mathbb{R}^3 | (x - s_i)^2 - r_i^2 \leq (x - s_j)^2 - r_j^2, \ \forall j \neq i\}, i, j = 1, \ldots, n. \tag{2.46}$$

Here, the distance to the sites themselves from the original Voronoi tessellation is changed to the power distance to spheres around the sites. The electron density $\rho(r)$ which as a function of spatial coordinates r over molecular cells in space can be used to obtain the dipole moment distribution:

$$\mu_k = \int_{M_K} r\rho(r)dr, k = 1, \ldots, N. \tag{2.47}$$

For each cell, the charge calculation is :

$$q_i = \int_{C_i^r} \rho(r)dr, \tag{2.48}$$

and the dipole moment:

$$\mu = \int_{C_i^r} r\rho(r)dr. \tag{2.49}$$

For these equations, the integration must be performed over the unit cell volume. In addition, unit cells belonging to the same molecule's atoms can be connected to obtain a molecular unit cell, and the charge and dipole moment of the atomic unit cells can be added to obtain the molecular charge and molecular dipole moment.

2.6. Angular probability distribution

Generally, to further strengthen the argument that the electric dipole moments of anions and cations and their corresponding fluctuations are essentially determined by local properties, the dipole–dipole angular correlations as a function of the shell around each molecule should be studied.[141] The angular distribution is calculated using:

$$\cos\Phi(charge - dipole) = (\mu_{cat}^{ref} \cdot r_{cat}^{shell_i})/(|\mu_{cat}^{ref}| \cdot |r_{cat}^{shell_i}|) \tag{2.50}$$

and

$$\cos\phi(dipole-dipole) = (\mu_{cat}^{ref} \cdot \mu_{cat}^{shell_i})/(|\mu_{cat}^{ref}| \cdot |\mu_{cat}^{shell_i}|) \tag{2.51}$$

Here, μ_{cat}^{ref} is defined as the dipole moment and r_{cat}^{shell} is defined as the vector of the center of ring to the center of charge (COC) of the reference cation. In these analyses, COC is defined as the center of the ion for analyzing the angular distribution. This means that the center of the molecular geometry is weighted by the charges on the atoms.[38] Thereby, the electric dipole moments of the cation and anion of the reference molecule are associated with the electric dipole moments of the cation and anion of the molecule within the first solvation shell (the first minimum of the radial distribution function).[141] Then the same procedure is applied to relate the electric dipole moments of the cation and anion of the reference molecule to the electric dipole moments of the molecules in a second solvation shell, and the size contains approximately the same number of molecules of the first solvation shell. Finally, the electric dipole moments of the anions and cations of the reference molecule are related to the electric dipole moments of the molecule beyond the second solvation shell.[141]

2.7. Vibrational spectroscopy

2.7.1. Infrared absorption and intensities

Molecules absorb frequencies that are characteristic of their molecular structure. These absorptions occur at resonant frequencies, where the frequency of the absorbed radiation matches the frequency of the vibration. By absorbing or emitting electromagnetic radiation, molecules can change from one eigenstate to another with an energy equal to the energy difference between the two states. For nuclear vibrations in molecules, these energy differences are typically in the range of 10^{-21} J to 10^{-19} J, which correspond to the IR region of the electromagnetic spectrum. For the experimental technique of IR, the results can be obtained from illuminating a chemical with infrared (IR) radiation and measuring its absorption rate based on its energy. In the Born-Oppenheimer and harmonic wave approximations, the resonant frequencies are associated with normal vibrational modes which corresponding to the ground state potential energy surface of the molecule's electrons. In static quantum chemistry, the theoretical values of IR spectra intensities can be derived from Fermi's golden rule[142] and calculated through the following expression:

$$W_{i\to f} = \frac{1}{\hbar^2}|\left\langle \nu_f|\mathcal{H}^{'}|\nu_i\right\rangle|^2 \rho N(\nu_{fi}). \tag{2.52}$$

Here, the transition rate $W_{i\to f}$ is for the transition from the initial state $|\nu_i>$ to the final state $|\nu_f>$, the perturbation $\mathcal{H}$ is by the electromagnetic radiation and the $\rho_N(\nu)$ is a density of photon states per frequency range. The perturbation expression is

$$\left\langle \nu_f|\mathcal{H}^{'}|\nu_i\right\rangle = -\left\langle \nu_f|\bar{\mu}(\mathbf{Q})\cdot E|\nu_i\right\rangle = -\left\langle \nu_f|\bar{\mu}(\mathbf{Q})|\nu_i\right\rangle \cdot E_O, \tag{2.53}$$

where the $\bar{\mu}(\mathbf{Q})$ is the molecular dipole moment dependant on the mass-weighted normal coordinates $\mathbf{Q}$, E is the electric field vector of the radiation and E_0 is the average amplitude. The

molecular dipole moment is derived from the Taylor series around the minimum of the potential energy surface up to first order:

$$\bar{\mu}(\mathbf{Q}) = \bar{\mu}_0 + \sum_{k=1}^{g} \left(\frac{\partial \bar{\mu}(\mathbf{Q})}{\partial \mathbf{Q}_k} \right)_0 \mathbf{Q}_k. \tag{2.54}$$

In this equation, g is as g = 3M - 6 (g = 3M - 5 in a linear molecule) within the harmonic approximation. Based on the above assumptions, the analytical expression of the transition dipole matrix element can be obtained, and the integrated absorption coefficient corresponding to the transition of the resonator from the ground state to the first excited state of mode k can be given by[143]

$$A_k = \frac{1}{4\pi\varepsilon_0} \frac{N_A \pi}{3c^2} \left(\frac{\partial \bar{\mu}(\mathbf{Q})}{\partial \mathbf{Q}_k} \right)_0^2. \tag{2.55}$$

As described above, once the normal mode of the molecule is known, the IR intensity can be calculated by taking the derivative of the dipole moment along the normal coordinate. However, it is impossible to obtain these derivatives directly from the MD simulation. One of the alternative approaches is to conduct the MD simulation in equilibrium in which all modes are excited at once, so the oscillation of the dipole moment contains contributions from all modes at the same time. When using the mass-weighted coordinate q = $\sqrt{m}$x, the trajectory can be obtained through:

$$q(t) = \sqrt{m} x_0 cos(\omega_0 + \varphi), \tag{2.56}$$

where the x_0 is the amplitude, ω_0 is the eigenfrequency, and φ is the phase. The dipole moment μ is

$$\mu(q) = \mu_0 + \left(\frac{\partial \mu}{\partial q} \right)_0 q, \tag{2.57}$$

and μ_0 is the dipole moment at the equilibrium position. When inserting the trajectory yields for the time-dependent dipole moment:

$$\mu(t) = \mu_0 + \left(\frac{\partial \mu}{\partial q} \right)_0 \sqrt{m} x_0 cos(\omega_0 + \varphi). \tag{2.58}$$

If using the time derivative of the coordinate instead of the coordinate itself, the equilibrium dipole moment which does not carry information relevant will be removed:

$$\dot{\mu}(t) = -\left(\frac{\partial \mu}{\partial q} \right)_0 \sqrt{m} x_0 \omega_0 sin(\omega_0 + \varphi). \tag{2.59}$$

The autocorrelation function is calculated:

$$R_{\dot{\mu}}(t) = \frac{1}{2} \left(\frac{\partial \mu}{\partial q} \right)_0^2 m x_0^2 \omega_0^2 cos(\omega_0 t), \tag{2.60}$$

which removes the dependence on the initial conditions of the MD simulation in terms of the phase φ. The Fourier transform of this expression can be given as:

$$\mathcal{F}(R_{\dot{\mu}})(\omega) = \int_{-\infty}^{\infty} R_{\dot{\mu}}(t) exp(-i\omega t) dt = \frac{1}{2}\left(\frac{\partial \mu}{\partial q}\right)_0^2 m x_0^2 \omega_0^2 \pi(\delta(\omega-\omega_0)+\delta(\omega+\omega_0)), \tag{2.61}$$

and the total integral of the spectrum is:

$$\int_{-\infty}^{\infty} \mathcal{F}(R_{\dot{\mu}})(\omega) d\omega = \left(\frac{\partial \mu}{\partial q}\right)_0^2 m x_0^2 \omega_0^2 \pi. \tag{2.62}$$

At the maximum elongation x = x_0, there is only potential energy $kx^2{}_0/2$, while the kinetic energy is zero. At the equilibrium position x = 0, the potential energy is zero and the kinetic energy is $kx^2{}_0/2$. On average, the kinetic energy is half of the maximum value, that is, $<E_{kin}> = kx^2{}_0/4$. Therefore, according to the definition of the characteristic frequency ω_0, the relationship between the oscillator amplitude and the average kinetic energy is $x_0 = \sqrt{4 < E_{int} > /m}/\omega_0$, therefore this is equal to:

$$\int_{-\infty}^{\infty} \mathcal{F}(R_{\dot{\mu}})(\omega) d\omega = \left(\frac{\partial \mu}{\partial q}\right)_0^2 \cdot 4\pi \langle E_{kin} \rangle = \left(\frac{\partial \mu}{\partial q}\right)_0^2 \cdot 2\pi k_B T. \tag{2.63}$$

Comparing these two equations (49 and 56), the IR spectrum in MD simulations can be given by:

$$A(\omega) = \frac{N_A}{24\pi\varepsilon_0 c^2 k_B T} \int_{-\infty}^{\infty} \langle \dot{\mu}(\tau) \cdot \dot{\mu}(\tau + t) \rangle_\tau exp(-i\omega t) dt, \tag{2.64}$$

where the vector autocorrelation dipole moment is switched to the general three-dimensional case. The wavenumber-dependent representation

$$A(\tilde{v}) = \frac{N_A}{12\varepsilon_0 c k_B T} \int_{-\infty}^{\infty} \langle \dot{\mu}(\tau) \cdot \dot{\mu}(\tau + t) \rangle_\tau exp(-2\pi i c\tilde{v} t) dt \tag{2.65}$$

can be calculated.

2.7.2. Raman scattering and intensities

Raman scattering or Raman effect is the inelastic scattering of photons by matter. This physical process can change the quantum state of a molecule, and there are both an exchange of energy and a change in the direction of light. When the photons are scattering, most are scattered elastically (Rayleigh scattering), with the scattered photon having the same energy (frequency, wavelength and color) as the incident photon, but in a different direction. A small fraction (about one part per million) of the scattered photons are inelastically scattered and have a different (usually lower) energy than the incident photon, which means that the molecule switches to another quantum state. These are Raman scattered photons.[144] Due to the conservation of energy, the photon energy changes according to the energy difference between the two molecular states. As early as 1923, Adolf Smekal predicted this effect through theoretical research.[145] After five years, Indian scientist C. V. Raman discovered this effect with the assistance of his student

K. S. Krishnan.[146] Then this effect was named Raman.
Raman spectroscopy identifies the structure of the molecule by determining the vibrational mode of the molecule, as well as observing the rotational and low-frequency modes of the system.[144] The lasers from visible, near-IR, near-ultraviolet range, or X-rays can be used in Raman spectra. In this process, the laser light interacts with the molecules in the system, leading to the energy change of the photon, thus providing information on the vibrational modes in the system. Usually, the IR spectra produce similar and complementary information, so the Raman spectra can be directly compared to the IR spectra.
The Placzek's classical theory of polarizability defines the Raman intensities theoretical values.[147] The dipole moment in the molecule is caused from the electric field of the incident radiation. The induced dipole moment value μ_{fi}^{ind} is defined quantum mechanically by evaluation of the corresponding polarizability matrix elements:

$$\left\langle \mu_{\mathrm{fi}}^{\mathrm{ind}} \right\rangle = \langle \nu_f | \bar{\alpha}(\mathbf{Q}) | \nu_i \rangle \, \mathrm{E}_0 \tag{2.66}$$

which assumes that the electric field is constant within the molecule, with an average magnitude of E_0. The polarizability tensor $\bar{\alpha}(\mathbf{Q})$ is expanded in a Taylor series:

$$\bar{\alpha}(\mathbf{Q}) = \bar{\alpha}_0 + \sum_{k=1}^{g} \left(\frac{\partial \bar{\alpha}(\mathbf{Q})}{\partial \mathbf{Q}_k} \right)_0 \mathbf{Q}_k. \tag{2.67}$$

The $\bar{\alpha}(\mathbf{Q})$ is the polarizability depending on the mass-weighted normal coordinates $\mathbf{Q}$.
In Raman spectroscopy, an important parameter is the scattering geometry employed in the measurement setup. The incident light beam propagates along the y axis and is polarized along the x axis, and the scattered light detector is located on the z axis and is equipped with a polarization filter to measure the x polarization intensity $\mathrm{I}^{\parallel}$ and the y polarization intensity $\mathrm{I}^{\perp}$. If the molecule is fixed relative to the laboratory coordinate system, here the results of differential Raman scattering of vibrational mode k are given by:

$$I_k^{\parallel} = \frac{\pi}{\varepsilon_0^2} (\widetilde{\nu}_{in} - \widetilde{\nu}_k)^4 \frac{h}{8\pi^2 c \widetilde{\nu}_k} \left(\frac{\partial \bar{\alpha}_{xx}(\mathbf{Q})}{\partial \mathbf{Q}_k} \right)_0^2 \frac{1}{1 - exp\left(-\frac{hc\widetilde{\nu}_k}{k_B T} \right)} \tag{2.68}$$

and

$$I_k^{\perp} = \frac{\pi}{\varepsilon_0^2} (\widetilde{\nu}_{in} - \widetilde{\nu}_k)^4 \frac{h}{8\pi^2 c \widetilde{\nu}_k} \left(\frac{\partial \bar{\alpha}_{xy}(\mathbf{Q})}{\partial \mathbf{Q}_k} \right)_0^2 \frac{1}{1 - \exp\left(-\frac{hc\widetilde{\nu}_k}{k_B T} \right)}. \tag{2.69}$$

In these equations, $\widetilde{\nu}_{in}$ is the wavenumber of the incident radiation, $\widetilde{\nu}_k$ is the wavenumber corresponding to k and T is the temperature. If the molecules are randomly oriented relative to the laboratory frame, the results which takes the classical averages of the polarizability tensor components are given by:

$$I_k^{\parallel} = \frac{\pi}{\varepsilon_0^2} (\widetilde{\nu}_{in} - \widetilde{\nu}_k)^4 \frac{h}{8\pi^2 c \widetilde{\nu}_k} \frac{45a_k^2 + 4\gamma_k^2}{45} \frac{1}{1 - \exp\left(-\frac{hc\widetilde{\nu}_k}{k_B T} \right)} \tag{2.70}$$

and

$$I_k^{\perp} = \frac{\pi}{\varepsilon_0^2}(\widetilde{\nu}_{in} - \widetilde{\nu}_k)^4 \frac{h}{8\pi^2 c\widetilde{\nu}_k} \frac{3\gamma_k^2}{45} \frac{1}{1 - exp\left(-\frac{hc\widetilde{\nu}_k}{k_B T}\right)} \tag{2.71}$$

with the isotropic polarizability derivative

$$a_k = \frac{1}{3}\left(\left(\frac{\partial \bar{\alpha}_{xx}(\mathbf{Q})}{\partial \mathbf{Q}_k}\right)_0 + \left(\frac{\partial \bar{\alpha}_{yy}(\mathbf{Q})}{\partial \mathbf{Q}_k}\right) + \left(\frac{\partial \bar{\alpha}_{zz}(\mathbf{Q})}{\partial \mathbf{Q}_k}\right)\right) \tag{2.72}$$

and the anisotropy

$$\gamma_k^2 = \frac{1}{2}\left(\left(\frac{\partial \bar{\alpha}_{xx}(\mathbf{Q})}{\partial \mathbf{Q}_k}\right)_0 - \left(\frac{\partial \bar{\alpha}_{yy}(\mathbf{Q})}{\partial \mathbf{Q}_k}\right)_0\right)^2 + \frac{1}{2}\left(\left(\frac{\partial \bar{\alpha}_{yy}(\mathbf{Q})}{\partial \mathbf{Q}_k}\right)_0 - \left(\frac{\partial \bar{\alpha}_{zz}(\mathbf{Q})}{\partial \mathbf{Q}_k}\right)_0\right)^2 + \frac{1}{2}\left(\left(\frac{\partial \bar{\alpha}_{zz}(\mathbf{Q})}{\partial \mathbf{Q}_k}\right)_0 - \left(\frac{\partial \bar{\alpha}_{xx}(\mathbf{Q})}{\partial \mathbf{Q}_k}\right)_0\right)^2 + 3\left(\frac{\partial \bar{\alpha}_{xy}(\mathbf{Q})}{\partial \mathbf{Q}_k}\right)_0^2 + 3\left(\frac{\partial \bar{\alpha}_{yz}(\mathbf{Q})}{\partial \mathbf{Q}_k}\right)_0^2 + 3\left(\frac{\partial \bar{\alpha}_{zx}(\mathbf{Q})}{\partial \mathbf{Q}_k}\right)_0^2. \tag{2.73}$$

If the polarizability replaces the dipole moment, the Raman spectrum can be derived in the same way as IR. The polarization frequency-dependent differential Raman scattering cross section for a fixed molecular orientation relative to the laboratory coordinate system can be given by:

$$I^{\parallel}(\omega) = \frac{\hbar}{64\pi^3 \varepsilon_0^2 c^4 k_B T} \frac{(\omega_{in} - \omega)^4}{(1 - \exp(-\frac{\hbar\omega}{k_B T}))} \int_{-\infty}^{\infty} \langle \dot{\alpha}_{xx}(\tau)\dot{\alpha}_{xx}(\tau + t)\rangle_{\tau} \exp(-i\omega t)dt \tag{2.74}$$

and

$$I^{\perp}(\omega) = \frac{\hbar}{64\pi^3 \varepsilon_0^2 c^4 k_B T} \frac{(\omega_{in} - \omega)^4}{(1 - \exp(-\frac{\hbar\omega}{k_B T}))} \int_{-\infty}^{\infty} \langle \dot{\alpha}_{xy}(\tau)\dot{\alpha}_{xy}(\tau + t)\rangle_{\tau} exp(-i\omega t)dt. \tag{2.75}$$

In the case of random molecular orientations relative to the laboratory coordinate system:

$$I^{\parallel}(\omega) = \frac{\hbar}{64\pi^3 \varepsilon_0^2 c^4 k_B T} \frac{(\omega_{in} - \omega)^4}{(1 - \exp(-\frac{\hbar\omega}{k_B T}))} \frac{45a(\omega) + 4\gamma(\omega)}{45} \tag{2.76}$$

and

$$I^{\perp}(\omega) = \frac{\hbar}{64\pi^3 \varepsilon_0^2 c^4 k_B T} \frac{(\omega_{in} - \omega)^4}{(1 - \exp(-\frac{\hbar\omega}{k_B T}))} \frac{3\gamma(\omega)}{45} \tag{2.77}$$

with the isotropic contribution

$$a(\omega) = \int_{-\infty}^{\infty} \left\langle \frac{\dot{\alpha}_{xx}(\tau) + \dot{\alpha}_{yy}(\tau) + \dot{\alpha}_{zz}(\tau)}{3} \frac{\dot{\alpha}_{xx}(\tau + t) + \dot{\alpha}_{yy}(\tau + t) + \dot{\alpha}_{zz}(\tau + t)}{3} \right\rangle_{\tau} \exp(-i\omega t)dt \tag{2.78}$$

and the anisotropic contribution:

$$\begin{aligned}\gamma(\omega) = \int_{-\infty}^{+\infty} \Big[& \frac{1}{2} \left\langle (\dot{\alpha}_{xx}(\tau) - \dot{\alpha}_{yy}(\tau))(\dot{\alpha}_{xx}(\tau+t) - \dot{\alpha}_{yy}(\tau+t)) \right\rangle_\tau \\ & + \frac{1}{2} \left\langle (\dot{\alpha}_{yy}(\tau) - \dot{\alpha}_{zz}(\tau))(\dot{\alpha}_{yy}(\tau+t) - \dot{\alpha}_{zz}(\tau+t)) \right\rangle_\tau \\ & + \frac{1}{2} \left\langle (\dot{\alpha}_{zz}(\tau) - \dot{\alpha}_{xx}(\tau))(\dot{\alpha}_{zz}(\tau+t) - \dot{\alpha}_{xx}(\tau+t)) \right\rangle_\tau \\ & + 3 \left\langle \dot{\alpha}_{xy}(\tau)\dot{\alpha}_{xy}(\tau+t) \right\rangle_\tau + 3 \left\langle \dot{\alpha}_{yz}(\tau)\dot{\alpha}_{yz}(\tau+t) \right\rangle_\tau \\ & + 3 \left\langle \dot{\alpha}_{zx}(\tau)\dot{\alpha}_{zx}(\tau+t) \right\rangle_\tau \Big] \exp(-i\omega t) \mathrm{d}t \end{aligned} \tag{2.79}$$

Like IR spectrum, these formulas can be transferred to a wavenumber-dependent representation, which is the representation actually calculated in TRAVIS. In the case of fixed molecular orientation with respect to the laboratory coordinate system, the wavenumber in Raman is given as:

$$I^{\parallel}(\widetilde{\nu}) = \frac{h}{8\varepsilon_0^2 k_B T} \frac{(\widetilde{\nu}_{in} - \widetilde{\nu})^4}{\widetilde{\nu}(1 - \exp(-\frac{hc\widetilde{\nu}}{k_B T}))} \int \langle \dot{\alpha}_{xx}(\tau)\dot{\alpha}_{xx}(t+\tau) \rangle_\tau \exp(-2\pi i c \widetilde{\nu} t) dt \tag{2.80}$$

and

$$I^{\perp}(\widetilde{\nu}) = \frac{h}{8\varepsilon_0^2 k_B T} \frac{(\widetilde{\nu}_{in} - \widetilde{\nu})^4}{\widetilde{\nu}(1 - \exp(-\frac{hc\widetilde{\nu}}{k_B T}))} \int \langle \dot{\alpha}_{xy}(\tau)\dot{\alpha}_{xy}(t+\tau) \rangle_\tau \exp(-2\pi i c \widetilde{\nu} t) dt, \tag{2.81}$$

where α denotes the polarization, h is the Planck constant and $\widetilde{\nu}_{in}$ is the laser wavenumber, which in all cases was set to 20000 cm^{-1}. The formula for random molecular orientation relative to the laboratory coordinate system is as follows:

$$I^{\parallel}(\widetilde{\nu}) = \frac{h}{8\varepsilon_0^2 k_B T} \frac{(\widetilde{\nu}_{in} - \widetilde{\nu})^4}{\widetilde{\nu}(1 - \exp(-\frac{hc\widetilde{\nu}}{k_B T}))} \frac{45a(\widetilde{\nu}) + 4\gamma(\widetilde{\nu})}{45} \tag{2.82}$$

and

$$I^{\perp}(\widetilde{\nu}) = \frac{h}{8\varepsilon_0^2 k_B T} \frac{(\widetilde{\nu}_{in} - \widetilde{\nu})^4}{\widetilde{\nu}(1 - \exp(-\frac{hc\widetilde{\nu}}{k_B T}))} \frac{3\gamma(\widetilde{\nu})}{45} \tag{2.83}$$

with the isotropic contribution

$$a(\widetilde{\nu}) = \int_{-\infty}^{\infty} \left\langle \frac{\dot{\alpha}_{xx}(\tau) + \dot{\alpha}_{yy}(\tau) + \dot{\alpha}_{zz}(\tau)}{3} \frac{\dot{\alpha}_{xx}(\tau+t) + \dot{\alpha}_{yy}(\tau+t) + \dot{\alpha}_{zz}(\tau+t)}{3} \right\rangle_\tau \exp(-2\pi i c \widetilde{\nu} t) dt \tag{2.84}$$

and the anisotropic contribution:

$$\begin{aligned}\gamma(\widetilde{\nu}) = \int_{-\infty}^{+\infty} \Big[& \frac{1}{2} \left\langle (\dot{\alpha}_{xx}(\tau) - \dot{\alpha}_{yy}(\tau))(\dot{\alpha}_{xx}(\tau+t) - \dot{\alpha}_{yy}(\tau+t)) \right\rangle_\tau \\ & + \frac{1}{2} \left\langle (\dot{\alpha}_{yy}(\tau) - \dot{\alpha}_{zz}(\tau))(\dot{\alpha}_{yy}(\tau+t) - \dot{\alpha}_{zz}(\tau+t)) \right\rangle_\tau \\ & + \frac{1}{2} \left\langle (\dot{\alpha}_{zz}(\tau) - \dot{\alpha}_{xx}(\tau))(\dot{\alpha}_{zz}(\tau+t) - \dot{\alpha}_{xx}(\tau+t)) \right\rangle_\tau \\ & + 3 \left\langle \dot{\alpha}_{xy}(\tau)\dot{\alpha}_{xy}(\tau+t) \right\rangle_\tau + 3 \left\langle \dot{\alpha}_{yz}(\tau)\dot{\alpha}_{yz}(\tau+t) \right\rangle_\tau \\ & + 3 \left\langle \dot{\alpha}_{zx}(\tau)\dot{\alpha}_{zx}(\tau+t) \right\rangle_\tau \Big] \exp\left(-2\pi i c \widetilde{\nu} t\right) \mathrm{d}t. \end{aligned} \tag{2.85}$$

2.8. Structural analyses

2.8.1. Radial pair Distribution functions and combined distribution functions

RDFs analysis, the most common kinds of trajectory analyses are particle density histograms, are widely used to obtain information about the system's structure by providing information on the average distance between two particles in the system.[148] In addition to simulation calculations, RDFs can also be calculated from the results of X-ray diffraction experiments.[149] For RDFs analysis, reference particles and observed particles can be selected from different molecules to obtain information about intermolecular properties, or reference particles and observed particles can be selected from the same molecule to obtain intramolecular information. The definition of RDFs in TRAVIS is provided:

$$g_{ab}(r) = \frac{V}{N_a N_b} \sum_{i=1}^{N_a} \sum_{j=i+1}^{N_b} \langle \delta(r - |\mathbf{r}_i(t) - \mathbf{r}_j(t)|) \rangle_t, \tag{2.86}$$

where r_i and r_j are the position vectors of the i-th and the j-th particle respectively. The δ presents the value 1 in the interval (with w being the bin width), otherwise is 0.[150]
Apart from the RDFs themselves, TRAVIS can also give the corresponding digital integral curve, which has a wide range of applications in evaluating the trajectories of different orbits and analyzing the exchange behavior of coordination molecules.[128,151]
TRAVIS can also provide histograms of other scalar data such as: angular distribution functions (ADFs), dihedral distribution functions (DDFs) and spatial distribution functions (SDFs). With TRAVIS, it is possible to use multi-dimensional histograms to understand the association effects, which are called combined distribution functions (CDFs). Thousands of CDFs can be obtained from the single trajectory through using the combination of distances, angles, dihedrals, point-plane distances, and point-line distances.[135,152–154] In addition, TRAVIS can even combine three scalars into a three-dimensional histogram.[155,156]

3. Locality in Amino-Acid Based Imidazolium Ionic Liquids

Wenbo Dong,* Vahideh Alizadeh,* Jan Blasius,* Luke Wylie,* Leonard Dick,* Zhijie Fan † and Barbara Kirchner*

Received: 8 June 2023, First published: 25 August 2023.

Reproduced in Appendix A from

W. Dong, V. Alizadeh, J. Blasius, L. Wylie, L. Dick, Z. Fan, B. Kirchner, *Phys. Chem. Chem. Phys.* **2023**, *25*, 24678-24685

doi:10.1039/D3CP02671J.

with permission from the Royal Society of Chemistry.‡

Contributions to the manuscript

- Development of the concept
- Performing all simulations, analysis, and calculations
- Interpretation of the results
- Writing of the manuscript

* Mulliken Center for Theoretical Chemistry, Clausius Institute for Physical and Theoretical Chemistry, University of Bonn, Beringstr. 4–6, 53115 Bonn, Germany

† Department of Chemistry, Imperial College London, South Kensington Campus, London SW7 2AZ, United Kingdom.

‡ Permission requests to reuse material from this chapter should be directed to the Royal Society of Chemistry.

Theoretical calculations can provide the fundamental understanding of the physical properties of ionic liquids (ILs). Several physical properties of ILs can be influenced by locality and fluctuations of dipole moments and polarization. In the following chapter, the authors focus on the electric dipole moment distribution and polarization of various ILs, as the means of characterizing and understanding these complex systems. Here, six types of amino acid (AA) ILs ([C_2C_1Im][ala], [C_2C_1Im][pro], [C_2C_1Im][his], [C_2C_1Im][trp], [C_2C_1Im][phe] and [C_2C_1Im][tyr]) are simulated using *ab initio* molecular dynamics (AIMD) with CP2K. By analyzing the trajectories obtained from simulations with TRAVIS, the dipole moment distributions for cations and anions are studied using the following methods: Wannier functions, Voronoi tessellation, as well as Blöchl, Löwdin and Mulliken charge schemes. The Wannier function is non-unique, due to the inherent uncertainty in the Bloch orbits, which can only be determined up to an arbitrary unitary transformations among all occupied orbitals at each point in the Brillouin zone. Maximally localized Wannier functions (MLWFs) provide detailed chemical analysis of bonding properties and their evolution during chemical reactions.[75] Therefore, they have become a well-established tool for post-processing electronic structure calculations. Voronoi tessellation accounts for variations in atomic sizes by adjusting the boundary planes to partition the electron density accordingly.

For cations, the dipole moment values are significantly lower value compared to those value of cations in the systems of 1-ethyl-3-methylimidazolium thiocyanate and 1-ethyl-3-methylimidazolium dicyanamide.[86] For anions, as the increase of size and polarization, the range of the dipole moment distribution exhibits a distinct enhancement. Specifically, we found that fluctuations in dipole moments are primarily determined by the anion rather than the cation. When calculated using Wannier and Voronoi methods, the cations show lower dipoles value compared to the anions. Furthermore, the Voronoi method yields lower dipole moment distributions than the Wannier method. Additionally, the analysis of electrostatic potentials showed the structural effects on the dipole moment values which can help explain the two dipole maxima in the Wannier center method and Voronoi method. The influence of charge calculation methods on dipole moment distribution was examined using the Blöchl, Löwdin and Mulliken charge schemes. When compared to the Blöchl and Löwdin charge scheme, the Mulliken charge scheme yields dipole moments that are closer to those obtained from the Wannier and Voronoi methods. Therefore, the Mulliken method is used in the next part: estimating monopole-dipole electrostatic interaction.

In monopole-dipole electrostatic interactions, the angular probability distribution was used to evaluate the degree of locality, which is between the dipole of one ion and the vector quantity from the ion center reference of other ions center of charge. Based on the previous results, the Mulliken charge scheme was selected. As a result of cos Φ (charge-dipole) and cos ϕ (dipole-dipole) of cations and anions separated by distance, when the distance was found to be over 700 pm, there was no preferential alignment.

As a further investigation, Voronoi tesselation was employed to predict dipole moments and polarization in [C_2C_1Im][ala] was be investigated by comparing the predicted infrared (IR) and Raman with experimental data. Herein, both IR and Raman spectroscopy agree with peak relative intensities and shapes of main peaks (around 1500 cm^{-1} and 3000 cm^{-1}). When comparing

with the experimental data, here is shown to be good correspondence.
In conclusion, this study focused on investigating the fluctuation and locality of dipole moments in six types of AA-ILs. The choice of ions used and the calculation method significantly influence the dipole moment and polarization. By employing different charge calculation schemes and theoretical approaches, we provided a comprehensive dataset for dipole moments and polarization in these systems. Furthermore, in theoretical calculations, it is possible to separate the infrared and Raman spectra of individual ions. This allows for the assignment of specific spectral signals to either cations or anions, which is not feasible in experimental studies. This work fills the gap in the systematic analysis of dipole moments in AA-ILs and provides valuable insights for future computational and experimental investigations.

4. Vibrational Spectra Simulations in Amino Acid-Based Imidazolium Ionic Liquids

Wenbo Dong,* , Jan Blasius,* Zhijie Fan,† and Luke Wylie*

Received: 19 April 2024, Published online: 29 June 2024.

Reprinted in Appendix B with permission from [**W. Dong**, J. Blasius, Z. Fan, L. Wylie, *J. Phys. Chem. B* **2024**, *128*, 6560-6566

doi:10.1021/acs.jpcb.4c02555.]. Copyright [2024] American Chemical Society.‡

For this article, Supporting Information is available free of charge at:
https://doi.org/10.1021/acs.jpcb.4c02555.

Contributions to the manuscript

- Development of the concept
- Performing all simulations, analysis, and calculations
- Co-performing visualizations
- Interpretation of the results
- Writing of the manuscript

*Mulliken Center for Theoretical Chemistry, Clausius Institute for Physical and Theoretical Chemistry, University of Bonn, Beringstr. 4–6, 53115 Bonn, Germany

†Department of Chemistry, Imperial College London, South Kensington Campus, London SW7 2AZ, United Kingdom

Theoretical chemistry plays a crucial role in spectral analysis, particularly in the interpretation and prediction of infrared (IR) and Raman spectra.[157] Through quantum chemical calculations and molecular dynamics simulations, we can accurately determine molecular vibration frequencies, assign spectral characteristic peaks, and reveal the relationship between molecular structure and spectral signals. This not only helps interpret experimental data, but also guides the design of new materials and chemical systems, and improves the accuracy and applicability of spectral analysis.

Ionic liquids (ILs) have attracted much attention in the fields of catalysis, energy storage and separation due to their unique physical and chemical properties, and spectroscopy, especially infrared and Raman spectroscopy, serves as a crucial tool for investigating their microstructure and interactions.[108,109] Theoretical chemical approaches, such as density functional theory (DFT) and molecular dynamics (MD) simulations, enable the accurate calculation of vibrational modes, hydrogen bond (HB) networks and ion interactions of ILs, thereby interpreting experimental spectral data. This combination of calculation and experiment not only deepens the understanding of the fundamental properties of ILs, but also provides theoretical guidance for their design and optimization in specific applications.

In the following chapter, all investigated ILs contain $[C_2C_1Im]^+$ as the cation to ensure consistency. In contrast, the anions analyzed consisted of a variety of deprotonated amino acids (AA): (L)-alaninate($[ala]^-$), (L)-prolinate ($[pro]^-$), (L)-histidinate ($[his]^-$), (L)-phenylalaninate ($[phe]^-$), (L)-tryptophanate ($[trp]^-$) and (L)-tyrosinate ($[tyr]^-$). Here, IR and Raman spectra for these ILs were computed using Voronoi tessellation and Wannier function centers. This study applies the ability to theoretically generate accurate infrared and Raman spectra using *ab initio* molecular dynamics (AIMD) simulations with the CP2K software. TRAVIS software was used to analyze the trajectories obtained from simulations.

In the case of IR spectra, the Voronoi tessellation and Wannier function methods were evaluated for their ability to accurately predict IR spectra for the full system, cation, and anion. The two methods exhibit relative consistency in the main peak positions, peak shapes, and relative intensities of the IR spectra, indicating their applicability in describing the molecular vibration modes of AA-ILs. Through spectral analysis, characteristic peaks associated with the vibration modes of the C-H bond in the imidazole ring and the AA side chain can be observed. The positions and intensities of these peaks are affected by the HB network.

In the case of Raman spectra, the Wannier localization does not converge to the same bonding mode in calculations with and without an external electric field. This inconsistency causes a flipping of the dipole vector, which strongly disturbs the dipole moment changes induced by the electric field. Therefore, only the Voronoi tessellation method was employed for Raman spectra (full system, cation, and anion). In all systems, the polarization differences of the cations were found to be negligible.

As a further investigation, a comparison between experimental and theoretical spectroscopy was conducted. Specifically, we examined the theoretical wavenumbers and the discrepancies between experimental and theoretical data for six ILs systems. The main characteristic peaks of the calculated IR and Raman spectra are consistent with experimental spectra, particularly

in the C-H stretching vibration (3000–3200 cm^{-1}) and imidazole ring deformation vibration (1400–1600 cm^{-1}) regions, and the peak position error is generally within 10-20 cm^{-1}.
This chapter presents the research on vibrational spectroscopy simulations of AA-ILs and analyzes the advantages and disadvantages of different dipole moment calculation methods. The findings demonstrate that the Voronoi method is more stable and reliable in calculating spectral intensity distributions, offering a robust computational tool for future ILs research. Additionally, the theoretical model developed in this study provides crucial support for the analysis of experimental spectra and lays the foundation for further exploration of ILs in catalysis, energy storage, and biomedical applications.

5. Aromatic-Aromatic Interactions and Hydrogen Bonding in Amino Acid Based Ionic Liquids

Wenbo Dong,* , Patrick R. Batista,* † Jan Blasius,* and Barbara Kirchner*

Received: 28 Jan 2025, First published: 31 Jan 2025.

Reproduced in Appendix C from

W. Dong, P. R. Batista, J. Blasius, B. Kirchner, *Phys. Chem. Chem. Phys.* **2025**, *27*, 4457-4466

doi:10.1039/D4CP04385E.

with permission from the Royal Society of Chemistry.‡

Contributions to the manuscript

- Development of the concept
- Performing all simulations, analysis, and calculations
- Interpretation of the results
- Writing of the manuscript

*Mulliken Center for Theoretical Chemistry, Clausius Institute for Physical and Theoretical Chemistry, University of Bonn, Beringstr. 4–6, 53115 Bonn, Germany

†Institute of Chemistry, University of Campinas, Monteiro Lobato, 270, Cidade Universitária, 13083-862, Campinas, São Paulo, Brazil.

The unique physicochemical properties of ionic liquids (ILs) originate from their complex micro-structures, especially hydrogen bonds (HB) networks, ion-ion interactions, and solvation effects. Theoretical chemistry methods, such as density functional theory (DFT) and molecular dynamics (MD) simulations, provide powerful tools for analyzing these microscopic interactions. DFT calculations accurately describe HBs in ILs and reveal their effects on viscosity, melting points, and ion mobility, while MD simulations explore the dynamic behavior of ILs, such as ion pair formation, nanoscale phase separation, and interfacial properties.[158,159] These theoretical studies not only deepen the understanding of the structure of ILs, but also provide important guidance for their applications in catalysis, energy storage, and separation.

Unlike traditional ILs, amino acid (AA) ILs introduce AA residues, making them exhibit more complex intermolecular interactions, which greatly affect their structure and function. Among these interactions, aromatic-aromatic interactions and HB are considered to be the key factors determining the properties of AA-ILs. However, the specific manifestations of these interactions in AA-ILs and their contributions to the stability of the system are still not fully understood. Therefore, Chapter 5 uses *ab initio* molecular dynamics (AIMD) simulations to study the molecular interactions in six different imidazolium AA-ILs ([C_2C_1Im][ala], [C_2C_1Im][pro], [C_2C_1Im][his], [C_2C_1Im][trp], [C_2C_1Im][phe] and [C_2C_1Im][tyr]), focusing on the cation-anion interactions, especially the π-π stacking and HB mechanisms. This study not only helps to reveal the basic structural characteristics of AA-ILs, but also provides important theoretical guidance for the design of future functional ILs.

Through the study of radial distribution functions (RDFs) and combined distribution functions (CDFs), it was found that there is a significant π-π stacking interaction between imidazolium cations, and the following conclusions were drawn: (i) π-π stacking mainly occurs in close-range interactions between cations and enhances the stability of the system. (ii) The strength of the π-π interaction depends on the selected amino acid anions, and different anions will affect the arrangement pattern of cations. (iii) π-π stacking helps to reduce the free volume of the system and improve the structural order These results demonstrate that by finely regulating the selection of cation–anion pairs, the stability and viscosity of AA-ILs can be optimized to meet different application needs. HB is another important stabilizing factor in AA-ILs. The study found that: the carboxylate on the AA anion is the main HB acceptor, the hydrogen atom on the imidazolium cation (especially C-H or N-H on the imidazole ring) forms a strong HB with the carboxylate of the anion, and the number and strength of HBs produced by different AA anions are different, which affect the solubility, viscosity and conductivity of AA-ILs. These results show that by optimizing the HB network of AA-ILs, their physicochemical properties can be further improved, making them more practical in fields such as biomedicine and catalysis.

The study also found that π-π stacking and HB are not independent but interrelated. Strong π-π interactions affect the formation of hydrogen bonds because the stacking pattern of cations changes the spatial arrangement of anions. The enhancement of the HB network may interfere with π-π stacking because the orientation of anions to cations affects the arrangement of their aromatic rings. The synergistic effects of π-π stacking and HB jointly determine the macrostructure and properties of AA-ILs. This study emphasizes that understanding the synergistic

effects of these non-covalent interactions is crucial for optimizing the molecular design of AA-ILs. The results of this chapter provide a molecular-level theoretical basis for optimizing the stability, viscosity, and solubility of AA-ILs. Since AA-ILs have potential uses in enzyme stabilization, drug delivery, and other fields, understanding their intermolecular interaction mechanisms will help develop bio-compatible solvents. The results of the π-π stacking and HB studies can be used to develop new soft materials with tunable physicochemical properties. Overall, this study laid a theoretical foundation for the rational design of functional ILs and promoted further development in the fields of green chemistry, biomedicine and advanced materials.

6. Summary and Outlook

Studying the polarization effect, spectral characteristics and molecular structure of ionic liquids (ILs) is crucial to understanding their microscopic mechanism of action, and *ab initio* Molecular Dynamics (AIMD), as a high-precision simulation method, plays an important role in this research field. It can not only capture the electronic polarization effect, but also accurately calculate the spectral characteristics and deeply analyze the molecular structure and dynamic behavior of ILs. With the development of machine learning and multi-scale simulation methods, AIMD will play a more important role in the study of ILs at a larger scale. This paper uses CP2K software to perform AIMD simulations and is dedicated to gaining a deeper understanding of amino acid-based (AA) imidazolium ILs, which have attracted widespread attention due to their unique structural and functional properties.

In ILs, polarization effects play a crucial role in their structural, dynamical, and spectral properties. In chapter 3, the main focus is on the local polarization properties of AA-ILs. The AIMD method is used, combined with different charge distribution schemes (such as Wannier function, Blöchl, Löwdin, Mulliken method and Voronoi tessellation), to systematically analyze the distribution of electric dipole moments and polarization behavior of cations and anions in ILs, and study the effectiveness of these methods in predicting dipole moments. The results show that cations and anions have different contributions to the polarization of the system, and choosing a suitable charge distribution method is crucial for accurately predicting the dipole moment. In addition, the localization of the monopole-dipole electrostatic interaction is evaluated using the angle probability distribution, and it is found that no preferred orientation is shown even within the range of 700 pm. IR and Raman spectra analysis of the $[C_2C_1Im][ala]$ system showed that the main signal peaks were consistent with the experimental results and could distinguish the contributions of cations and anions in the ILs. The extension of this research can focus on the structural and functional properties of ILs derived from different AAs, and their potential in various applications. In particular, a deeper understanding of the polarization behavior and localization of ILs will help design ILs with specific properties to meet the needs of different fields.

In recent years, AA-ILs have attracted extensive attention in the fields of catalysis, energy storage, and bio-compatible materials due to their unique physicochemical properties. However, the microstructure, dipole moment distribution, and influence of this type of ILs on vibrational spectra are still lacking in systematic research. In chapter 4, AIMD simulations were used, combined with the maximum localized Wannier function and the Voronoi tessellation method, to systematically analyze the dipole moment distribution of several typical AA-ILs and calculate their vibrational spectra. The study found that the polarity and HB of different AAs side chains

have an important influence on the local changes in the dipole moment, resulting in subtle differences in the vibrational spectra. In addition, the study further verified the reliability of the AIMD method in analyzing the spectral characteristics of ILs, providing theoretical guidance for experimental studies. Combining experimental data with simulation results can deepen the understanding of the relationship between the microstructure and macroscopic properties of ILs, thereby guiding the design and application of new functional ILs, especially in the fields of electrochemistry, drug delivery and nano-materials.

Chapter 5 used AIMD to systematically study the intermolecular interactions of six AA-ILs. Through the analysis of radial distribution functions (RDFs) and combined distribution functions (CDFs), significant cation-anion, cation-cation, and anion-anion interactions were presented in these ILs. Among them, the cations and anions are mainly bound by π-π interactions. In addition, the study also identified the existence of multiple hydrogen bonds, especially the hydrogen bonds between the carboxylic acid group of the anion and the hydrogen atoms on the cation ring. These detailed analyzes revealed the spatial configuration of the studied system and the key interactions that maintain its structural stability. These findings make AA-ILs have potential application value as chiral solvents and for the dissolution and stabilization of biomolecules. This study helps to further explore the effects of different AA side chains on the intermolecular interactions of ILs in order to design ionic liquids with specific functions. In addition, combining computational simulations with experimental studies will help to deeply understand the application potential of these ILs in fields such as biomedicine and catalysis. In particular, it will be of great significance to carry out systematic research on their application prospects in chiral separation, bio-molecule stabilization, and green catalysts.

Furthermore, this thesis of these microscopic interactions and dipole moment characteristics also provides new ideas for the application of ILs in interface and surface science. For example, surface nonlinear spectroscopy techniques, such as sum-frequency generation spectroscopy (SFG), can be used to study the molecular arrangement and dipole orientation of ILs at solid-liquid or liquid-gas interfaces.[160,161] SFG technology is particularly sensitive to interfacial molecules with non-centrosymmetric structures, and can therefore help reveal the ordered structures formed by ILs on the surface and their interactions with substrate materials. In addition, since ILs are often used as surfactants or solvents in catalysis and separation technology, changes in their surface dipole moments may directly affect reaction kinetics and mass transfer processes, which are all worthy of further study.

7. Bibliography

[1] T. Welton, *Chem. Rev.* **1999**, *99*, 2071–2084.

[2] J. S. Wilkes, *Green Chem.* **2002**, *4*, 73–80.

[3] K. Ghandi, *GSC* **2014**, *4*, 44–53.

[4] Y. Marcus, *From Molten Salts to RTILs. Cham, sl: Springer International Publishing.* **2016**.

[5] K. Fumino, R. Ludwig, *J. Mol. Liq.* **2014**, *192*, 94–102.

[6] P. Walden, *Bull. Acad. Imper. Sci.(St. Petersburg)* **1914**, *1800*.

[7] D. R. MacFarlane, M. Forsyth, E. I. Izgorodina, A. P. Abbott, G. Annat, K. Fraser, *Phys. Chem. Chem. Phys.* **2009**, *11*, 4962–4967.

[8] F. H. Hurley, T. P. WIer, *J. Electrochem. Soc.* **1951**, *98*, 207.

[9] C. L. Hussey, T. Scheffler, J. S. Wilkes, A. Fannin, *J. Electrochem. Soc.* **1986**, *133*, 1389.

[10] J. S. Wilkes, J. A. Levisky, R. A. Wilson, C. L. Hussey, *Inorg. Chem.* **1982**, *21*, 1263–1264.

[11] J. S. Wilkes, M. J. Zaworotko, *Supramol. Chem.* **1993**, *1*, 191–193.

[12] E. I. Cooper, E. J. O'Sullivan, *Energy Environ. Sci.* **1992**, *1992*, 386.

[13] C. A. Angell, Y. Ansari, Z. Zhao, *Faraday Discuss.* **2012**, *154*, 9–27.

[14] J. Holbrey, N. Plechkova, K. Seddon, *Green Chem.* **2006**, *8*, 411–414.

[15] A. J. Greer, J. Jacquemin, C. Hardacre, *Mol.* **2020**, *25*, 5207.

[16] M. Koel, *Ionic liquids in chemical analysis*, CRC press, **2008**.

[17] R. D. Rogers, K. R. Seddon, *Sci.* **2003**, *302*, 792–793.

[18] S. A. Forsyth, J. M. Pringle, D. R. MacFarlane, *Aust. J. Chem.* **2004**, *57*, 113–119.

[19] Z. Lei, C. Dai, J. Hallett, M. Shiflett, *Introduction: Ionic liquids for diverse applications*, **2024**.

[20] P. C. Marr, A. C. Marr, *Green Chem.* **2016**, *18*, 105–128.

[21] S. K. Singh, A. W. Savoy, *J. Mol. Liq.* **2020**, *297*, 112038.

[22] S. Zein El Abedin, F. Endres, *Acc. Chem. Res.* **2007**, *40*, 1106–1113.

[23] R. Hayes, G. G. Warr, R. Atkin, *Chem. Rev.* **2015**, *115*, 6357–6426.

[24] V. A. Parsegian, *Van der Waals forces: a handbook for biologists, chemists, engineers, and physicists*, Cambridge university press, **2005**.

[25] W. R. Bowen, F. Jenner, *Adv. Colloid Interface Sci.* **1995**, *56*, 201–243.

[26] A. Ray, *Nat.* **1971**, *231*, 313–315.

[27] G. A. Jeffrey, G. A. Jeffrey, *An introduction to hydrogen bonding*, *Vol. 12*, Oxford university press New York, **1997**.

[28] P. Metrangolo, G. Resnati, *Halogen bonding: fundamentals and applications*, *Vol. 126*, Springer, **2008**.

[29] W. Dong, V. Alizadeh, J. Blasius, L. Wylie, L. Dick, Z. Fan, B. Kirchner, *Phys. Chem. Chem. Phys.* **2023**, *25*, 24678–24685.

[30] A. M. Fernandes, M. A. Rocha, M. G. Freire, I. M. Marrucho, J. A. Coutinho, L. M. Santos, *J. Phys. Chem. B.* **2011**, *115*, 4033–4041.

[31] T. Welton, *Chem. Rev.* **2004**, *99*, 2071–2083.

[32] T. L. Greaves, C. J. Drummond, *Chem. Rev.* **2008**, *108*, 206–237.

[33] M. J. Earle, J. M. Esperança, M. A. Gilea, J. N. Canongia Lopes, L. P. Rebelo, J. W. Magee, K. R. Seddon, J. A. Widegren, *Nat.* **2006**, *439*, 831–834.

[34] J. Han, A. Mariani, S. Passerini, A. Varzi, *Energy Environ. Sci.* **2023**, *16*, 1480–1501.

[35] S. Gehrke, B. Kirchner, *J. Chem. Eng. Data* **2019**, *65*, 1146–1158.

[36] M. A. Ortuno, O. Holloczki, B. Kirchner, N. Lopez, *J. Phys. Chem. Lett.* **2019**, *10*, 513–517.

[37] J. Blasius, R. Elfgen, O. Hollóczki, B. Kirchner, *Phys. Chem. Chem. Phys.* **2020**, *22*, 10726–10737.

[38] R. Clark, M. von Domaros, A. J. McIntosh, A. Luzar, B. Kirchner, T. Welton, *J. Chem. Phys.* **2019**, *151*.

[39] F. Malberg, O. Hollóczki, M. Thomas, B. Kirchner, *Struct. Chem.* **2015**, *26*, 1343–1349.

[40] B. Bhargava, S. Balasubramanian, *J. Am. Chem. Soc.* **2006**, *128*, 10073–10078.

[41] F. Biscay, A. Ghoufi, V. Lachet, P. Malfreyt, *J. Phys. Chem. C* **2011**, *115*, 8670–8683.

[42] H. Huber, A. J. Dyson, B. Kirchner, *Chem. Soc. Rev.* **1999**, *28*, 121–133.

[43] E. J. Maginn, *J. Condens. Matter Phys.* **2009**, *21*, 373101.

[44] H. M. Senn, W. Thiel, *Atomistic approaches in modern biology: from quantum chemistry to molecular simulations* **2007**, 173–290.

[45] E. Maginn, J. Elliott, *Ind. Eng. Chem. Res.* **2010**, *49*, 3059–3078.

[46] K. Kadau, J. L. Barber, T. C. Germann, B. L. Holian, B. J. Alder, *Philos. Trans. R. Soc. A* **2010**, *368*, 1547–1560.

[47] Y.-L. Wang, B. Li, S. Sarman, F. Mocci, Z.-Y. Lu, J. Yuan, A. Laaksonen, M. D. Fayer, *Chem. Rev.* **2020**, *120*, 5798–5877.

[48] H. Weingärtner, *Angew. Chem. Int. Ed.* **2008**, *47*, 654–670.

[49] R. Lynden-Bell, *Mol. Phys.* **2003**, *101*, 2625–2633.

[50] M. Lísal, *J. Chem. Phys.* **2013**, *139*, 214701.

[51] M. Campetella, M. Montagna, L. Gontrani, E. Scarpellini, E. Bodo, *Phys. Chem. Chem. Phys.* **2017**, *19*, 11869–11880.

[52] X. Paredes, J. Fernandez, A. A. Padua, P. Malfreyt, F. Malberg, B. Kirchner, A. S. Pensado, *J. Phys. Chem. B.* **2012**, *116*, 14159–14170.

[53] K. Wendler, F. Dommert, Y. Y. Zhao, R. Berger, C. Holm, L. Delle Site, *Faraday Discuss.* **2012**, *154*, 111–132.

[54] N. Rohman, N. N. Dass, S. Mahiuddin, *J. Chem. Eng. Data* **1999**, *44*, 465–472.

[55] R. Abraham, M. Abdulkhadar, C. Asokan, *J. Chem. Thermodyn.* **2000**, *32*, 1–16.

[56] H. Ohno, K. Fukumoto, *Acc. Chem. Res.* **2007**, *40*, 1122–1129.

[57] P. Ossowicz, J. Klebeko, B. Roman, E. Janus, Z. Rozwadowski, *Mol.* **2019**, *24*, 3252.

[58] G.-h. Tao, L. He, W.-s. Liu, L. Xu, W. Xiong, T. Wang, Y. Kou, *Green Chem.* **2006**, *8*, 639–646.

[59] J. Kagimoto, K. Fukumoto, H. Ohno, *ChemComm* **2006**, 2254–2256.

[60] Z. Song, Y. Liang, M. Fan, F. Zhou, W. Liu, *RSC Adv.* **2014**, *4*, 19396–19402.

[61] Q.-P. Liu, X.-D. Hou, N. Li, M.-H. Zong, *Green Chem.* **2012**, *14*, 304–307.

[62] J. Tong, M. Hong, Y. Chen, H. Wang, J.-Z. Yang, *J. Chem. Eng. Data* **2012**, *57*, 2265–2270.

[63] D. H. Dagade, S. P. Shinde, K. R. Madkar, S. S. Barge, *J. Chem. Thermodyn.* **2014**, *79*, 192–204.

[64] P. Ossowicz, E. Janus, G. Schroeder, Z. Rozwadowski, *Mol.* **2013**, *18*, 4986–5004.

[65] C. Herrera, M. Atilhan, S. Aparicio, *Phys. Chem. Chem. Phys.* **2018**, *20*, 10213–10223.

[66] R. Bader, A. Larouche, C. Gatti, M. Carroll, P. MacDougall, K. Wiberg, *J. Chem. Phys.* **1987**, *87*, 1142–1152.

[67] J. Antosiewicz, *Biophys. J.* **1995**, *69*, 1344–1354.

[68] A. V. Gubskaya, P. G. Kusalik, *J. Chem. Phys.* **2002**, *117*, 5290–5302.

[69] P. Debye, *Nobel Lectures, Chem.* **1922**, *1941*, 383–401.

[70] M. Thomas, M. Brehm, B. Kirchner, *Phys. Chem. Chem. Phys.* **2015**, *17*, 3207–3213.

[71] G. H. Wannier, *Phys. Rev.* **1937**, *52*, 191.

[72] B. Kirchner, J. Hutter, *J. Chem. Phys.* **2004**, *121*, 5133–5142.

[73] M.-P. Gaigeot, R. Vuilleumier, M. Sprik, D. Borgis, *J. Chem. Theory Comput.* **2005**, *1*, 772–789.

[74] S. Zahn, K. Wendler, L. Delle Site, B. Kirchner, *Phys. Chem. Chem. Phys.* **2011**, *13*, 15083–15093.

[75] N. Marzari, A. A. Mostofi, J. R. Yates, I. Souza, D. Vanderbilt, *RMP* **2012**, *84*, 1419–1475.

[76] S. F. Boys, *RMP* **1960**, *32*, 296.

[77] S. Boys, P. Löwdin, *AP, NY* **1966**, 253.

[78] W. Kohn, L. J. Sham, *Phys. Rev.* **1965**, *140*, A1133.

[79] N. Marzari, D. Vanderbilt, *Phys. Rev. B* **1997**, *56*, 12847.

[80] T. A. Manz, D. S. Sholl, *J. Chem. Theory Comput.* **2012**, *8*, 2844–2867.

[81] P. Bultinck, C. Van Alsenoy, P. W. Ayers, R. Carbó-Dorca, *J. Chem. Phys.* **2007**, *126*.

[82] R. F. Bader, *Chem. Rev.* **1991**, *91*, 893–928.

[83] M. Brehm, M. Thomas, *Mol.* **2021**, *26*, 1875.

[84] W. Pokojski, P. Pokojska, *Pol. Cartogr. Rev.* **2018**, *50*, 141–150.

[85] C. E. R. Prado, M. G. D. Pópolo, T. Youngs, J. Kohanoff, R. M. Lynden-Bell, *Mol. Phys.* **2006**, *104*, 2477–2483.

[86] K. Wendler, S. Zahn, F. Dommert, R. Berger, C. Holm, B. Kirchner, L. Delle Site, *J. Chem. Theory Comput.* **2011**, *7*, 3040–3044.

[87] M. Thomas, M. Brehm, R. Fligg, P. Vöhringer, B. Kirchner, *Phys. Chem. Chem. Phys.* **2013**, *15*, 6608–6622.

[88] M. Thomas, M. Brehm, O. Hollóczki, Z. Kelemen, L. Nyulászi, T. Pasinszki, B. Kirchner, *J. Chem. Phys.* **2014**, *141*, 1024510.

[89] M. Thomas, B. Kirchner, *J. Phys. Chem. Lett.* **2016**, *7*, 509–513.

[90] M. Brehm, M. Thomas, *J. Phys. Chem. Lett.* **2017**, *8*, 3409–3414.

[91] M. Brehm, M. Thomas, *J. Chem. Theory Comput.* **2019**, *15*, 3901–3905.

[92] C. A. Cassity, B. Siu, M. Soltani, J. L. McGeehee, K. J. Strickland, M. Vo, E. A. Salter, A. C. Stenson, A. Wierzbicki, K. N. West, et al., *Phys. Chem. Chem. Phys.* **2017**, *19*, 31560–31571.

[93] M.-P. Gaigeot, M. Martinez, R. Vuilleumier, *Mol. Phys.* **2007**, *105*, 2857–2878.

[94] B. Stuart, *Kirk-Othmer encyclopedia of chemical technology* **2000**.

[95] N. L. Alpert, W. E. Keiser, H. A. Szymanski, *IR: theory and practice of infrared spectroscopy*, Springer Science & Business Media, **2012**.

[96] S. Raugei, F. L. Gervasio, P. Carloni, *Phys. Status Solidi B* **2006**, *243*, 2500–2515.

[97] F. Neese, *J. Biol. Inorg. Chem.* **2006**, *11*, 702–711.

[98] P. Geerlings, *Pharm.* **2022**, *15*, 1112.

[99] M. Orio, D. A. Pantazis, F. Neese, *Photosynth. Res.* **2009**, *102*, 443–453.

[100] N. A. Besley, *Acc. Chem. Res.* **2020**, *53*, 1306–1315.

[101] J. Autschbach, *Coord. Chem. Rev.* **2007**, *251*, 1796–1821.

[102] A. Lavrentyev, B. Gabrelian, V. Vu, N. Denysyuk, P. Shkumat, A. Tarasova, L. Isaenko, O. Khyzhun, *Opt. Mater.* **2016**, *53*, 64–72.

[103] P. L. Silvestrelli, M. Bernasconi, M. Parrinello, *Chem. Phys. Lett.* **1997**, *277*, 478–482.

[104] J. M. Bowman, *Acc. Chem. Res.* **1986**, *19*, 202–208.

[105] J. O. Jung, R. B. Gerber, *Chem. Phys.* **1996**, *105*, 10332–10348.

[106] C. Cappelli, S. Monti, G. Scalmani, V. Barone, *J. Chem. Theory Comput.* **2010**, *6*, 1660–1669.

[107] S. A. Fischer, T. W. Ueltschi, P. Z. El-Khoury, A. L. Mifflin, W. P. Hess, H.-F. Wang, C. J. Cramer, N. Govind, *J. Phys. Chem. B.* **2016**, *120*, 1429–1436.

[108] V. H. Paschoal, L. F. Faria, M. C. Ribeiro, *Chem. Rev.* **2017**, *117*, 7053–7112.

[109] A. Wulf, K. Fumino, D. Michalik, R. Ludwig, *ChemPhysChem* **2007**, *8*, 2265–2269.

[110] Y.-l. Yang, Y. Kou, *Chemcomm* **2004**, 226–227.

[111] K. Iwata, H. Okajima, S. Saha, H.-o. Hamaguchi, *Acc. Chem. Res.* **2007**, *40*, 1174–1181.

[112] R. Futrelle, D. McGinty, *Chem. Phys. Lett.* **1971**, *12*, 285–287.

[113] J. Mahanty, B. Ninham **1976**.

[114] J. Wilkes, M. Zaworotko, *J. Chem. Soc., Chem. Commun.* **1992**, *965*, 967.

[115] J. D. Holbrey, W. M. Reichert, R. D. Rogers, *Dalton Trans.* **2004**, 2267–2271.

[116] J. J. Golding, D. R. MacFarlane, L. Spiccia, M. Forsyth, B. W. Skelton, A. H. White, *ChemComm* **1998**, 1593–1594.

[117] P. M. Dean, J. M. Pringle, D. R. MacFarlane, *Phys. Chem. Chem. Phys.* **2010**, *12*, 9144–9153.

[118] M. G. Del Pópolo, G. A. Voth, *J. Phys. Chem. B.* **2004**, *108*, 1744–1752.

[119] V. I. Korsunskiy, R. B. Neder, A. Hofmann, S. Dembski, C. Graf, E. Rühl, *Appl. Crystallogr.* **2007**, *40*, 975–985.

[120] R. E. Skyner, J. B. Mitchell, C. Groom, *CrystEngComm* **2017**, *19*, 641–652.

[121] F. Sessa, P. D'Angelo, V. Migliorati, *Chem. Phys. Lett.* **2018**, *691*, 437–443.

[122] C. Hardacre, J. D. Holbrey, S. J. McMath, D. T. Bowron, A. K. Soper, *J. Chem. Phys.* **2003**, *118*, 273–278.

[123] C. Hardacre, J. D. Holbrey, M. Nieuwenhuyzen, T. G. Youngs, *Acc. Chem. Res.* **2007**, *40*, 1146–1155.

[124] C. Nieto de Castro, M. Lourenço, A. Ribeiro, E. Langa, S. Vieira, P. Goodrich, C. Hardacre, *J. Chem. Eng. Data.* **2010**, *55*, 653–661.

[125] P. Kadlubanski, K. Calderon-Mojica, W. A. Rodriguez, D. Majumdar, S. Roszak, J. Leszczynski, *J. Phys. Chem. A* **2013**, *117*, 7989–8000.

[126] S. S. Rao, S. P. Gejji, *J. Phys. Chem. A* **2016**, *120*, 5665–5684.

[127] A. A. Rodríguez-Sanz, E. M. Cabaleiro-Lago, J. Rodríguez-Otero, *Org. Biomol. Chem.* **2015**, *13*, 7961–7972.

[128] M. Brehm, B. Kirchner, *TRAVIS-a free analyzer and visualizer for Monte Carlo and molecular dynamics trajectories*, **2011**.

[129] I. T. Todorov, W. Smith, K. Trachenko, M. T. Dove, *J. Mater. Chem.* **2006**, *16*, 1911–1918.

[130] D. A. Case, T. E. Cheatham III, T. Darden, H. Gohlke, R. Luo, K. M. Merz Jr, A. Onufriev, C. Simmerling, B. Wang, R. J. Woods, *J. Comput. Chem.* **2005**, *26*, 1668–1688.

[131] M. Brehm, M. Thomas, *J. Chem. Inf. Model.* **2018**, *58*, 2092–2107.

[132] W. Humphrey, A. Dalke, K. Schulten, *J. Mol. Graph.* **1996**, *14*, 33–38.

[133] P. Turner, *Center for coastal and land-margin research, Oregon Graduate Institute of Science and Technology, Beaverton, OR* **2005**, *2*, 19.

[134] J. Opiła in *2016 39th International Convention on Information and Communication Technology, Electronics and Microelectronics (MIPRO)*, IEEE, pp. 343–348.

[135] M. Brehm, M. Thomas, S. Gehrke, B. Kirchner, *J. Chem. Phys.* **2020**, *152*.

[136] M. P. Allen, D. J. Tildesley, *Computer simulation of liquids*, Oxford university press, **2017**.

[137] M. Born, K. Huang, *Dynamical theory of crystal lattices*, Oxford university press, **1996**.

[138] D. Marx, J. Hutter, *Modern methods and algorithms of quantum chemistry* **2000**, *1*, 141.

[139] M. E. Tuckerman, M. Parrinello, *J. Chem. Phys.* **1994**, *101*, 1302–1315.

[140] A. Putrino, D. Sebastiani, M. Parrinello, *J. Chem. Phys.* **2000**, *113*, 7102–7109.

[141] C. Krekeler, F. Dommert, J. Schmidt, Y. Zhao, C. Holm, R. Berger, L. Delle Site, *Phys. Chem. Chem. Phys.* **2010**, *12*, 1817–1821.

[142] D. McQuarrie, *Harper's chemistry series (Harper & Row, New York, 1975)"Portions of this work were originally published under the title: Statistical thermodynamics* **1975**.

[143] J. Neugebauer, M. Reiher, C. Kind, B. A. Hess, *J. Comput. Chem.* **2002**, *23*, 895–910.

[144] D. C. Harris, M. D. Bertolucci, *Symmetry and spectroscopy: an introduction to vibrational and electronic spectroscopy*, Courier Corporation, **1989**.

[145] A. Smekal, *Naturwissenschaften* **1923**, *11*, 873–875.

[146] C. V. Raman, *Ind. J. Phys.* **1928**, *2*, 387–398.

[147] G. Placzek, *Z. Phys.* **1931**, *70*, 84–103.

[148] D. McQuarrie, *Statistical Mechanics, Harper &*, **1976**.

[149] T. Head-Gordon, G. Hura, *Chem. Rev.* **2002**, *102*, 2651–2670.

[150] J. Thar, M. Brehm, A. P. Seitsonen, B. Kirchner, *J. Phys. Chem. B* **2009**, *113*, 15129–15132.

[151] K. A. Röhrig, T. D. Kühne, *Phys. Rev. E Stat. Nonlin. Soft Matter Phys.* **2013**, *87*, 045301.

[152] M. Brüssel, M. Brehm, T. Voigt, B. Kirchner, *Phys. Chem. Chem. Phys.* **2011**, *13*, 13617–13620.

[153] A. S. Pensado, M. Brehm, J. Thar, A. P. Seitsonen, B. Kirchner, *ChemPhysChem* **2012**, *13*, 1845–1853.

[154] M. Brehm, H. Weber, A. S. Pensado, A. Stark, B. Kirchner, *Phys. Chem. Chem. Phys.* **2012**, *14*, 5030–5044.

[155] M. Bruessel, M. Brehm, A. S. Pensado, F. Malberg, M. Ramzan, A. Stark, B. Kirchner, *Phys. Chem. Chem. Phys.* **2012**, *14*, 13204–13215.

[156] M. Macchiagodena, G. Mancini, M. Pagliai, G. Cardini, V. Barone, *Int. J. Quantum Chem.* **2018**, *118*, e25554.

[157] R. R. Jones, D. C. Hooper, L. Zhang, D. Wolverson, V. K. Valev, *Nanoscale Res. Lett.* **2019**, *14*, 1–34.

[158] P. A. Hunt, C. R. Ashworth, R. P. Matthews, *Chem. Soc. Rev.* **2015**, *44*, 1257–1288.

[159] K. Low, S. Y. Tan, E. I. Izgorodina, *Frontiers Chem.* **2019**, *7*, 208.

[160] F. Vidal, A. Tadjeddine, *Rep. Prog. Phys.* **2005**, *68*, 1095.

[161] S. Baldelli, *J. Phys. Chem. Lett.* **2013**, *4*, 244–252.

A. Locality in Amino-Acid Based Imidazolium Ionic Liquids

Wenbo Dong,* Vahideh Alizadeh,* Jan Blasius,* Luke Wylie,* Leonard Dick,* Zhijie Fan † and Barbara Kirchner*

Received: 8 June 2023, First published: 25 August 2023.

Reproduced from Ref.

W. Dong, V. Alizadeh, J. Blasius, L. Wylie, L. Dick, Z. Fan, B. Kirchner, *Phys. Chem. Chem. Phys.* **2023**, *25*, 24678-24685

doi:10.1039/D3CP02671J.

with permission from the Royal Society of Chemistry.‡

Contributions to the manuscript

- Development of the concept
- Performing all simulations, analysis, and calculations
- Interpretation of the results
- Writing of the manuscript

* Mulliken Center for Theoretical Chemistry, Clausius Institute for Physical and Theoretical Chemistry, University of Bonn, Beringstr. 4–6, 53115 Bonn, Germany

† Department of Chemistry, Imperial College London, South Kensington Campus, London SW7 2AZ, United Kingdom.

PCCP

ROYAL SOCIETY OF CHEMISTRY

PAPER

View Article Online
View Journal | View Issue

Cite this: *Phys. Chem. Chem. Phys.*, 2023, **25**, 24678

Locality in amino-acid based imidazolium ionic liquids†

Wenbo Dong,[a] Vahideh Alizadeh,[a] Jan Blasius,[a] Luke Wylie,[a] Leonard Dick,[a] Zhijie Fan[b] and Barbara Kirchner*[a]

Several amino-acid based imidazolium ILs are investigated through the use of *ab initio* molecular dynamics (AIMD), which includes full polarization. The electric dipole moment distribution and polarization is used as a means of characterizing and understanding these complex systems. Various charge scheme methods were analyzed (Wannier function, Blöchl, Löwdin and Mulliken charge schemes and Voronoi tessellation) to determine their ability to predict dipole moments. These results and the following comparison of methods further deepen the knowledge of polarization by highlighting the importance of the anion and cation separately on polarizability contribution and the need to select a suitable method to predict these. The angular probability distribution is utilized to measure the degree of locality in monopole-dipole electrostatic interactions, which showed no preferential alignment over 700 pm. In addition, the IR and Raman spectra from Voronoi tessellation of $[C_2C_1Im][ala]$ were analyzed. In these, the strongest signalling peaks showed consistency with experiment and the ability to differentiate between anion and cation components of the IL.

Received 8th June 2023,
Accepted 24th August 2023

DOI: 10.1039/d3cp02671j

rsc.li/pccp

1. Introduction

Ionic liquids (ILs)[1] are defined as liquids that are composed entirely of ions in a liquid state below 100 °C.[2–5] In ionic compounds, the main interaction force between anions and cations is Coulombic interactions.[6] The larger the ionic radius, the smaller the force between molecules and the lower the melting point of this ionic compound.[7] The interaction energy between ions has been found to be highly dependent on the charge density.[8] The charge density is related to the magnitude and distribution of the charges of anions and cations. At present, environmental protection and sustainable resources are key factors driving the research in many countries and regions. As a result of ILs being non-volatile and non-flammable, they can be utilized as effective solvents, which are characterized by their recycling capabilities, ease of control and product recovery.[9] Moreover, the electrical conductivity of ILs is susceptible to many factors, such as temperature, pressure and the composition of mixtures (concentration of ILs in mixtures).[10–13] Room temperature ILs have been successfully used as mediators for green synthesis to achieve many important reactions.[14] Due to the many combinations of cations and anions, ILs are highly customizable for individual applications, with the possibility of least 1 million binary IL combinations and 10^{18} combinations of ternary ILs.[1,15] ILs have good solubility for many inorganic salts and organic substances, as a result they are widely used in many fields, including solvent extraction and preparation of inorganic or hybrid materials.[16–20]

In the field of sustainable chemistry, research into ILs carries significant potential and many relevant applications. As a result of this, it is important to understand the physical properties of ILs to be able to apply them as suitable solvents in each individual circumstance. To gain this fundamental understanding, theoretical calculations are often applied on the liquid–gas interface of different solutions (including ILs). These studies have analyzed a variety of different properties,[3,21–24] such as structure analysis of the liquid–gas interface in the IL ($[C_4C_1Im][PF_6]$) in a study by Bhargava *et al.*[25] or the surface tension of the liquid–vapor interface for alcohols.[26] Molecular dynamics (MD) simulations can provide a molecular-level view into the relationship between macroscopic and microscopic properties,[27] and give greater understanding behind the factors affecting the physical interface properties of ILs. There are several previous studies examining ILs using the DFT based *ab initio* molecular dynamics (AIMD) method to calculate important physical properties.[28–30] In particular, the physical properties calculated have included the study of the structure of the liquid gas-interface.[31] In addition, the electric

[a] *Mulliken Center for Theoretical Chemistry, University of Bonn, Beringstraße 4+6, D-53115 Bonn, Germany. E-mail: kirchner@thch.uni-bonn.de*
[b] *Department of Chemistry, Imperial College London, South Kensington Campus, London SW7 2AZ, UK*

† Electronic supplementary information (ESI) available. See DOI: https://doi.org/10.1039/d3cp02671j

dipole moment of an ion serves as a physical indicator of its electronic structure in ILs with electric dipole moment fluctuations being dependent on polarization.[32]

In a prior study, different kinds of 1-ethyl-3-methylimidazolium ($[C_2C_1Im]^+$) based ILs have been investigated by Car–Parrinello simulations to indicate that several physical properties can be affected by locality and fluctuations.[33] In addition, changing the dipole moment can also affect physical properties of ILs, for example increasing the dipole moment in cations can cause a decrease in the melting point.[34] To delve deeper into the physical properties of ILs, the magnitude and cause of the dipole moment and polarization must first be understood. This study will aim to give a more thorough understanding of important molecular properties of unique IL combinations. In order to achieve this goal, the liquid dynamics, including localities and fluctuations must first be considered. Here, we want to further investigate these properties through AIMD simulations of amino acid based ILs. Several different amino acids have been selected as anions, these will be paired with 1-ethyl-3-methylimidazolium ($[C_2C_1Im]^+$) as the cation. We will observe the dipole moment distributions, as well as the degree of locality in these IL systems and calculate IR and Raman spectra to validate theoretical predictions.

2. Systems investigated

ILs selected for investigation all contained $[C_2C_1Im]^+$ as the cation to maintain consistency. In contrast, the anions analyzed consisted of a variety of deprotonated amino acids: L-alaninate ($[ala]^-$), L-prolinate ($[pro]^-$), L-histidinate ($[his]^-$), L-phenylalaninate ($[phe]^-$), L-tryptophanate ($[trp]^-$) and L-tyrosinate ($[tyr]^-$), as shown in Fig. 1. These ILs were previously investigated using nuclear magnetic resonance (NMR) and Fourier-transform infrared spectroscopy (FTIR) analyses to study physical properties and their mechanism of SO_2 absorption, which has drawn much attention for use in environmental protection.[35]

All IL simulations were conducted using 16 ion pairs, as it was shown previously that at least 8 ion pairs were required to capture local effects.[33] Table 1 shows the theoretical densities, compositions and box sizes.

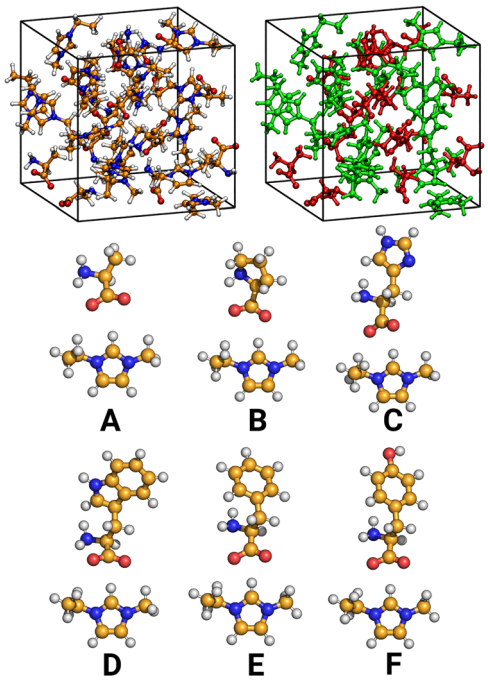

Fig. 1 Snapshots of the $[C_2C_1Im][ala]$ simulation box. Below this, the different ion pairs are depicted. (A) $[C_2C_1Im][ala]$; (B) $[C_2C_1Im][pro]$; (C) $[C_2C_1Im][his]$; (D) $[C_2C_1Im][trp]$; (E) $[C_2C_1Im][phe]$; (F) $[C_2C_1Im][tyr]$. The color code for the ball-and stick images as well as for the left simulation box is carbon: orange; oxygen: red; nitrogen: blue; and hydrogen: white. The color code for the right simulation box is anion: red, cation: green.

Table 1 Theoretical densities $\rho_{370\,K}$ and box sizes a of the simulation boxes

Quantity	$\rho_{370\,K}$/g cm^{-3}	a/Å
$[ala]^-$	1.086	16.96
$[pro]^-$	1.070	17.66
$[his]^-$	1.064	18.65
$[trp]^-$	1.093	19.70
$[phe]^-$	1.089	18.89
$[tyr]^-$	1.139	19.25

3. Methods

3.1 Static quantum chemical calculations

Quantum chemical calculations were carried out in order to obtain the electrostatic potentials (ESPs) of the amino acid anions. Therefore, geometry optimizations as well as frequency calculations were performed with the Orca[36] software package employing the PBEh-3c[37] composite method, which was paired with a modified def2-SV(P) basis set, termed as def2-mSVP. This method includes the DFT-D3 dispersion correction scheme[38,39], as well as a geometrical counterpoise correction[37,40] in order to account for the intermolecular, as well as the intramolecular, basis set superposition error. The grid level was chosen as 5 and a tight convergence criteria was selected for the SCF energy calculations as well as in geometry optimizations. These simulation boxes were equilibrated at the level of a classical force field employing the Canongia Lopes and Padua force field parameters.

3.2 MD simulations

The LAMMPS software package[41] was used to pre-equilibrate all simulation boxes with the classical force field of Canongia Lopes and Padua (CL & P).[42,43] The *NpT* ensemble was used to obtain equilibrium densities (Table 1) for each IL system with an applied time step of 1 fs, a temperature of 370 K, the barostat applying 1 bar of pressure to the system, and 500 ion pairs.[44,45] These simulations were run for 10 ns. Experimental densities were not found for each IL, but for both $[C_2C_1Im][ala]$ (1.089 g cm^{-3}) and $[C_2C_1Im][pro]$ (1.109 g cm^{-3}) measured at 353.15 K.[46] Deviations of the theoretically derived densities are small, with an error of 2.8% and 3.5%, respectively, compared

to experiment. Based on the cell parameters given in Table 1, simulation boxes containing 16 ion pairs were again set up using PACKMOL.[47,48] To remove initial hotspots, these boxes were equilibrated for 20 ns in the *NVT* ensemble, using a time step of 1 fs as well as the aforementioned force field parameters. The last step of each of these trajectories was taken as the input structure for the subsequent AIMD simulations.

Before performing the production run, these input structures were further equilibrated for 10 ps (20 000 steps) in the *NVT* ensemble using AIMD simulations. Therefore, a temperature of 370 K, a time step of 0.5 fs and Nosé–Hoover massive thermostats with a coupling constant of 10 fs were employed. Then the production simulation was performed in the *NVT* ensemble and both with a timestep of 0.5 fs applied and a temperature of 370 K.[44,45] The production run was performed for 30 ps (60 000 steps) employing a global thermostat and a thermostat coupling constant of 50 fs. The BLYP functional[49,50] was applied in combination with the corresponding BLYP Goedecker–Teter–Hutter pseudopotentials[51–53] for core electrons and the molecularly optimized double-ζ basis set (MOLOPT-DZVP-SR-GTH)[54] was used. Dispersion interactions were accounted for by the DFT-D3 correction.[38,39] The target accuracy for the SCF convergence was set to 10–5 and the density CUTOFF criterion was set to 280 Ry with a relative cutoff of 40 Ry and multigrids number 5 (NGRID 5). AIMD simulations were carried out based on the hybrid Gaussian and plane wave (GPW) method with CP2K.[55] Dipole moments and polarizations are calculated using the Wannier method, different charge schemes (Blöchl/Löwdin/Mulliken) and Voronoi tessellation as implemented in CP2K. TRAVIS (Trajectory Analyzer and Visualizer)[56,57] is used to analyze the trajectories obtained from simulations.

3.3 Methodology

The localized Wannier function is calculated using AIMD simulations and applying a block Jacobi method.[58] In eqn (1), for each molecule I, the dipole moment consists of the sum of all Wannier function centers assigned to each molecule and the sum of nuclei with the charges Z_A at the positions R_A:

$$\mu = -2e\sum_{i=1}^{N} r_i + e\sum_{A=1}^{M} Z_A R_A \quad (1)$$

Here, e is the elementary charge, while r_i refers to the position of the Wannier centers. The N and M show the nuclei number and all nuclei numbers of the molecule. Through assuming that the dipole moment includes the electric field E, a possible calculation scheme for the polarization is shown in eqn (2):

$$\mu_{ind} = \alpha E \quad (2)$$

Here, the α is the second-order polarizability tensor. When considering charge schemes such as Blöchl, Löwdin and Mulliken methods, the molecular dipole moment μ can be obtained through the classical definition:

$$\mu = \sum_{i=1}^{N} q_i \cdot \vec{r_i} \quad (3)$$

where the N shows the number of nuclei. The q_i and $\vec{r_i}$ are charge and position, respectively. In contrast, Voronoi tessellation is an extended segmentation scheme, which allows Voronoi positions at atomic locations to be independent. In radical Voronoi tessellation, van der Waals radii are assigned to the sites which are chosen to be the location of the nuclei. Thus, the Voronoi cell C_i^r is given by

$$C_i^r = \{x \in R^3 | (x - s_i)^2 - r_i^2 \leq (x - s_j)^2 - r_j^2 \forall j \neq i\},\ i, j = 1, ..., n, \quad (4)$$

with s_i being sites and chosen to be the nuclei' position. In this equation, a Voronoi cell contains all points in space which are closer to s_i than to any other site. The molecular cells M_K are obtained by uniting the Voronoi cells of all atoms in the same molecule. The dipole moment distribution can be obtained by integrating the electron density $\rho(r)$ as a function of spatial coordinates r over molecular cells in space:

$$\mu_k = \int_{M_K} r\rho(r)\mathrm{d}r,\ k = 1, ..., N \quad (5)$$

The position of the element surface between two atoms is determined by the square deviation of the radius. For each cell, the charge calculation is defined as eqn (6) and the dipole moment being calculated by eqn (7).

$$q_i = \int_{C_i^r} \rho(r)\mathrm{d}r \quad (6)$$

$$\mu = \int_{C_i^r} r\rho(r)\mathrm{d}r \quad (7)$$

Due to all systems being defined consistently within the same methods, it is possible to compare different ions to identify common trends. Within these analyses, center of charge (COC) is defined as the ion's center and is used to analyze the angular distribution. This means the molecule geometric center is weighted by the charge on the atoms.[24] This is in contrast to the center of mass (COM) which is defined as the center of the molecule by mass. In this study, the dipole moment of $[C_2C_1Im]^+$ is calculated with respect to the geometric center of the five ring atoms (COR) and the anion's dipole moment is calculated from the COM.

4. Analysis and results

4.1 Molecular dipole moments

The intensities of IR and Raman spectra are found to depend on the strength of molecular dipole moments and polarization. The dipole moment is not only a measure of charge displacement, but also an indicator of the local accumulation density of the molecules. It is used to summarize the effects of electrons in space and describe the interactions of charges and assess the

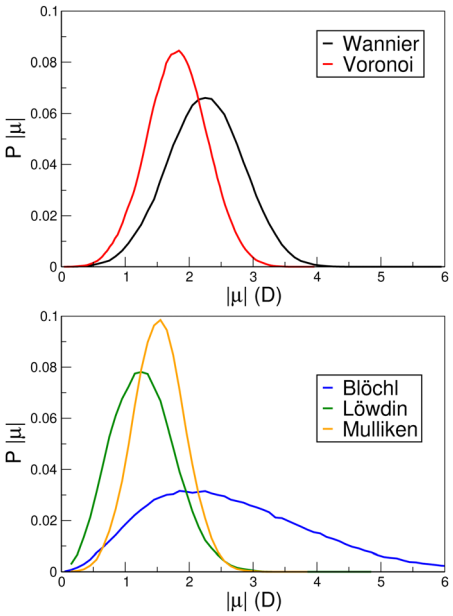

Fig. 2 Dipole moment distributions based on the Wannier center and Voronoi tessellation for the cations of the $[C_2C_1Im][pro]$ (above). Dipole moment distributions based on Blöchl, Löwdin and Mulliken charges for the cations of the $[C_2C_1Im][pro]$ (below).

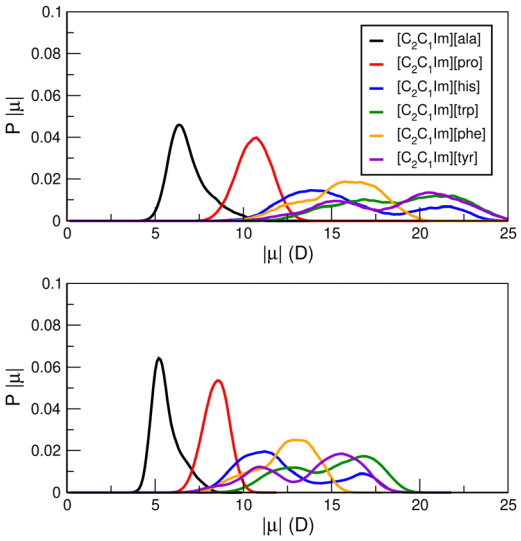

Fig. 3 The dipole moment distributions based on Wannier center (above) and Voronoi (below) analysis for the anions of the ILs.

abundance of sterically favourable configurations. As a result, analysis of the dipole moment accurately shows the variation of the electrostatic properties of ions with local liquid phase changes.

Fig. 2 shows the dipole distributions for cations and anions of $[C_2C_1Im][pro]$ studied using three methods: Wannier functions, Voronoi tessellation as well as Blöchl, Löwdin and Mulliken charge schemes. Compared to non-IL solvents, such as water, ILs are known to typically give a broader dipole moment distribution.[59] In the cation of 1-ethyl-3-methylimidazolium thiocyanate and 1-ethyl-3-methylimidazolium dicyanamide,[33] the dipole moments of the cations show a much higher value than that in the systems presented in this study. As the size of the anion and polarization increase, the range (the difference between the maximum and the minimum values found) of the dipole moment distribution also shows a distinct increase. This is shown particularly in Fig. 3, wherein the $[C_2C_1Im][ala]$ IL has a range of 6.3 D for the $[ala]^-$, whilst $[C_2C_1Im][tyr]$ gives a range of 15.5 D for the $[tyr]^-$ anion when calculated using the Wannier method. This relationship between the size of the IL ions and the range of dipole distribution comes due to the flexibility of the IL ions. This is due to more conformers being thermodynamically possible in large, flexible ion systems, which in turn causes an increase in possible dipole magnitudes. This is in agreement with literature, wherein this relationship is shown specifically in imidazolium ILs.[33] Specifically, these studies have shown that fluctuations in dipoles are primarily determined by the anion rather than the $[C_2C_1Im]^+$ cation. When comparing Fig. 2 and 3, the cations show lower dipoles (2.0 D on average) compared to the anions (all over 4.0 D) studied here when calculated using Wannier and Voronoi methods. When comparing the cation dipole strength in these ILs, the change of anion was found to have a minimal impact on the dipole moment of the cation calculated using the Wannier and Voronoi methods. For cations, the dipole moments distributions have the same mean value in the six systems in both the Wannier and Voronoi methods (2.5 D for Wannier and 2.0 D for Voronoi, see Fig. 2). In the case of the anions, all methods yield the same trends for the dipole strengths, in Fig. 3, the order is in all cases A, B, C and E from the weakest to the strongest dipole. In the case of the ILs collectively, when calculated using the Voronoi method, these are found to have lower dipole moments distributions than those found using the Wannier method, with an average difference of 1.0 D. This relationship comes as a result of the ions having a greater charge when using Wannier centers, while the electron density can flow between Voronoi cells.

In the cases of $[C_2C_1Im][his]$, $[C_2C_1Im][trp]$ and $[C_2C_1Im][tyr]$, the anions show two dipole maxima in the Wannier center method and Voronoi method. Typically, the electric dipole moment of the molecule primarily depends on the charge displacement caused by hydrogen bonds. In Fig. 4, a comparison of the gas phase ESPs of the amino acid anions shows that in the system of $[his]^-$, the presence of the aromatic ring may cause the observed two dipole maxima due to these positions being negatively charged. Similarly, in $[trp]^-$ the π-system can also be used to explain the two dipole maxima due to their negative charges. When comparing the structure $[C_2C_1Im][tyr]$ with $[C_2C_1Im][phe]$ in Fig. 1, one of the H-atoms on the benzene ring of $[C_2C_1Im][tyr]$ is substituted by a hydroxyl group, one conclusion is that the alcohol group alters the dipole distribution to two dipole signals due to the –OH group being negatively charged.

In order to estimate the influence of the charge calculation method, the dipole moment distribution was calculated using Löwdin and Mulliken charge schemes (Fig. 5). When comparing charge calculation methods, there is shown to be significant

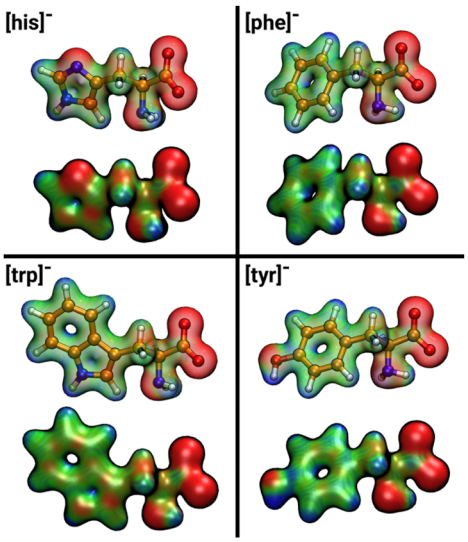

Fig. 4 Gas phase electrostatic potentials of the amino acid anions: $[his]^-$, $[trp]^-$, $[phe]^-$ and $[tyr]^-$, mapped onto the electron density (isosurface value 0.04). The color scale is chosen from −0.1 (blue) to 0.1 (red).

variation between methods. In the Mulliken method, a basis function is used to represent the molecular wave function. The Löwdin method is similar to the Mulliken method but has been shown to produce more localized virtual orbitals.[60,61] Both of the Mulliken and Löwdin methods are based on one-particle density matrices of the molecule, which are defined over standard non-orthogonal basis sets and over symmetrically orthogonalised atomic orbitals, respectively.[60,62,63] In comparison with the Löwdin charge scheme, the Mulliken charge scheme was shown to give dipoles closer (especially the two dipole maxima) to those of the Wannier and Voronoi methods (Fig. 3), so that the Mulliken method will be used in the next part of this study. For example, over all ILs studied, Mulliken dipoles are shown to differ by 1.0 D and under 0.5 D from Wannier and Voronoi, respectively. In the case of dipole values, Blöchl charges were shown to cause a weaker dipole moment by 0.5 D compared to Wannier in the case of $[C_2C_1Im]^+$. Löwdin and Mulliken methods were also shown to cause further reduced dipole moments (1.5 D and 1.0 D for Löwdin and Mulliken respectively on average) compared to Wannier as shown in Fig. 3. Meanwhile, this trend of reduced dipole moments in the Blöchl, Löwdin and Mulliken methods was also noted in the anions of the ILs analyzed.

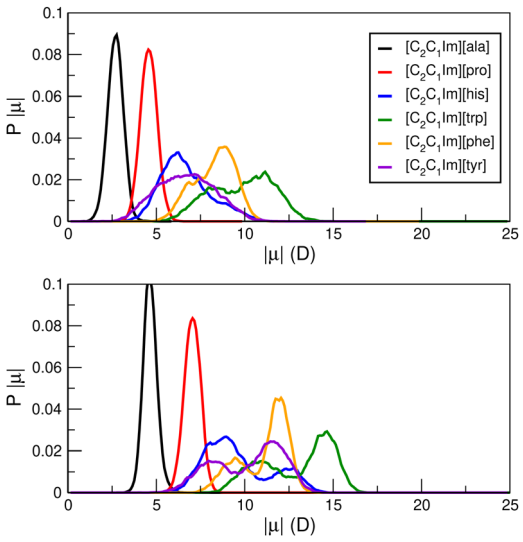

Fig. 5 Dipole moment distributions based on Löwdin (above) and Mulliken (below) charge schemes for the anions of the IL.

In order to obtain the monopole interactions between ions, the Mulliken method is used to measure charge transfer between cations and anions (Table 2). From this data, system D showed the highest degree of charge transfer (0.635 e) which was also found to be the most highly polarized, which highlights the possible correlation between polarization and charge transfer. The charge transfer of other systems were relatively consistent in comparison, varying by less than 0.1 e.

4.2 Locality of charge–dipole and dipole–dipole interactions

In monopole-dipole electrostatic interactions, the angular probability distribution between the dipole of one ion and the vector quantity from the ion center reference of other ions COC can be utilized to measure the degree of locality. The angular distribution is calculated using:

$$\cos\Phi(\text{charge}-\text{dipole}) = \mu_{\text{cat}}^{\text{ref}} \cdot r_{\text{cat}}^{\text{shell}_i} / \left|\mu_{\text{cat}}^{\text{ref}}\right| \cdot \left|r_{\text{cat}}^{\text{shell}_i}\right| \quad (8)$$

and

$$\cos\Phi(\text{dipole}-\text{dipole}) = \mu_{\text{cat}}^{\text{ref}} \cdot \mu_{\text{cat}}^{\text{shell}_i} / \left|\mu_{\text{cat}}^{\text{ref}}\right| \cdot \left|\mu_{\text{cat}}^{\text{shell}_i}\right| \quad (9)$$

Here, $\mu_{\text{cat}}^{\text{ref}}$ is defined as the dipole moment and $r_{\text{cat}}^{\text{shell}}$ is defined as the vector of the COR to the COC of the reference $[C_2C_1Im]^+$ ion. Normally, the dipole moment distribution of cations is closely related to the orientation of the $r_{\text{cat}}^{\text{shell}}$ and the cation dipole.[33] The Mulliken charge scheme was chosen due to its well established ability to replicate charges from Wannier and Voronoi approaches as discussed above. The angular probability distribution of $\cos\Phi$ (charge–dipole) and $\cos\phi$ (dipole–dipole) of cations or anions separated by distance is shown in Fig. 6 and 7. As a result of the structure of $[C_2C_1Im][trp]$ containing more negative points shown in the analysis of electrostatic potentials, especially on the rings, the location of the COC contained a large degree of uncertainty. In all systems, when the distance was found to be over 700 pm, there was no preferential alignment, as shown in Fig. S1–S4 (ESI†). In particular in systems $[C_2C_1Im][pro]$, $[C_2C_1Im][his]$ and $[C_2C_1Im][phe]$ the cut-off for preferential alignment is as low as 500 pm, while the correlations of the dipoles and the COC directions decay more slowly. In previous studies, the anion

Table 2 Charge transfer in the units of *e* obtained *via* Mulliken analysis for each IL tested as labelled in Fig. 1

A	B	C	D	E	F
0.306	0.270	0.253	0.635	0.264	0.230

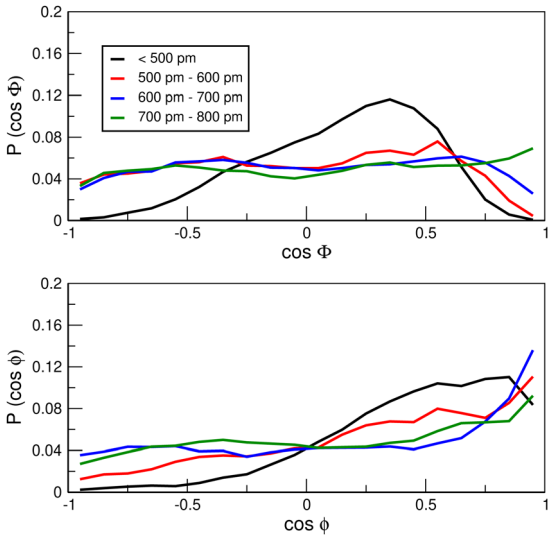

Fig. 6 Angular probability distribution of cos Φ (charge–dipole) and cos ϕ (dipole–dipole) separated by distance below 500 pm (black), from 500–600 pm (red), from 600–700 pm (blue) and 700–800 pm (green) for cations in $[C_2C_1Im][his]$.

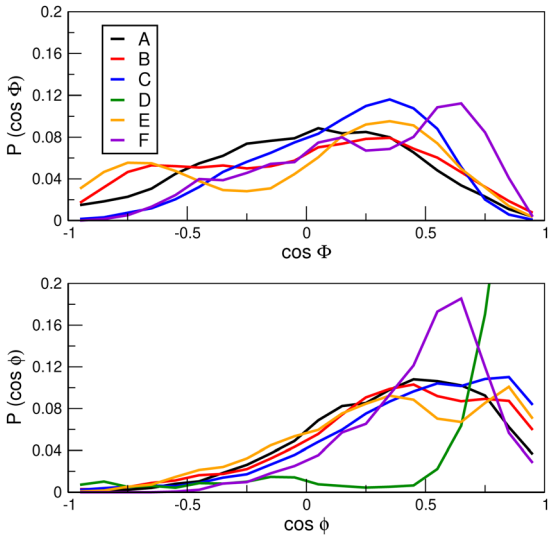

Fig. 7 Angular probability distribution of cos Φ (charge–dipole) and cos ϕ (dipole–dipole) of cations separated by distances below 500 pm of all ILs analyzed.

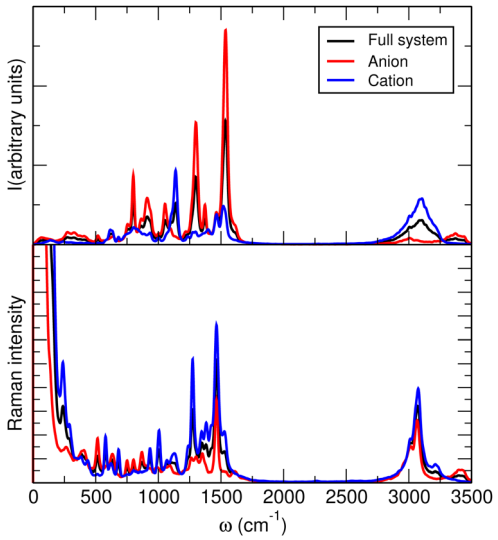

Fig. 8 IR (top) and Raman (bottom) spectra of $[C_2C_1Im][ala]$ calculated using Voronoi tesselation.

was found to exert a strong influence over the preferential alignment and r_{cat}^{shell} directionality.[64] In a previous paper,[33] it was proposed that charge locality and fluctuation of imidazolium-based ILs may be general features in many varied IL systems. As has been shown through the data presented in this study, we further prove the link between locality and charge fluctuation with further classes of ILs.

Prior studies have shown that IR and Raman intensities are influenced by the molecule polarizability and dipole moment, respectively.[65,66] As such, the accuracy of using Voronoi tessellation to predict dipole moments and polarization in amino acid ILs can be validated through comparing the predicted IR and Raman spectra with experiment.[67] Fig. 8 shows the IR and Raman spectra of $[C_2C_1Im][ala]$ obtained theoretically from Voronoi tessellation. Herein, both IR and Raman spectroscopy agree with peak relative intensities and shapes of main peaks (around 1500 cm^{-1} and 3000 cm^{-1}). Among these, the peak at 1500 cm^{-1} corresponds to the double bonds stretching vibration in $[C_2C_1Im][ala]$, whilst the broad peak above 3000 cm^{-1} is indicative of an unsaturated hydrocarbon C–H stretching band.

The main peaks in the IR spectra were compared to experimental data as shown in Table 3. In the IR measured experimentally and shown in Fig. S1 in the ESI,† there is shown to be good correspondence to the theoretical data. For example, the peak seen experimentally at 1561 cm^{-1} is also shown theoretically around this point, which corresponds to the C═O stretch. The peak at over 3000 cm^{-1} corresponding to the unsaturated hydrocarbon C–H stretching vibration is also accurately predicted being at 3083 cm^{-1} experimentally and 3104 cm^{-1} theoretically. When comparing the Raman experimental data for neutral alanine published in literature,[67] shows strong consistency, exhibited by the peak at 1450 cm^{-1} being reproduced, which relates to the $C_{Et}H$ bending vibration. In addition, in theoretical calculations it is possible to separate the IR and Raman spectra of individual ions. This allows for the possibility to assign individual signals either to the cation or anion, something not possible in experimental studies. For instance, the signal around 1600 cm^{-1} in IR is strongest in the anion due to it being from the C═O antisymmetric stretch in the anion. While in contrast, the signal around 1100 cm^{-1} in IR is strongest in the cation and is attributed to the in-plane $C_{Im}H$ bending. This therefore outlines the possibility of accurately predicting the IR and Raman spectra using MD on these complex amino acid IL systems. This method is able to account for the influence of effects on molecular polarizability and

Table 3 Notable vibrational wavenumbers in the IR spectra of $[C_2C_1Im][ala]$. Comparison of experimental wavenumbers ω_{exp}/cm^{-1} and theoretical wavenumbers ω_{the}/cm^{-1}

ω_{exp}/cm^{-1}	ω_{the}/cm^{-1}	Description
1169	1138	$C_{Im}H$ bend
1357	1305	$C_{ala}H_3$ bend
1561	1537	C_{ala}=O stretch
2111		Water
2597		Water
3083	3104	=$C_{Im}H$ stretch

dipole moments observed, while also being able to separate the anion and cation signals.

5. Conclusion

In this study, we focused on examining the fluctuation and locality of dipole moment in six amino-acid based imidazolium ILs utilizing AIMD simulations. The results indicated that for ILs, both the type of ions used and the methods of calculations affects the magnitude of the dipole moment and polarization. In particular, between different charge function calculation method, the Mulliken charge scheme showed greater consistency with Wannier centers and Voronoi tessellation in comparison to Blöchl and Löwdin charge schemes. There was also found to be a link between anion size and range of dipole moment distribution, with larger amino acid anions shown to give broader dipole moment distributions. In addition, Raman/IR were accurately reproduced for $[C_2C_1Im][ala]$ system and were able to effectively differentiate the source of each signal between ions. This study therefore furthers the knowledge of polarization and its affect on spectroscopy in IL solvents. In the future, this may have applications in interface research using AIMD analysis to gain further understanding of interface properties in similar complex IL systems.

Author contributions

Wenbo Dong: methodology, formal analysis, writing – original draft, visualisation, Vahideh Alizadeh: writing – review & editing, Jan Blasius: writing – review & editing, supervision, Luke Wylie: writing – review & editing, Leonard Dick: COC software support, Zhijie Fan: IR experimantal data support, Barbara Kirchner: conceptualisation, writing – review & editing, supervision. All authors have read and agreed to the published version of the manuscript.

Conflicts of interest

There are no conflicts to declare.

Acknowledgements

The authors thank the DFG under the grant project number 406232243, the China Scholarship Council (CSC).

Notes and references

1 B. Kirchner, O. Hollóczki, J. N. Canongia Lopes and A. A. Pádua, *Wiley Interdiscip. Rev. Comput. Mol. Sci.*, 2015, **5**, 202–214.
2 O. Hollóczki, F. Malberg, T. Welton and B. Kirchner, *Phys. Chem. Chem. Phys.*, 2014, **16**, 16880–16890.
3 F. Malberg, O. Hollóczki, M. Thomas and B. Kirchner, *Struct. Chem.*, 2015, **26**, 1343–1349.
4 B. Kirchner, F. Malberg, D. S. Firaha and O. Hollóczki, *J. Condens. Matter Phys.*, 2015, **27**, 463002.
5 S. Zhang, *Encyclopedia of Ionic Liquids*, Springer Nature, 2023.
6 K. Fumino and R. Ludwig, *J. Mol. Liq.*, 2014, **192**, 94–102.
7 A. Mehrkesh and A. T. Karunanithi, *Fluid Ph. Equilibria*, 2016, **427**, 498–503.
8 J. Han, A. Mariani, S. Passerini and A. Varzi, *Energy Environ. Sci.*, 2023, **16**, 1480–1501.
9 M. J. Earle and K. R. Seddon, *Pure Appl. Chem.*, 2000, **72**, 1391–1398.
10 J. Leys, M. Wübbenhorst, C. Preethy Menon, R. Rajesh, J. Thoen, C. Glorieux, P. Nockemann, B. Thijs, K. Binnemans and S. Longuemart, *J. Chem. Phys.*, 2008, **128**, 064509.
11 M. Kanakubo, K. R. Harris, N. Tsuchihashi, K. Ibuki and M. Ueno, *Fluid Ph. Equilibria*, 2007, **261**, 414–420.
12 F. Yebra, J. Troncoso and L. Roman, *Fluid Ph. Equilibria*, 2020, **515**, 112573.
13 A. Jarosik, S. R. Krajewski, A. Lewandowski and P. Radzimski, *J. Mol. Liq.*, 2006, **123**, 43–50.
14 K. Fukumoto, M. Yoshizawa and H. Ohno, *J. Am. Chem. Soc.*, 2005, **127**, 2398–2399.
15 R. D. Rogers and K. R. Seddon, *Science*, 2003, **302**, 792–793.
16 J. Dupont, R. F. de Souza and P. A. Suarez, *Chem. Rev.*, 2002, **102**, 3667–3692.
17 E. D. Bates, R. D. Mayton, I. Ntai and J. H. Davis, *J. Am. Chem. Soc.*, 2002, **124**, 926–927.
18 M. Armand, F. Endres, D. R. MacFarlane, H. Ohno and B. Scrosati, *Na. Mater.*, 2011, **8**, 129–137.
19 C. F. Poole and S. K. Poole, *J. Chromatogr. A*, 2010, **1217**, 2268–2286.
20 Z. Ma, J. Yu and S. Dai, *Adv. Mater.*, 2010, **22**, 261–285.
21 S. Gehrke and B. Kirchner, *J. Chem. Eng. Data*, 2019, **65**, 1146–1158.
22 M. A. Ortuno, O. Holloczki, B. Kirchner and N. Lopez, *J. Phys. Chem. Lett.*, 2019, **10**, 513–517.
23 J. Blasius, R. Elfgen, O. Hollóczki and B. Kirchner, *Phys. Chem. Chem. Phys.*, 2020, **22**, 10726–10737.
24 R. Clark, M. von Domaros, A. J. McIntosh, A. Luzar, B. Kirchner and T. Welton, *J. Phys. Chem.*, 2019, **151**, 164503.
25 B. L. Bhargava and S. Balasubramanian, *J. Am. Chem. Soc.*, 2006, **128**, 10073–10078.
26 F. Biscay, A. Ghoufi, V. Lachet and P. Malfreyt, *J. Phys. Chem. C*, 2011, **115**, 8670–8683.
27 Y. Nagata, T. Ohto, M. Bonn and T. D. Kühne, *Chem. Phys.*, 2016, **144**, 204705.

28 R. Lynden-Bell, *Mol. Phys.*, 2003, **101**, 2625–2633.
29 M. Lsal, *Chem. Phys.*, 2013, **139**, 214701.
30 M. Campetella, M. Montagna, L. Gontrani, E. Scarpellini and E. Bodo, *Phys. Chem. Chem. Phys.*, 2017, **19**, 11869–11880.
31 X. Paredes, J. Fernandez, A. A. Padua, P. Malfreyt, F. Malberg, B. Kirchner and A. S. Pensado, *J. Phys. Chem. B*, 2012, **116**, 14159–14170.
32 K. Wendler, F. Dommert, Y. Y. Zhao, R. Berger, C. Holm and L. Delle Site, *Faraday Discuss.*, 2012, **154**, 111–132.
33 K. Wendler, S. Zahn, F. Dommert, R. Berger, C. Holm, B. Kirchner and L. Delle Site, *J. Chem. Theory Comput.*, 2011, **7**, 3040–3044.
34 C. A. Cassity, B. Siu, M. Soltani, J. L. McGeehee, K. J. Strickland, M. Vo, E. A. Salter, A. C. Stenson, A. Wierzbicki, K. N. West, B. D. Rabideau and J. H. Davis Jr, *Phys. Chem. Chem. Phys.*, 2017, **19**, 31560–31571.
35 X. Meng, J. Wang, H. Jiang, X. Shi and Y. Hu, *Energ Fuel*, 2017, **31**, 2996–3001.
36 F. Neese, *WIREs Comp. Mol. Sci.*, 2012, **2**, 73–78.
37 S. Grimme, J. G. Brandenburg, C. Bannwarth and A. Hansen, *J. Chem. Phys.*, 2015, **143**, 054107.
38 S. Grimme, J. Antony, S. Ehrlich and H. Krieg, *J. Chem. Phys.*, 2010, **132**, 154104.
39 S. Grimme, S. Ehrlich and L. Goerigk, *J. Comput. Chem.*, 2011, **32**, 1456–1465.
40 H. Kruse and S. Grimme, *J. Chem. Phys.*, 2012, **136**, 04B613.
41 S. Plimpton, *J. Comput. Phys.*, 1995, **117**, 1–19.
42 J. N. Canongia Lopes, J. Deschamps and A. A. Pádua, *J. Phys. Chem. B*, 2004, **108**, 2038–2047.
43 J. N. Canongia Lopes and A. Pádua, *J. Phys. Chem. B*, 2006, **110**, 19586–19592.
44 S. Nosé, *J. Chem. Phys.*, 1984, **81**, 511–519.
45 W. G. Hoover, *Phys. Rev. A*, 1985, **31**, 1695.
46 A. S. L. Gouveia, L. C. Tomé and I. M. Marrucho, *J. Chem. Eng. Data*, 2016, **61**, 83–93.
47 J. M. Martnez and L. Martnez, *J. Comput. Chem.*, 2003, **24**, 819–825.
48 L. Martnez, R. Andrade, E. G. Birgin and J. M. Martnez, *J. Comput. Chem.*, 2009, **30**, 2157–2164.
49 J. P. Perdew, *Phys. Rev. B: Condens. Matter Mater. Phys.*, 1986, **33**, 8822.
50 A. D. Becke, *Phys. Rev. A*, 1988, **38**, 3098.
51 S. Goedecker, M. Teter and J. Hutter, *Phys. Rev. B: Condens. Matter Mater. Phys.*, 1996, **54**, 1703.
52 C. Hartwigsen, S. Gœdecker and J. Hutter, *Phys. Rev. B: Condens. Matter Mater. Phys.*, 1998, **58**, 3641.
53 M. Krack, *Theor. Chem. Acc.*, 2005, **114**, 145–152.
54 J. VandeVondele and J. Hutter, *J. Chem. Phys.*, 2007, **127**, 114105.
55 A. CP2k, CP2k developers group under the terms of the GNU General Public License.
56 M. Brehm and B. Kirchner, *J. Chem. Inf. Model.*, 2011, **51**, 2007–2023.
57 M. Brehm, M. Thomas, S. Gehrke and B. Kirchner, *J. Chem. Phys.*, 2020, **152**, 164105.
58 B. Kirchner and J. Hutter, *J. Chem. Phys.*, 2004, **121**, 5133–5142.
59 P. L. Silvestrelli and M. Parrinello, *Phys. Rev. Lett.*, 1999, **82**, 3308–3311.
60 P.-O. Löwdin, *Chem. Phys.*, 1950, **18**, 365–375.
61 I.-M. Høyvik, B. Jansik and P. Jørgensen, *J. Comput. Chem.*, 2013, **34**, 1456–1462.
62 R. Mulliken, *J. Chem. Phys.*, 1955, **23**, 1833.
63 T. Kar and A. Sannigrahi, *J. Mol. Struct.*, 1988, **165**, 47–54.
64 C. Krekeler, F. Dommert, J. Schmidt, Y. Zhao, C. Holm, R. Berger and L. Delle Site, *Phys. Chem. Chem. Phys.*, 2010, **12**, 1817–1821.
65 H. Liu, Y. Wang and J. M. Bowman, *Chem. Phys.*, 2015, **142**, 194502.
66 D. Tuschel, *Spectrosc.*, 2014, **29**, 14–21.
67 G. Zhu, X. Zhu, Q. Fan and X. Wan, *Spectrochim Acta A Mol Biomol Spectrosc.*, 2011, **78**, 1187–1195.

SUPPORTING INFORMATION

Locality in amino-acid based imidazolium ionic liquids

Wenbo Dong,[a] Vahideh Alizadeh,[a] Jan Blasius[a], Luke Wylie[a], Leonard Dick[a], Zhijie Fan[b], Barbara Kirchner[a*]

[a]Mulliken Center for Theoretical Chemistry, University of Bonn, Beringstr. 4+6, D-53115 Bonn, Germany

[b]Department of Chemistry, Imperial College London, South Kensington Campus, London SW7 2AZ, United Kingdom

*email:kirchner@thch.uni-bonn.de

Experimental Methodology

Material and Purification

Unless stated otherwise all materials were used as received without further purification. L-alanine (≥ 99.5%), L-phenylalanine (≥ 99.5%), L-proline (≥ 99.5%), L-histidine (≥ 99.5%), L-tyrosine (≥ 99.5%), L-tryptophan (≥ 99.5%), acetic acid (≥ 99.8%), silver nitrate (≥ 99%), 1-methyl imidazole (≥ 99%), bromoethane (≥ 98%) were purchased from Sigma-Aldrich. Amberlite IRN-78, OH^- form, ion-exchange resin (particle size = 25-30 mesh, 500-600 mm) was purchased from Acros Organics. Starting materials which have been stored over a long time need to purify before use. 1-ethyl imidazole (≥ 99.9%), which was purchased from Fluorochem, and 1-methyl imidazole were stirred over potassium hydroxide overnight, followed by distillation under vacuum. Bromoethane was extracted with concentrated sulfuric acid until the acid layer remained colourless. Then the organic layer was separated and neutralised with saturated sodium bicarbonate aqueous solution, followed by washing with deionised water. The resulting organic layer was dried with anhydrous magnesium sulphate overnight, followed by distillation under vacuum. Upon purification, all reagents were stored in the nitrogen atmosphere prior to reaction.

Equipment

Infrared (IR) spectra were recorded on a Perkin Elmer 1600 series FT-IR spectrometer.

Method

The ILs were synthesized by anion-exchange method.

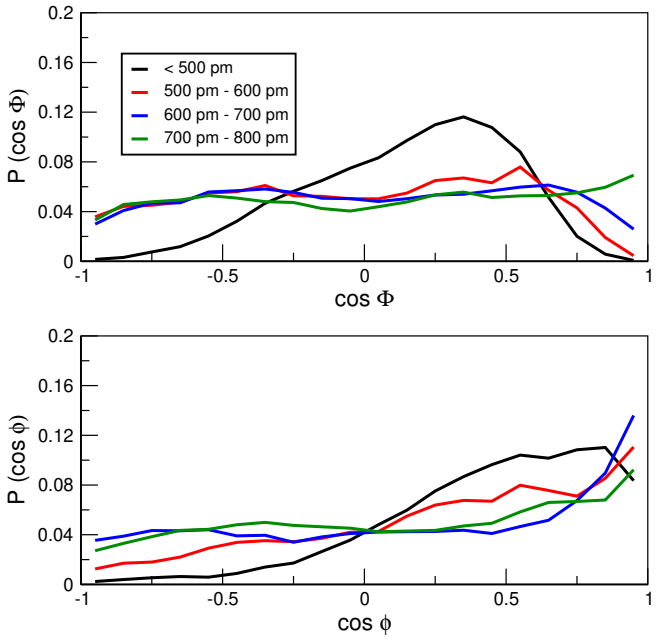

Figure S1: Angular probability distribution of cos Φ (charge-dipole) and cos ϕ (dipole-dipole) separated by distance below 500 pm (black), from 500-600 pm (red), from 600-700 pm (blue) and 700-800 pm (green) for cations in $[C_2C_1Im][his]$.

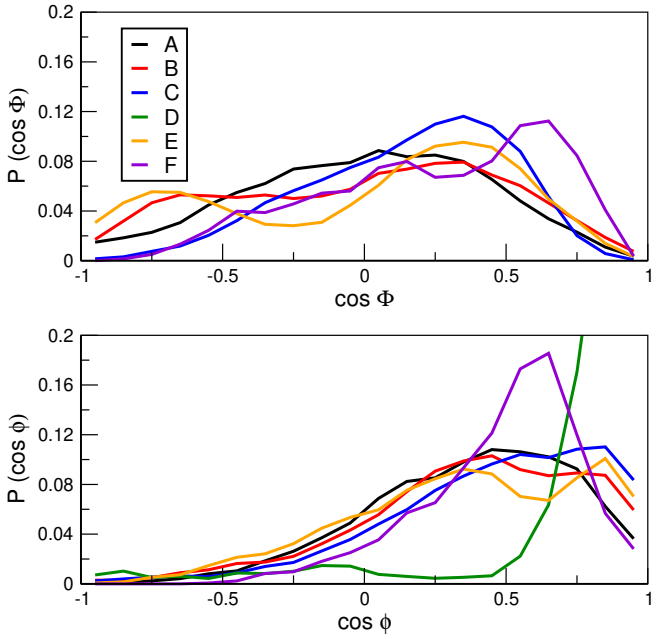

Figure S2: Angular probability distribution of cos Φ (charge-dipole) and cos ϕ (dipole-dipole) of cations separated by distances below 500 pm of all ILs analyzed.

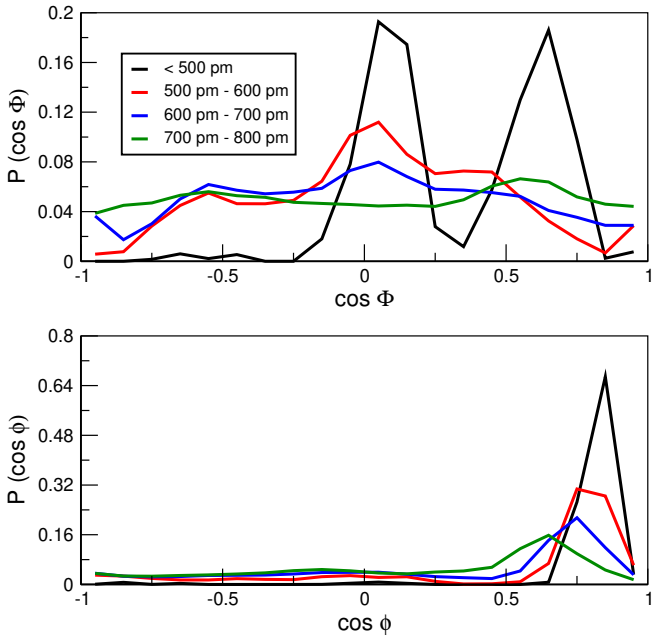

Figure S3: Angular probability distribution of cos Φ (charge-dipole) and cos ϕ (dipole-dipole) separated by distance below 500 pm (black), from 500-600 pm (red), from 600-700 pm (blue) and 700-800 pm (green) for anions in $[C_2C_1Im][his]$.

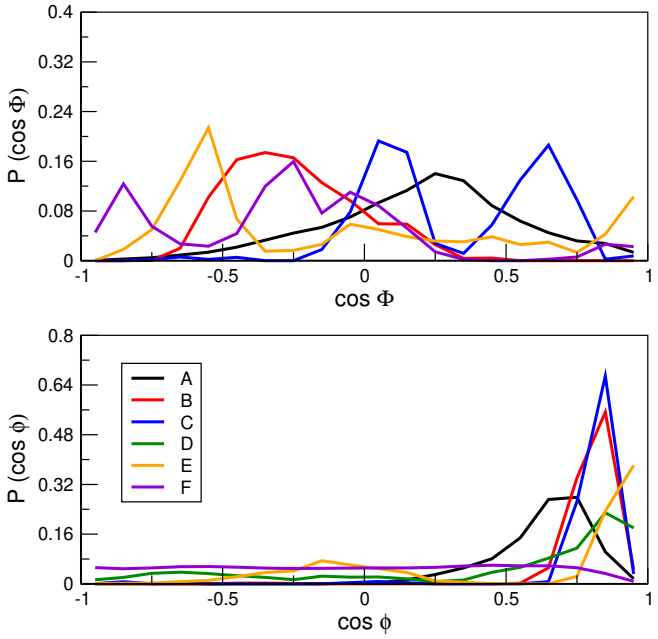

Figure S4: Angular probability distribution of cos Φ (charge-dipole) and cos ϕ (dipole-dipole) of anions separated by distances below 500 pm of all ILs analyzed.

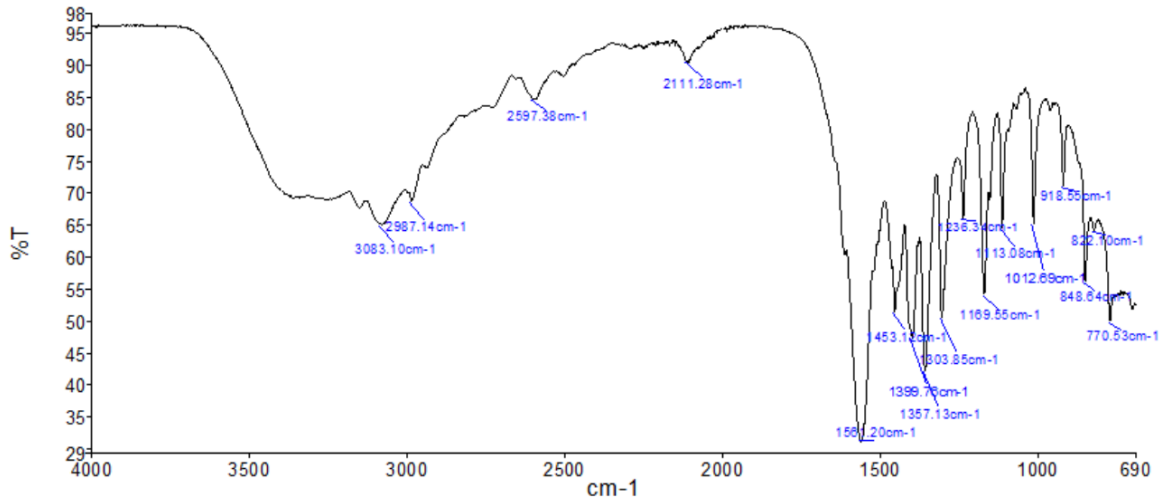

Figure S5: The experimental IR spectrum of $[C_2C_1Im][ala]$.

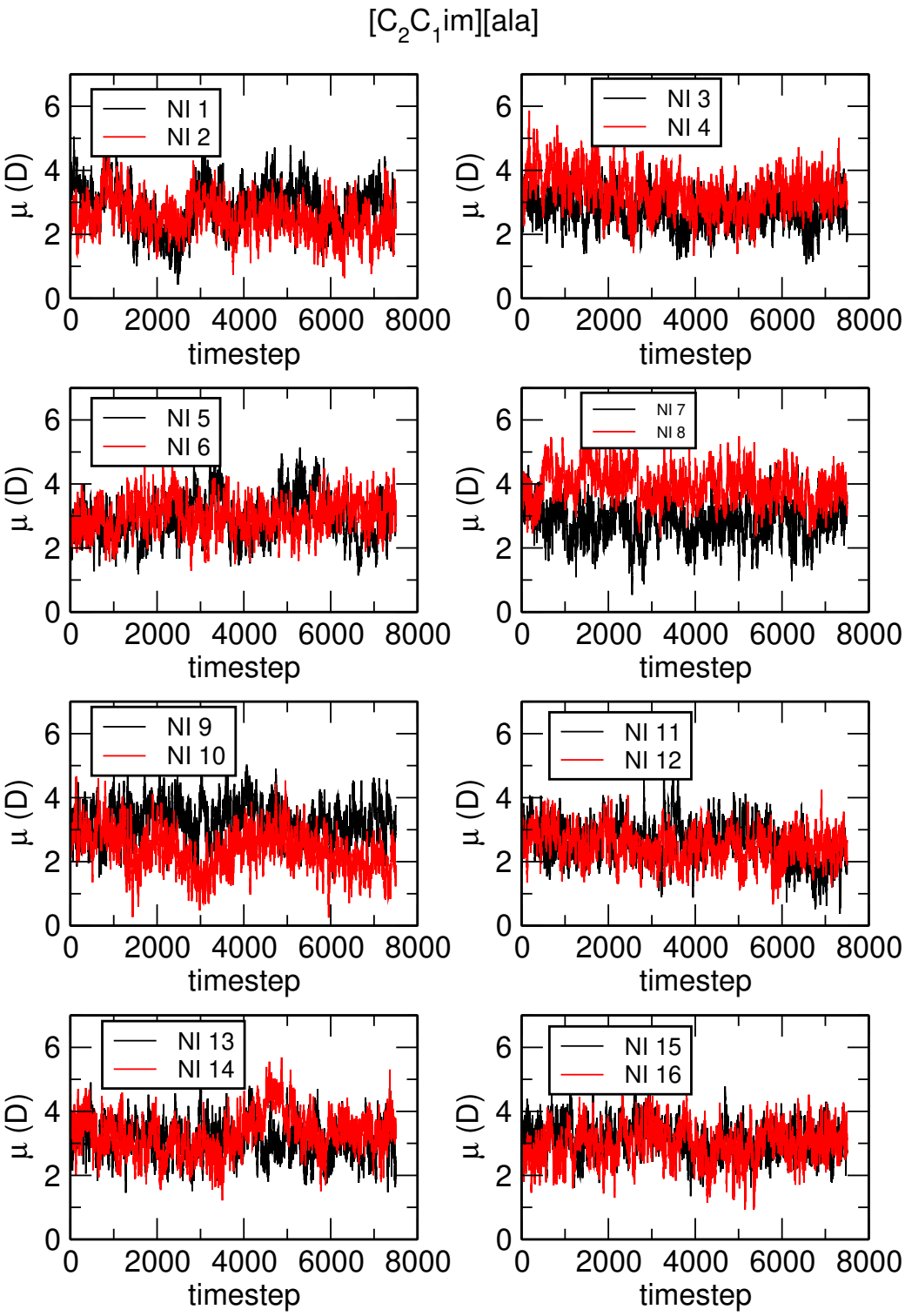

Figure S6: The every time development of the dipole moment (μ) of one randomly selected ion of anion in $[C_2C_1Im][ala]$.

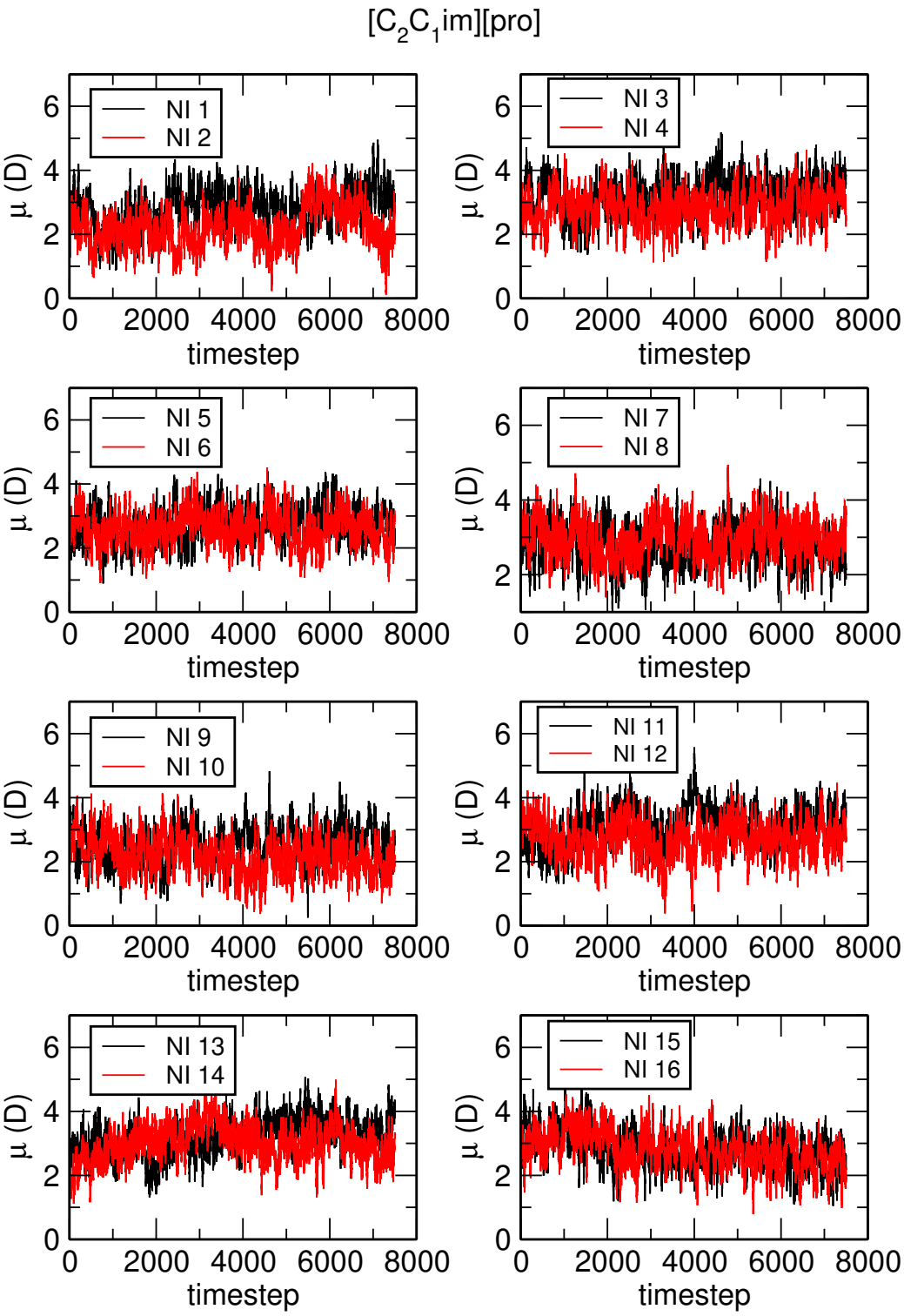

Figure S7: The every time development of the dipole moment (μ) of one randomly selected ion of cation in $[C_2C_1Im][pro]$.

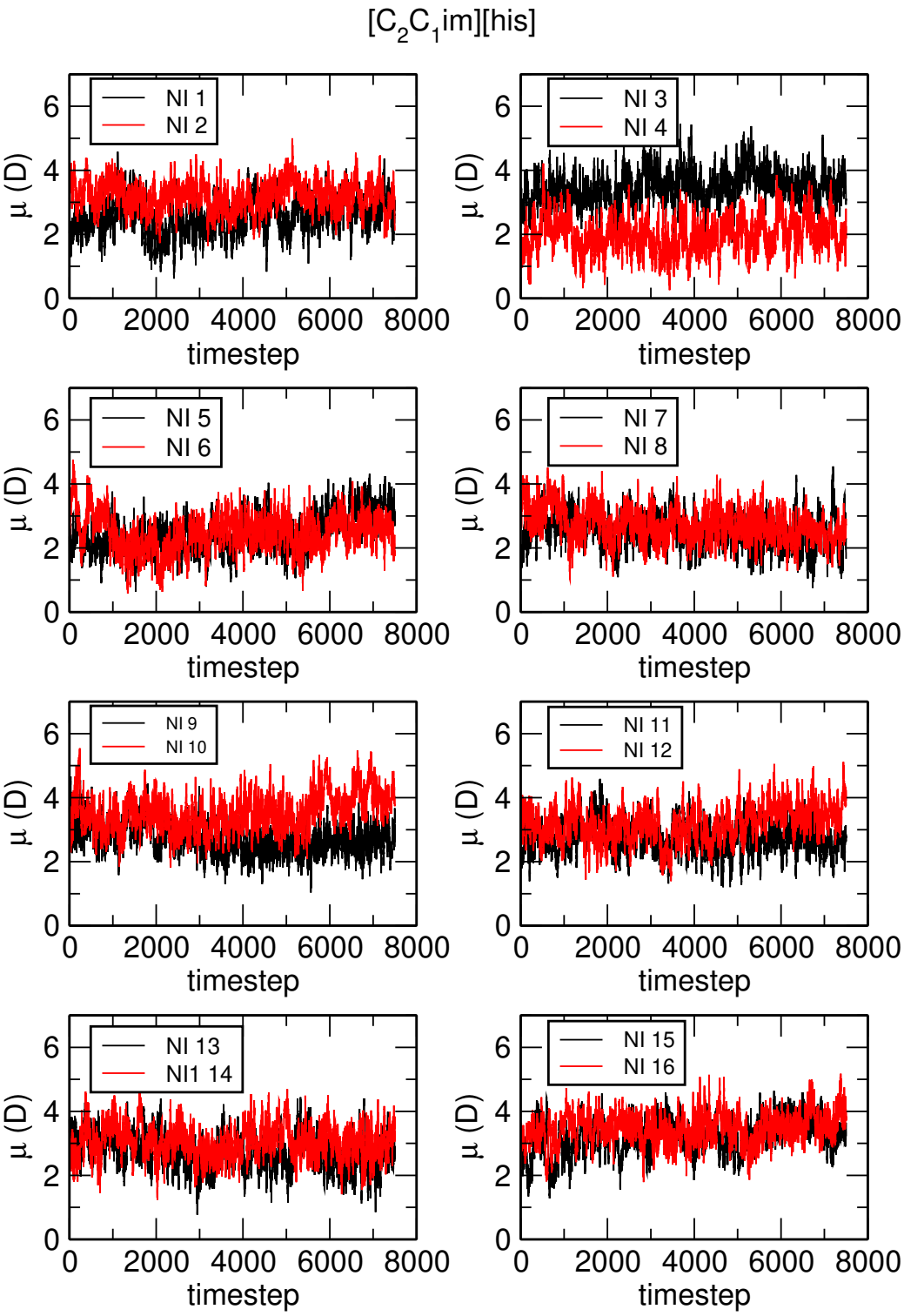

Figure S8: The every time development of the dipole moment (μ) of one randomly selected ion of cation in $[C_2C_1Im][his]$.

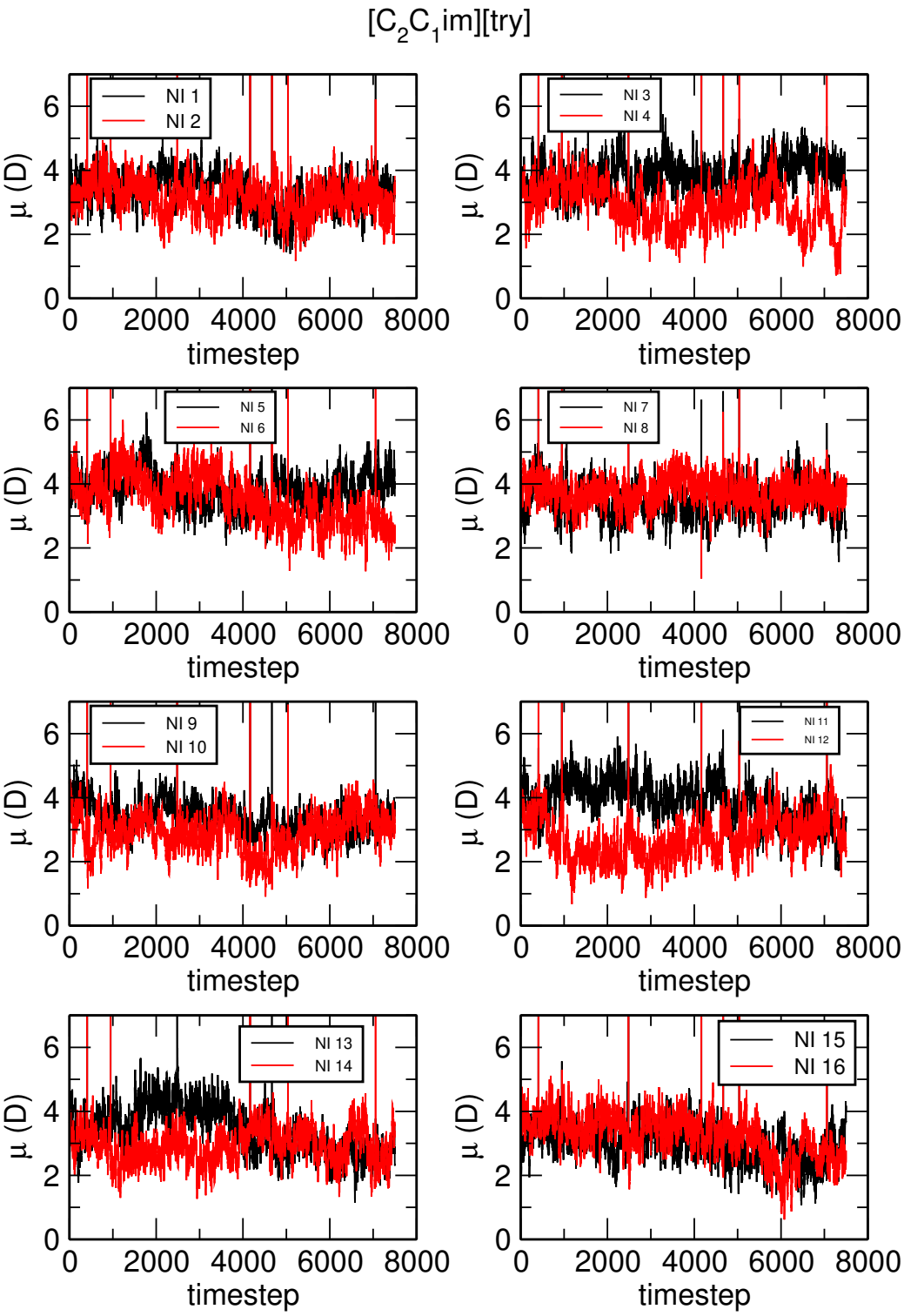

Figure S9: The every time development of the dipole moment (μ) of one randomly selected ion of cation in $[C_2C_1Im][trp]$.

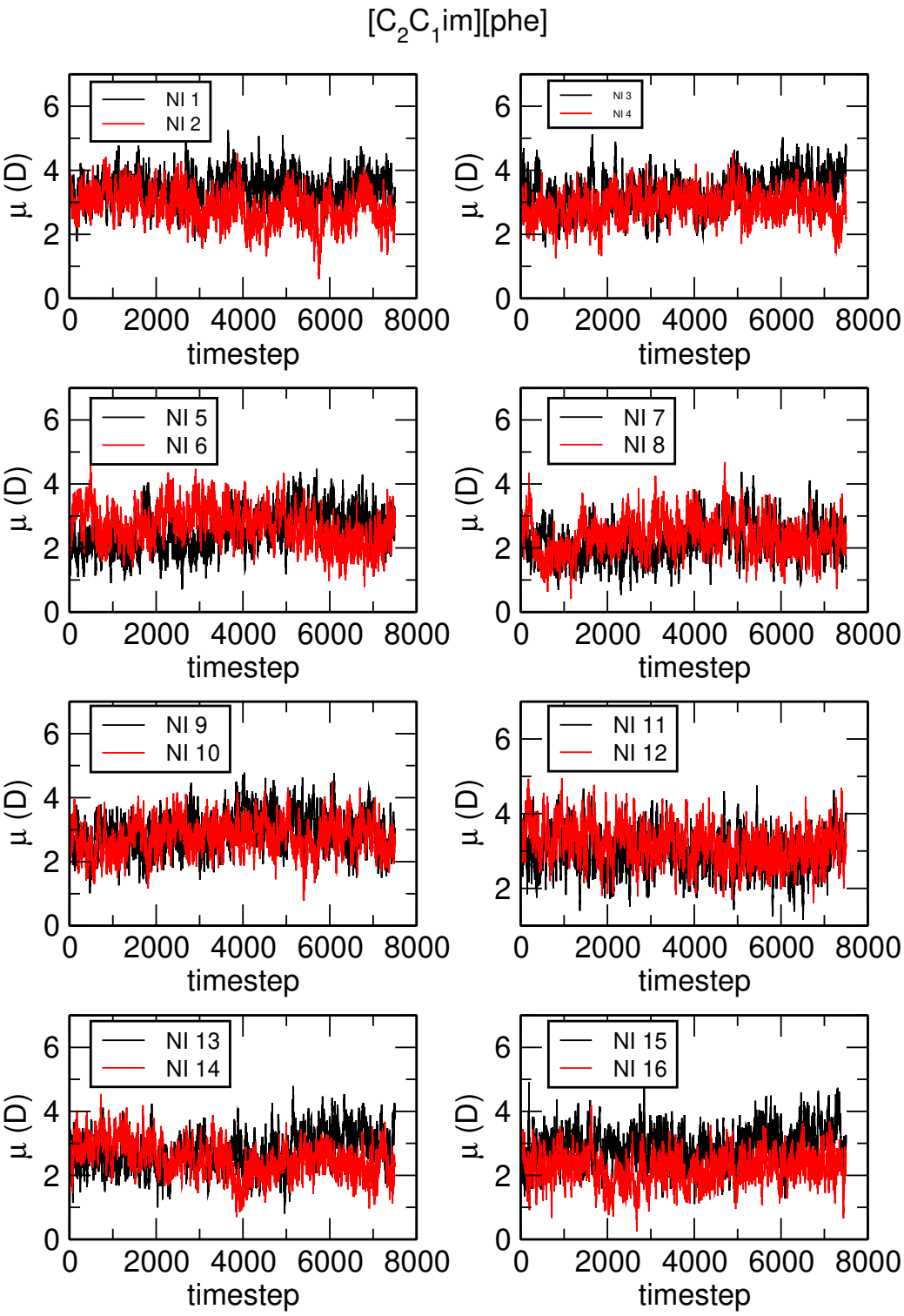

Figure S10: The every time development of the dipole moment (μ) of one randomly selected ion of cation in $[C_2C_1Im][phe]$.

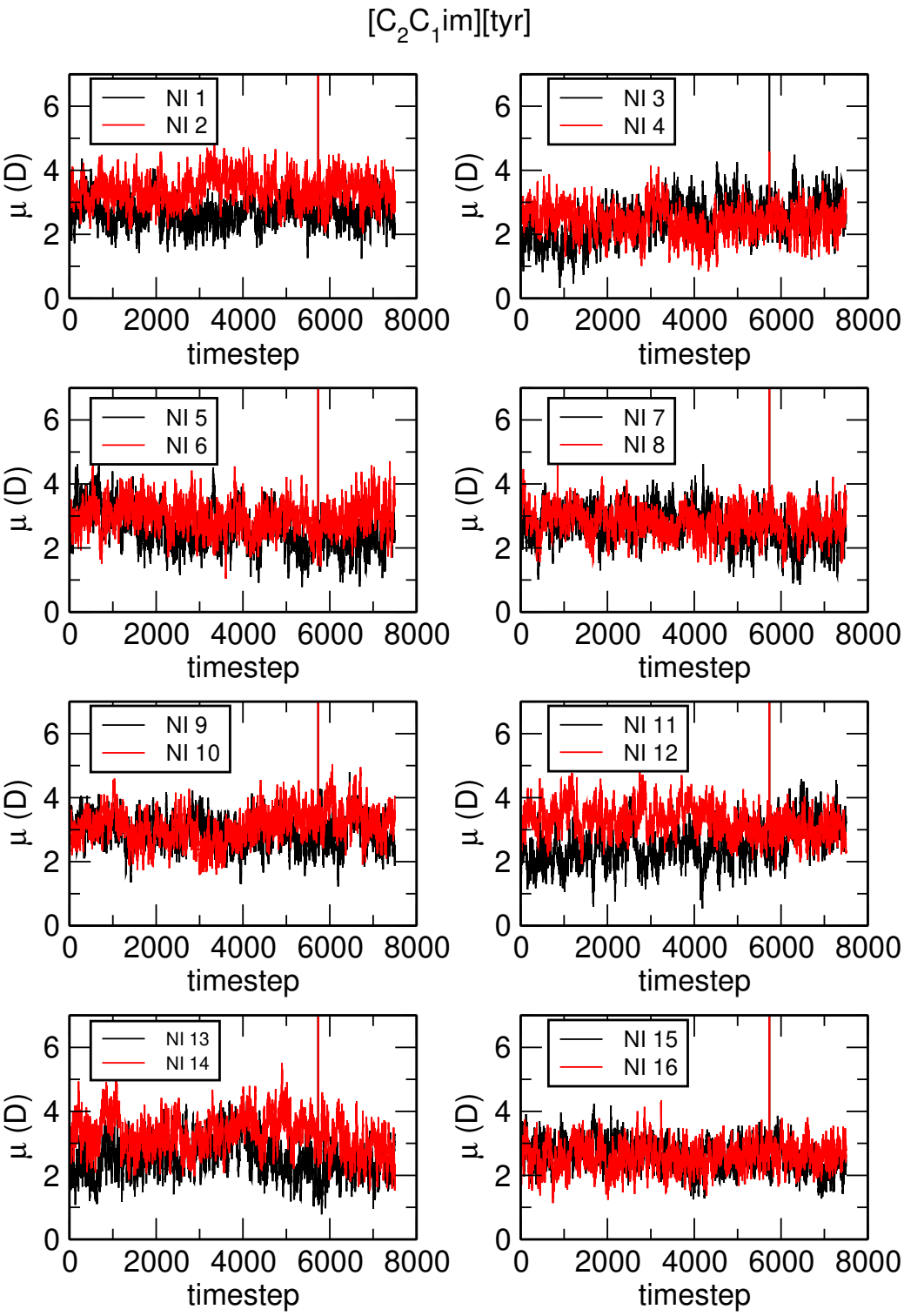

Figure S11: The every time development of the dipole moment (μ) of one randomly selected ion of cation in $[C_2C_1Im][tyr]$.

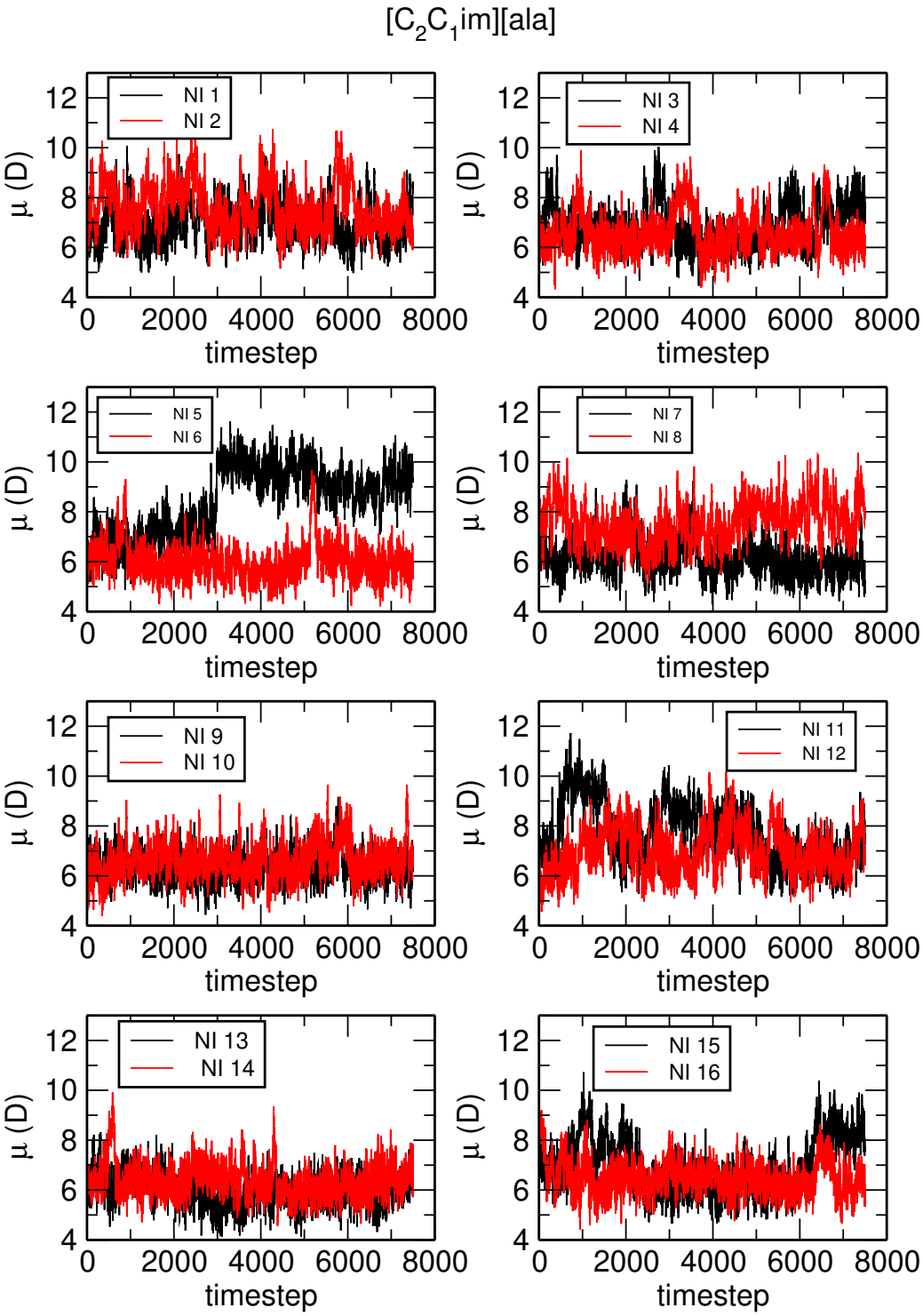

Figure S12: The every time development of the dipole moment (μ) of one randomly selected ion of anion in $[C_2C_1Im][ala]$.

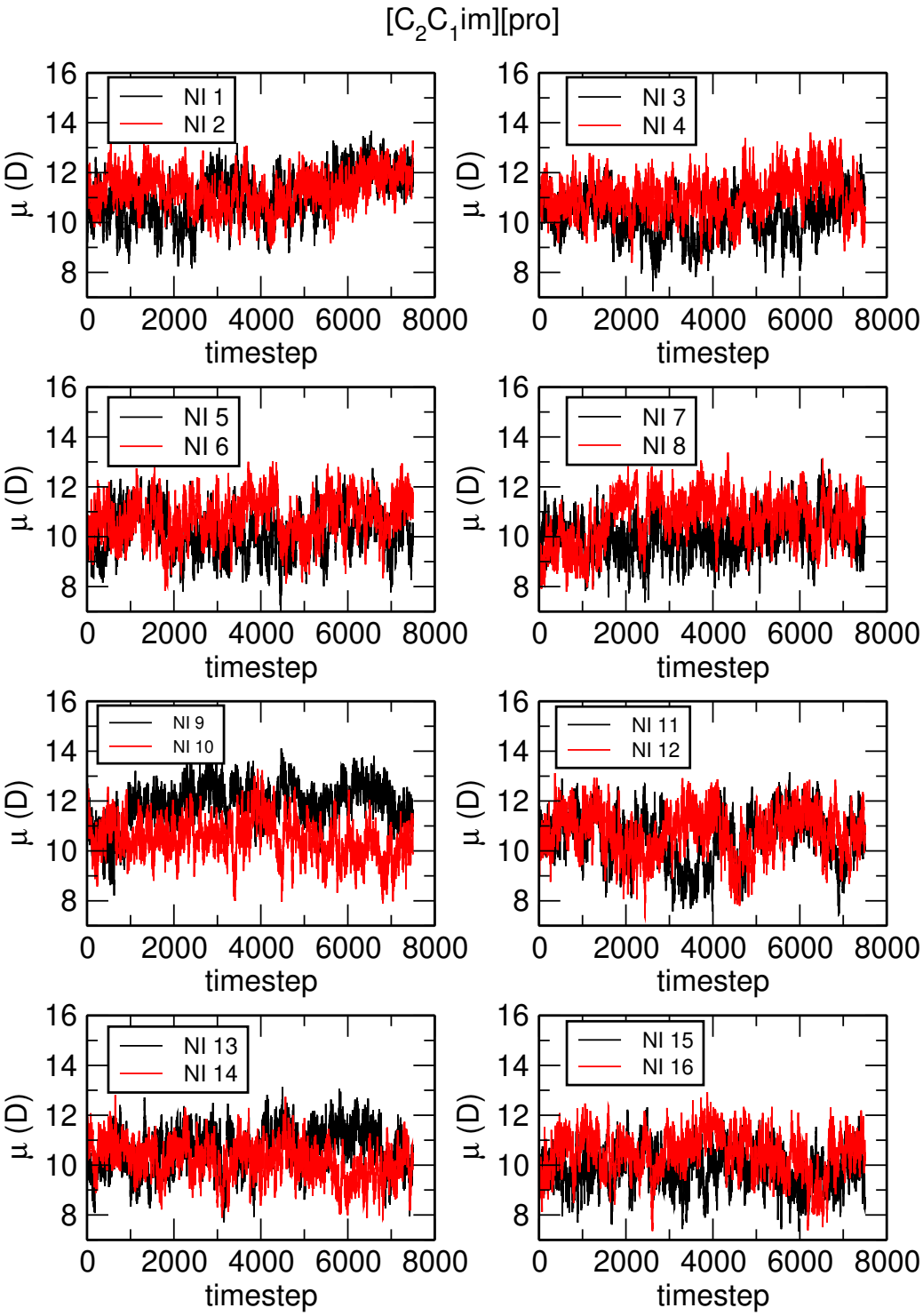

Figure S13: The every time development of the dipole moment (μ) of one randomly selected ion of anion in $[C_2C_1Im][pro]$.

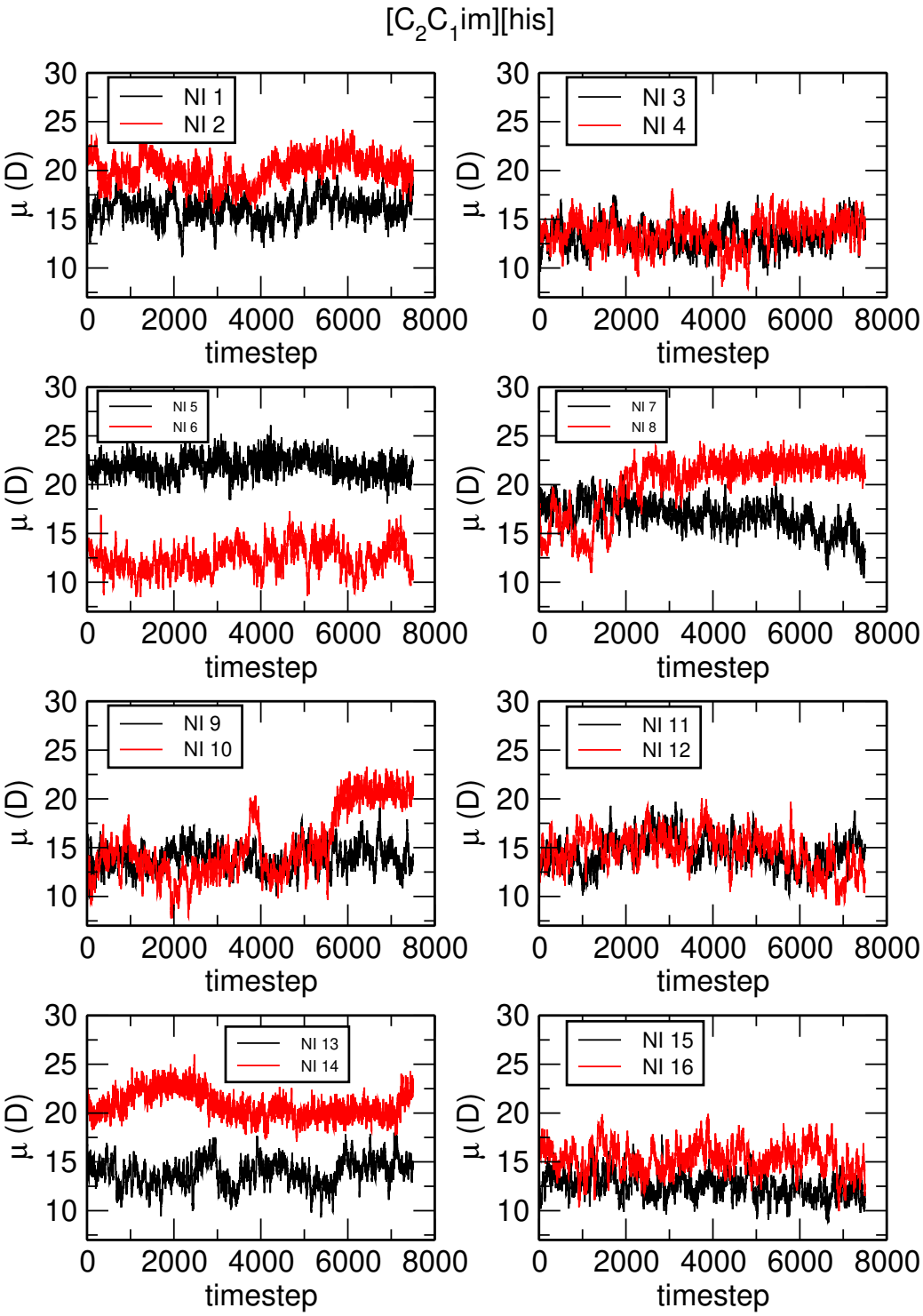

Figure S14: The every time development of the dipole moment (μ) of one randomly selected ion of anion in [C_2C_1Im][his].

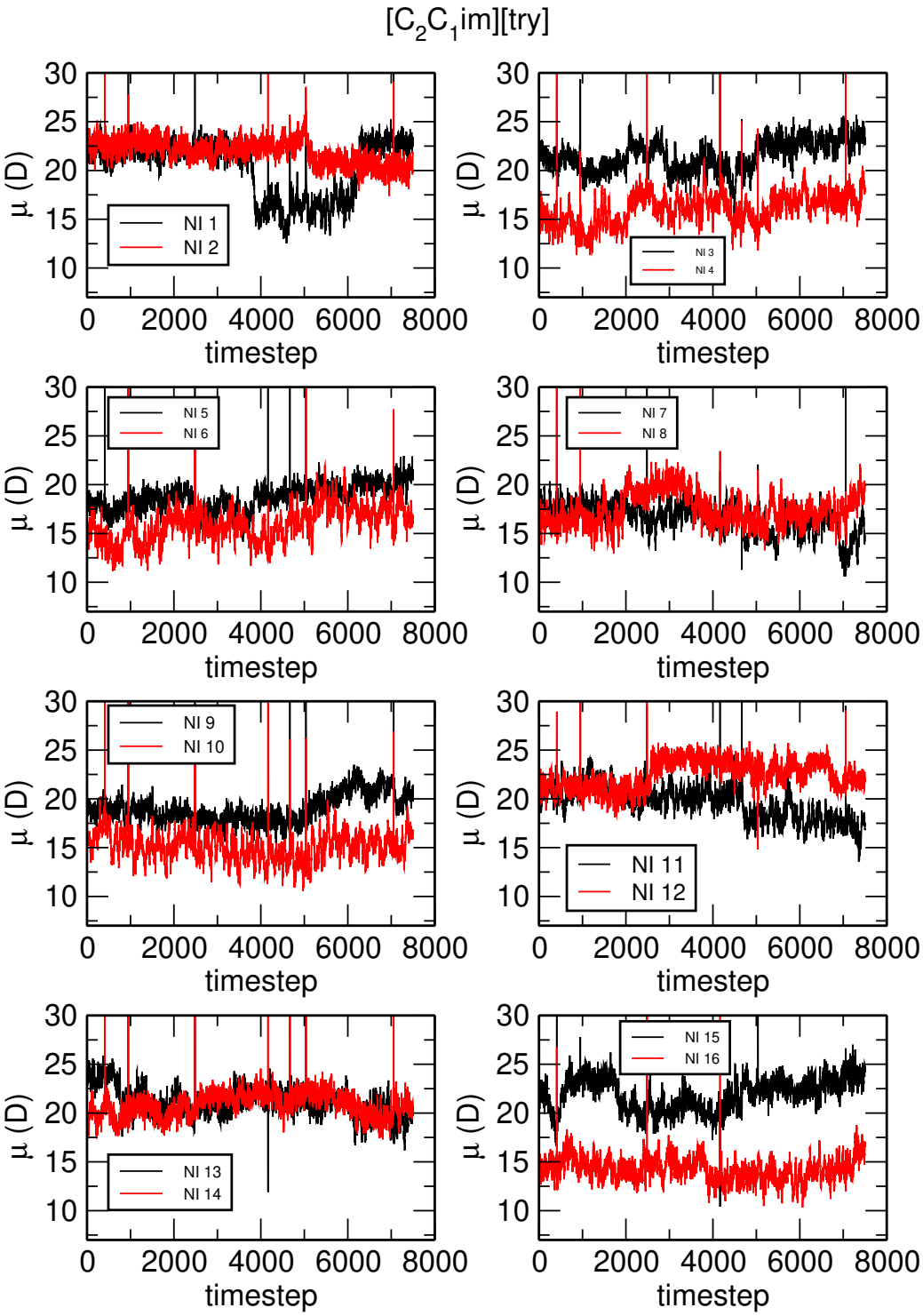

Figure S15: The every time development of the dipole moment (μ) of one randomly selected ion of anion in $[C_2C_1Im][trp]$.

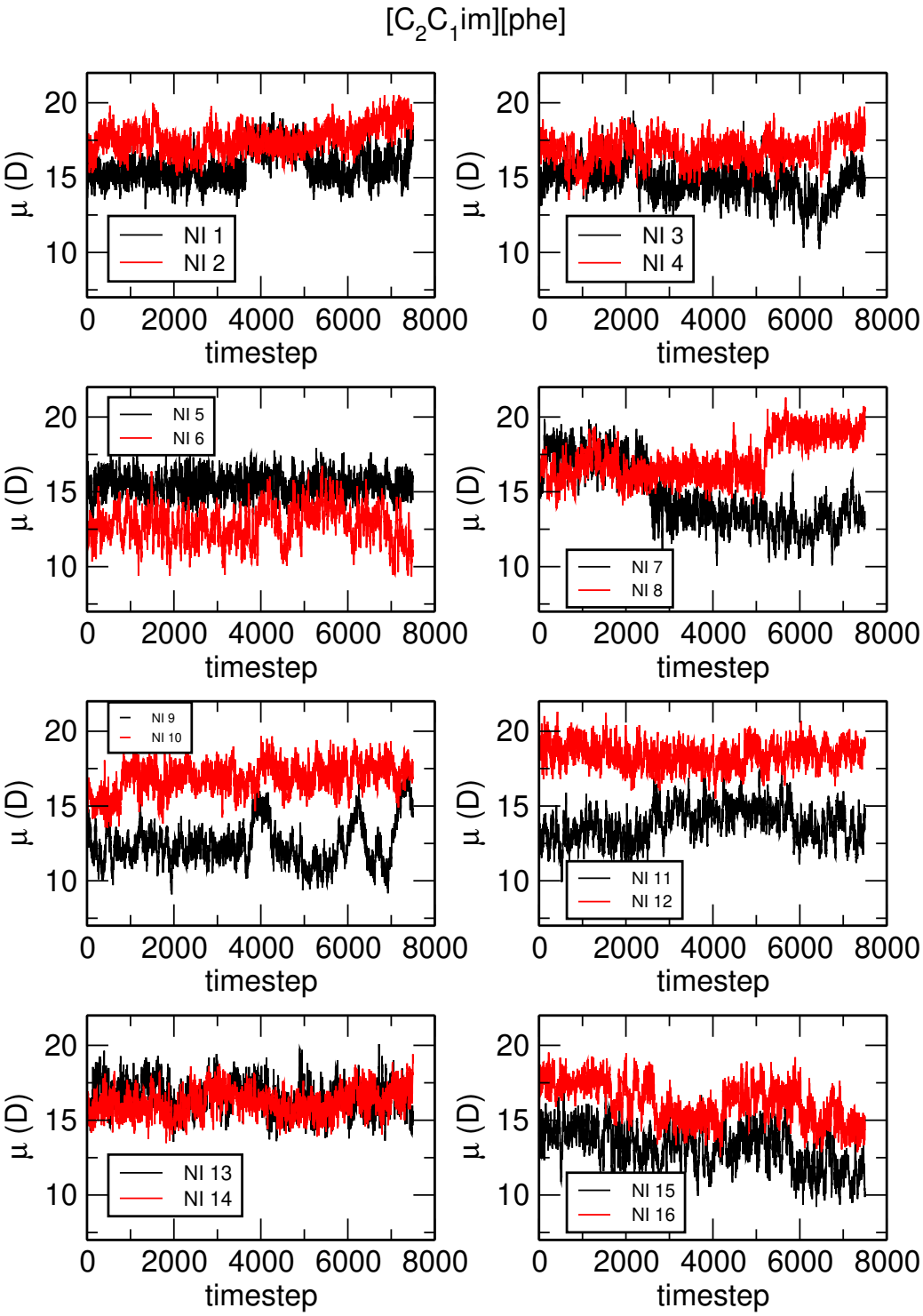

Figure S16: The every time development of the dipole moment (μ) of one randomly selected ion of anion in [C_2C_1Im][phe].

B. Vibrational Spectra Simulations in Amino Acid-Based Imidazolium Ionic Liquids

Wenbo Dong,* , Jan Blasius,* Zhijie Fan,† and Luke Wylie*

Received: 19 April 2024, Published online: 29 June 2024.

Reprinted with permission from [**W. Dong**, J. Blasius, Z. Fan, L. Wylie, *J. Phys. Chem. B* **2024**, *128*, 6560-6566

doi:10.1021/acs.jpcb.4c02555.]. Copyright [2024] American Chemical Society.‡

For this article, Supporting Information is available free of charge at:
https://doi.org/10.1021/acs.jpcb.4c02555.

Contributions to the manuscript

- Development of the concept
- Performing all simulations, analysis, and calculations
- Co-performing visualizations
- Interpretation of the results
- Writing of the manuscript

*Mulliken Center for Theoretical Chemistry, Clausius Institute for Physical and Theoretical Chemistry, University of Bonn, Beringstr. 4–6, 53115 Bonn, Germany

†Department of Chemistry, Imperial College London, South Kensington Campus, London SW7 2AZ, United Kingdom

THE JOURNAL OF PHYSICAL CHEMISTRY B
A JOURNAL OF THE AMERICAN CHEMICAL SOCIETY

pubs.acs.org/JPCB Article

Vibrational Spectra Simulations in Amino Acid-Based Imidazolium Ionic Liquids

Wenbo Dong, Jan Blasius, Zhijie Fan, and Luke Wylie*

Cite This: J. Phys. Chem. B 2024, 128, 6560−6566 Read Online

ACCESS | Metrics & More | Article Recommendations | Supporting Information

ABSTRACT: We present maximally localized Wannier functions and Voronoi tessellation to obtain dipole moment distributions for vibrational spectra in several important ionic liquids calculated by using ab initio molecular dynamics simulations. IR and Raman spectra of various imidazolium-based ionic liquids (ILs) paired with six amino acid anions are shown herein. For IR spectra, two approaches (Wannier and Voronoi) are in agreement with respect to the relative intensities and the overall shapes for the main peaks. Under Raman spectra, the polarizability of the covalent bonds is shown to affect the strength of the Raman scattering signal. The advantage of the Voronoi tessellation method, being that it does not have strong spikes in its time development, is demonstrated by the comparison of two theoretical methods (Wannier and Voronoi) with experimental data. We analyze the errors between theoretical and experimental spectroscopic data, with the Voronoi method shown to accurately reproduce experimental values. In addition, theoretical spectroscopy shows the ability to accurately separate components of a mixture. The combination of theoretical and experimental methods is utilized to understand the spectroscopic properties of amino acid-based imidazolium ILs.

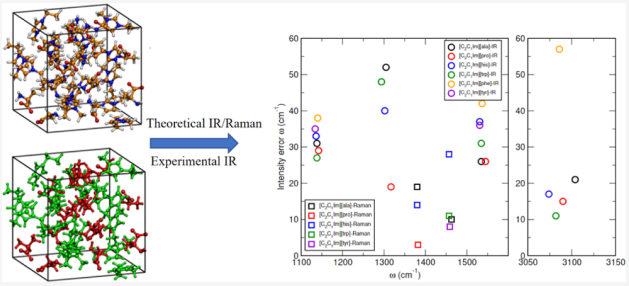

INTRODUCTION

Accurate prediction of vibration spectra is of vital importance in the field of computational chemistry, especially when using theory to prescreen for experiments. In 1997, Silvestrelli et al. evaluated the IR spectra of liquid water by using Car−Parrinello molecular dynamics (MD) to examine the impact of quantum correction on IR absorption.[1] When compared to other methods (such as the vibrational self-consistent field (VSCF)[2,3] and perturbative corrections to the harmonic approximation[4]), the approach based on ab initio molecular dynamics (AIMD) simulations is characterized by its ability to give conformation sampling in phase space and handling the electronic structure of molecular systems using the Born−Oppenheimer approximation.[5] Similarly, the power spectrum can be obtained through performing a Fourier transformation of the particle velocities autocorrelation.[6] IR and Raman spectroscopy also require autocorrelation of the dipole moment and molecular polarizability.

Maximally localized Wannier functions (MLWFs) are a powerful approach used to obtain the dipole moments of individual molecules.[7−10] The dipole moment can provide an insight into the properties of chemical bonds (such as nonbonded electron pairs). Furthermore, the finite differences of dipole moments can be used to determine the magnitude of polarizability.[11] In the case of theoretical part, the IR absorption can be determined through several methods, such as the comparison of different calculation methods of IR in crystalline systems[12] or decomposing total IR aqueous systems to their solute and solvent contributions.[13] Similarly, previous research on Raman spectra prediction involved the application in gas or bulk phase cyclohexane vibrational spectra.[11,14] MLWFs centers allow every orbital to be assigned to a molecule, requiring a huge amount of computational resources for localization, with this being more computationally intensive than the calculation of the electronic structure. To calculate IR or Raman spectra, one solution often applied is to divide the total electron density by the molecular contributions. Various approaches (such as the nonempirical atoms-in-molecules method[15] and Hirshfeld partitioning[16]) are primarily used to assign atomic partial charges in molecules. Voronoi tessellation is a method that divides the space of the simulation cell.[17] In the Voronoi method, each point of space is assigned to exactly one cell, and the faces of the cells are always placed midway between two atoms.

In past years, IR and Raman spectroscopy showed insight vital to the characterization of ionic liquids (ILs).[18−20] A study by Wulf et al. combined theoretical DFT calculations and experimental methods to investigate the spectral properties of

Received: April 19, 2024
Revised: June 21, 2024
Accepted: June 21, 2024
Published: June 29, 2024

https://doi.org/10.1021/acs.jpcb.4c02555
J. Phys. Chem. B 2024, 128, 6560−6566

imidazolium-based ILs.[19] Furthermore, the review by Paschoal et al. showed the application of computationally calculated vibrational spectroscopy to study phase transitions in ILs.[18]

In a prior study by our group, we presented the power spectra of several imidazolium-based ILs based on AIMD simulations.[21] In this study, to gain further understanding of vibrational spectra, we investigated spectra that were calculated for several different amino acids with varying anions, while 1-ethyl-3-methylimidazolium ($[C_2C_1Im]$) was kept consistent as the cation. This ability to theoretically produce accurate IR and Raman spectra with AIMD simulations is applied in this study.

METHODS

Computational Details. In this project, the NpT ensemble was used to obtain the equilibrium density with the barostat applying pressure of 1 bar, a temperature of 370 K, and 500 ion pairs to the systems. These simulations were run for 10 ns using MD simulations. The LAMMPS software package[22] was used for classical MD simulations with the OPLS-AA[23] as well as the Canongia Lopes and Padua (CL&P) force field parameters.[24,25] The final simulation boxes contained 16 ion pairs. Following this, the production AIMD simulations were performed in the NVT ensemble with a time step of 0.5 fs applied and a temperature of 370 K employing a Nosé−Hoover chain thermostat.[26,27] The equilibration was run for 10 ps (20 000 steps) with a massive thermostatting coupling constant of 10 fs. The following production run was simulated for 30 ps (60 000 steps) employing a global thermostat and a thermostat coupling constant of 50 fs. The CP2K software was used to perform AIMD simulations.[28] The BLYP functional[29,30] was applied in combination with the corresponding BLYP Goedecker−Teter−Hutter pseudopotentials[31−33] for core electrons. The simulations used the molecularly optimized double-ζ basis set (MOLOPT-DZVP-SR-GTH).[34] DFT-D3 correction was used to account for dispersion interactions.[35,36] Dipole moments and polarizations were calculated using the Wannier method and Voronoi tessellation[8,37] as implemented in CP2K.[28] TRAVIS (Trajectory Analyzer and Visualizer)[38,39] was used to analyze the trajectories obtained from simulations. Types of analysis that will be performed using TRAVIS in this study will be dipole moment distribution calculations, as well as production of theoretically calculated IR and Raman spectra.

Methodology. In regard to the dipole moment calculation in a bulk phase AIMD simulation, Wannier functional centers are located near molecules, allowing each center to be assigned to a molecule differently based on a minimum distance criterion. The dipole moment is calculated through the sum of all Wannier function centers assigned and over all nuclei of the molecule with the charges Z_A and positions R_A

$$\mu = -2e\sum_{i=1}^{N} r_i + e\sum_{A=1}^{M} Z_A R_A \tag{1}$$

where e is the elementary charge. The molecular polarizability is defined as

$$\mu_{ind} = \alpha E \tag{2}$$

Here, α is the second-order polarizability tensor and E is an electric field.

The Voronoi tessellation[11,17] is a simple way to divide the space of analog cells, and it defines n Voronoi cells C_i as

$$C_i = \{X \in R^3 | r_i^2 \le (x - s_j)^2 - r_j^2 \ \forall\, j \ne i\},\ i, j = 1, \ldots, n. \tag{3}$$

This equation takes a set of n sites s_i as input, meaning that cell C_i contains all points that are closer to site s_i than to any other site. The Voronoi tessellation assigns each point in space to precisely one cell. The cell faces are always positioned midway between the two atoms. In the radical Voronoi tessellation method, which can extend the partitioning scheme and allow keeping the Voronoi sites at the atom positions, when radius r_i is assigned to each site, the cells C_i^r is determined according to

$$C_i^r = \{X \in R^3 | (x - s_i)^2 - r_i^2 \le (x - s_j)^2 - r_j^2 \ \forall\, j \ne i\},\ i, j = 1, \ldots, n. \tag{4}$$

Here, the distance to the sites themselves from the original Voronoi tessellation is changed to the power distance to spheres around the sites. For each cell, the charge calculation is

$$q_i = \int_{C_i^r} \rho(r)\mathrm{d}r \tag{5}$$

and the dipole moment

$$\mu = \int_{C_i^r} r\rho(r)\mathrm{d}r \tag{6}$$

The polarizability tensor $\bar{\alpha}(\boldsymbol{Q})$ is expanded in the Taylor series

$$\bar{\alpha}(\boldsymbol{Q}) = \bar{\alpha}_0 + \sum_{k=1}^{g} \frac{\partial\bar{\alpha}(\boldsymbol{Q})}{\partial \boldsymbol{Q}_k}_{0} \boldsymbol{Q}_k \tag{7}$$

The $\bar{\alpha}(\boldsymbol{Q})$ is the polarizability depending on the mass-weighted normal coordinates $\boldsymbol{Q}$. IR and Raman intensities are influenced by the dipole moment and polarization.[40,41] Trajectories were analyzed with the TRAVIS software package.[38,42] When considering the general three-dimensional case, the definition of wavenumber-dependent IR absorption $A(\tilde{\nu})$ is

$$A(\tilde{\nu}) = \frac{N_A}{12\varepsilon_0 c k_B T}\int \langle \dot{\mu}(\tau)\cdot\dot{\mu}(\tau + t)\rangle_\tau \exp^{-2\pi i c\tilde{\nu}t}\,\mathrm{d}t \tag{8}$$

Here, t and τ denote the time, N_A is Avogadro's constant, ε_0 is the vacuum permittivity, c is the speed of light in vacuum, k_B is the Boltzmann constant, T is the average simulation temperature (in kelvin), and $\langle \dot{\mu}(\tau)\cdot\dot{\mu}(\tau + t)\rangle_\tau$ defines the autocorrelation function of the dipole moment time derivative. Replacing the polarizability by dipole moment, the wavenumber in Raman is given as

$$I(\tilde{\nu}) = \frac{h}{8\varepsilon_0^2 k_B T}\frac{(\tilde{\nu}_{in} - \tilde{\nu})^4}{\tilde{\nu}\left(1 - \exp\left(-\frac{hc\tilde{\nu}}{k_B T}\right)\right)} \cdot \int (\langle \dot{\alpha}_{xx}(\tau)\dot{\alpha}_{xx}(t + \tau)\rangle_\tau + \langle \dot{\alpha}_{xy}(\tau)\dot{\alpha}_{xy}(t + \tau)\rangle_\tau)\exp^{-2\pi i c\tilde{\nu}t}\mathrm{d}t \tag{9}$$

where α denotes the polarization, h is the Planck constant, and $\tilde{\nu}_{in}$ is the laser wavenumber, which in all cases was set to 20 000 cm^{-1}.

Systems Investigated. In this study, various ILs, which all contain $[C_2C_1Im]^+$ as the cations, were selected. We investigated several amino acids, namely, (L)-alaninate

https://doi.org/10.1021/acs.jpcb.4c02555
J. Phys. Chem. B 2024, 128, 6560−6566

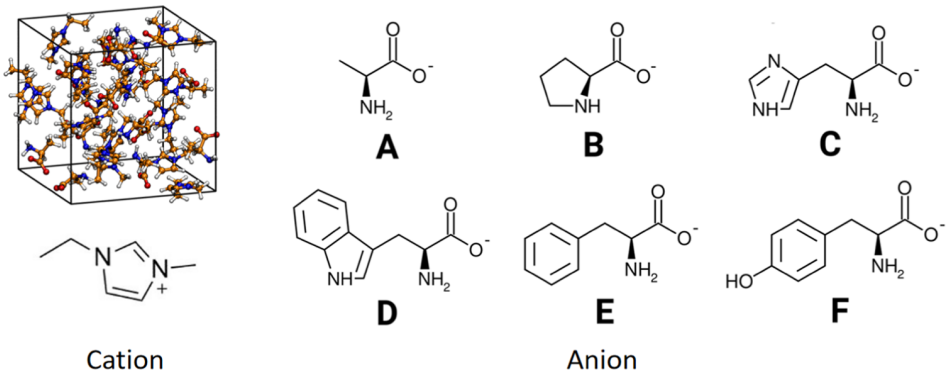

Figure 1. Left panel shows the snapshot of the $[C_2C_1Im][ala]$ simulation box and cation $[C_2C_1Im]^+$. Right panel shows the different anions (A) $[ala]^-$, (B) $[pro]^-$, (C) $[his]^-$, (D) $[trp]^-$, (E) $[phe]^-$, and (F) $[tyr]^-$. Color code for the ball-and-stick images as well as for the left simulation box is as follows: carbon, orange; oxygen, red; nitrogen, blue; and hydrogen, white.

([ala]$^-$), (L)-prolinate ([pro]$^-$), (L)-histidinate ([his]$^-$), (L)-phenylalaninate ([phe]$^-$), (L)-tryptophanate ([trp]$^-$), and (L)-tyrosinate ([tyr]$^-$) in their anionic state, which are shown in Figure 1. All simulations were conducted using 16 ion pairs. The theoretical densities, compositions, and box sizes are shown in Table 1.

Table 1. Theoretical Densities $\rho_{350\,K}$ and Box Sizes a of the Simulation Boxes

quantity	[ala]$^-$	[pro]$^-$	[his]$^-$
$\rho_{350\,K}$ (g cm^{-1})	1.086	1.070	1.064
a (Å)	16.96	17.66	18.65
quantity	[trp]$^-$	[phe]$^-$	[tyr]$^-$
$\rho_{350\,K}$ (g cm^{-1})	1.093	1.089	1.139
a (Å)	19.70	18.89	19.25

DISCUSSION AND RESULTS

Theoretical Spectroscopy. In prior studies, IR and Raman spectra from Voronoi tessellation and Wannier function centers for methanol, benzene, and phenol were investigated.[11] These schemes were shown to give changes in agreement when compared to the experimental data with results obtained from the Wannier and Voronoi methods for benzene, and the additional band observed is from 1200 to 1350 cm^{-1} in spectra calculated using the Wannier method. Here, it is shown that the Voronoi approach gives a closer representation of the experiment and lower errors when calculating IL spectra. In this study, two methods (Voronoi tessellation and Wannier function) were assessed for their ability to accurately predict IR spectra.

As shown in Figures 2 and 3, all approaches agree with respect to relative intensities and the overall shapes for these main peaks (around 1500 and 3000 cm^{-1}). Among these, 1500 cm^{-1} corresponds to the vibrations within the C═O stretching in anions, while the signal at 3000 cm^{-1} is due to the aromatic ═CH stretching band predominantly stemming from the cation. Comparing the same cations in various systems, the spectra produced were relatively similar, with the exception of $[C_2C_1Im][trp]$ and $[C_2C_1Im][tyr]$ systems when using the Wannier method. In this instance, a stronger signal was shown in the region of 3000 cm^{-1}, which confirms observations from a prior study.[11] The intensity of the relative peaks with

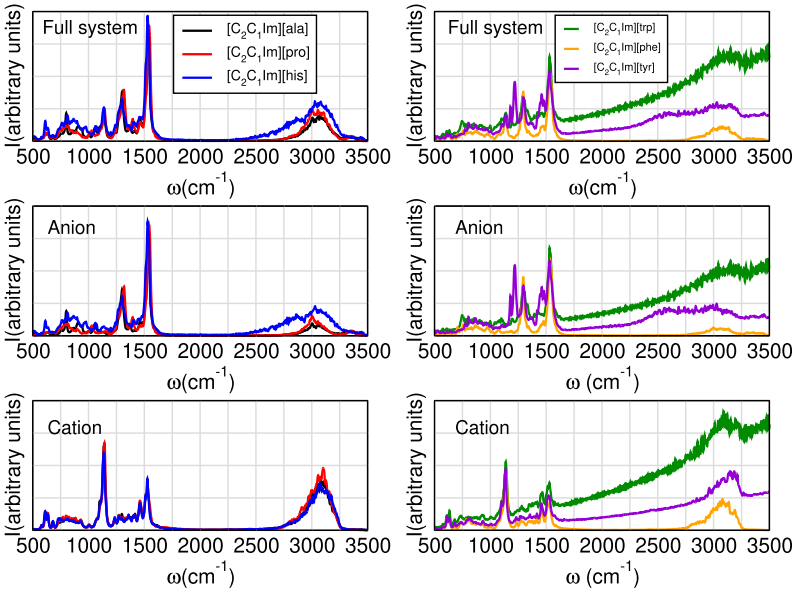

Figure 2. IR spectra calculated using the Wannier methodology of all ILs analyzed.

https://doi.org/10.1021/acs.jpcb.4c02555
J. Phys. Chem. B 2024, 128, 6560−6566

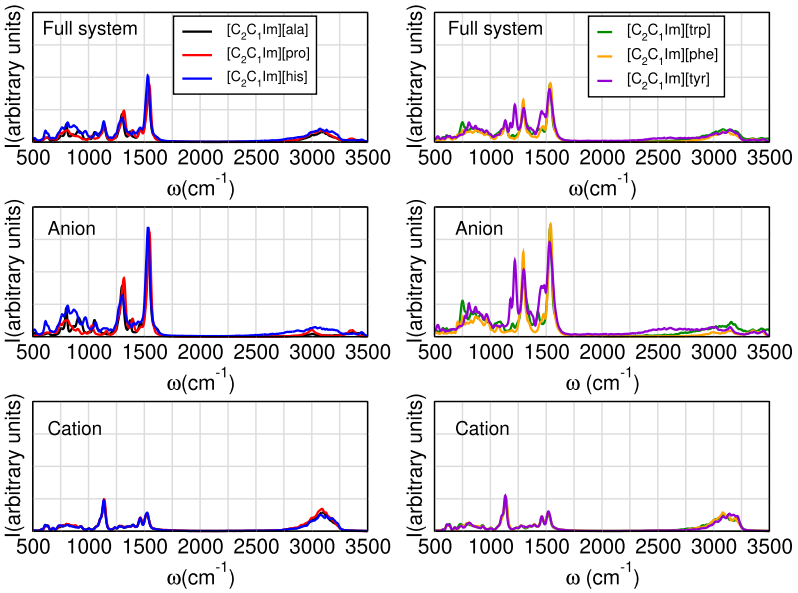

Figure 3. IR spectra from analysis using Voronoi tessellation analysis of all ILs determined and analyzed.

Voronoi dipole moments decreased from those obtained using the Wannier method, especially around 3000 cm^{-1}. However, the broad band around 3000 cm^{-1} should be assigned to the cation and not to the anions.[42] This is to say, when assigning peaks to anions and cations, the Voronoi method outperforms the Wannier method.

In addition, the peak intensities of spectra calculated using the Voronoi method were slightly reduced, as a result of molecules in the Wannier method remaining static while the Voronoi cells' electron density could move. These results reinforce the trends found in several common molecular liquids (methanol, benzene, and phenol).[11] There are broad bands in the spectra of the anions of all systems around 3000 cm^{-1}, with the Wannier approach. Comparing the IR spectra of the anions between the Wannier and Voronoi approaches, the Voronoi method specifically shows weak intensities. Meanwhile, $[C_2C_1Im]^+$ possesses three broad modes of C−H stretching vibrations in ring hydrogen atoms, suggesting that the IR intensity is partially transferred from cations to anions. The Wannier method can assign a large portion of the intensity to anions, especially for $[C_2C_1Im][trp]$, while in Voronoi almost no anions contribute to this band. This is due to Wannier functional centers not being strictly assigned to individual molecules in the system, which is more obvious in the higher dipole moment value system.

For the Raman spectra, if the Wannier localization does not converge to the same bonding mode in both calculations with and without an external electric field, flipping the dipole vector will strongly disturb the change in the dipole moment induced by the electric field. This increases the resulting polarizability by several orders of magnitude, leads to a strong spike in its temporal development, and makes the Fourier transformation unsuitable for Raman.[11] To investigate how polarization affects Raman spectra, AIMD simulations employing the Voronoi tessellation approach are investigated, as shown in Figure 4. $[C_2C_1Im][trp]$, $[C_2C_1Im][phe]$, and $[C_2C_1Im][tyr]$ show up to 2 times higher Raman intensity, specifically in the signals of the anions, compared to other systems analyzed. The strength of the Raman scattering signal is related to the polarizability of the covalent bonds.[43] In all systems, the cation shows

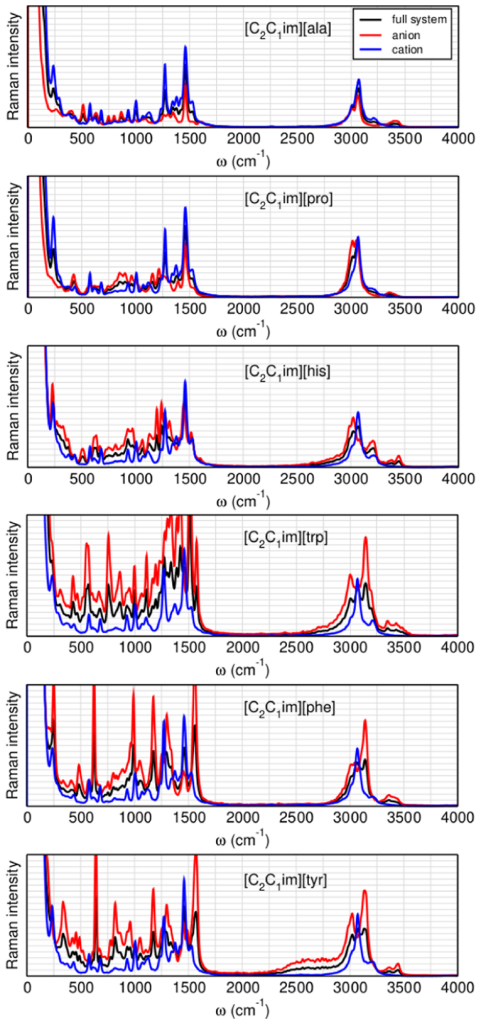

Figure 4. Raman spectra from analysis using Voronoi tessellation analysis for all systems as calculated theoretically using AIMD.

https://doi.org/10.1021/acs.jpcb.4c02555
J. Phys. Chem. B 2024, 128, 6560−6566

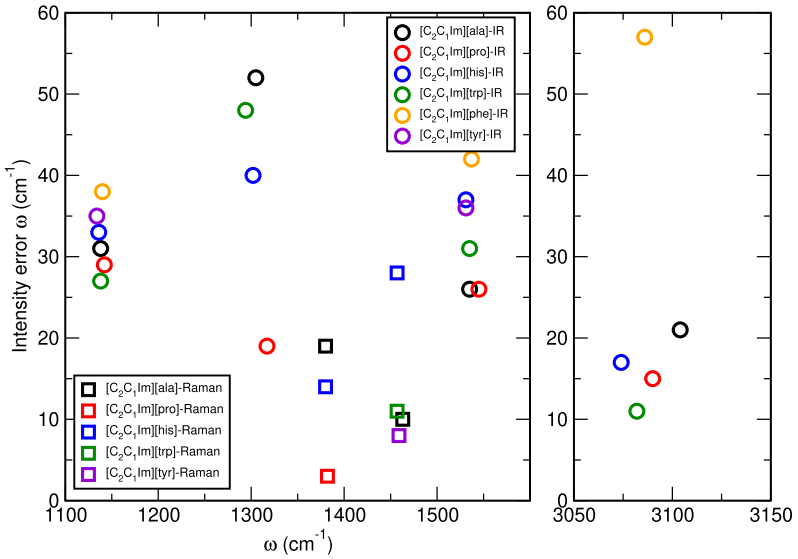

Figure 5. Comparison of theoretical wavenumber (X) and the error between experimental and theoretical data (Y).

negligible differences in polarization. By comparing this region (below 1500 cm^{-1}) with IR, the peaks of C−H bending vibrations can be accurately predicted in the Raman spectra. There was no apparent red shift or blue shift at any cation-induced signal; this showed that the bond energy remained relatively consistent between the ILs tested.

Experimental Spectroscopy. *Spectroscopic Analysis.* A detailed comparison of the main peak positions in IR and Raman data obtained theoretically (Voronoi) and IR experimental data is shown in Tables S2 and S3, and Figures S1−S4 of the SI. The theoretical data show a good correspondence to the IR experimental data (Figures S4−S9 in the SI). Among these, the most intense band of all systems in both theory and experiment is connected to the antisymmetric C═O antisymmetric stretch mode in anion molecules (around 1550 cm^{-1}). The peaks around 3050 cm^{-1} are very sensitive to small changes in intermolecular interactions, particularly hydrogen bonding, and can be affected by the presence of water. The peaks show good correspondence with the experimental data and theoretical data of the anion in all systems. In addition, on the experimental spectra, all systems show evidence of a broad peak at approximately 3300 cm^{-1}, which is indicative of exposure to water vapor during the measurement. Specifically, the signals around 1100 and 1350 cm^{-1} relate to the in-plane $C_{Im}H$ bending in the cation and CH_2 bending in the anions ([C_2C_1Im][ala] also contains CH_3 bending). When focusing on the theoretically obtained Raman data, the two peaks around 1350 and 1450 cm^{-1} are attributed to the $C_{Im}N$ stretch and $C_{Et}H$ bend, which are manifested in the cation signals. The theoretical IR only shows anion $C_{Im}H$ stretching; however, the theoretical Raman illustrates both the −CH stretching from the unsaturated hydrocarbon and saturated hydrocarbon. The C−N stretching is mainly concentrated in the range of 1030−1350 cm^{-1}.

Comparison of Experimental and Theoretical Spectroscopy. Figure 5 shows the comparison between the theoretical wavenumber and the error between experimental and theoretical data of 6 IL systems. Tables 2 and 3 present the notable vibrational wavenumbers in the theoretical IR spectra (Voronoi), theoretical Raman spectra (Voronoi) and experimental IR spectra of [C_2C_1Im][ala] and [C_2C_1Im][tyr]. From this, it is shown that below 1600 cm^{-1}, the peak numbers of theoretical data of the structure in 6 ILs have a strong correlation. The theoretical data peak numbers around 3100 cm^{-1} are in the range of 3050 and 3150 cm^{-1}, which contain an error of around 15 cm^{-1}, except in the case of [C_2C_1Im][phe]. For peaks with wavenumbers around 1150 cm^{-1} ($C_{Im}H$ bend), a similar value is seen between all 6 ILs, with an average error of 32 cm^{-1} and all errors being between 25 and 40 cm^{-1}. All of the error values are below 60 cm^{-1} and the lowest error reaches 3 cm^{-1}. Overall, the theoretical Raman

Table 2. Notable Vibrational Wavenumbers in the IR Spectra of [C_2C_1Im][ala] and Comparison of Experimental Wavenumbers ω_{exp} (cm^{-1}) and Theoretical Wavenumbers (Voronoi) ω_{the} (cm^{-1})

ω_{exp} (cm^{-1})	ω_{the} (IR) (cm^{-1})	ω_{the} (Raman) (cm^{-1})	description
1169	1138		$C_{Im}H$ bend
1357	1305		$C_{ala}H_2$ bend, $C_{ala}H_3$ bend
1399		1380	$C_{Et}H$ bend, $C_{Im}N$ stretch
1453		1463	$C_{Et}H$ bend
1561	1535		C_{ala}═O stretch
2111			water
2597			water
3083	3104		═$C_{Im}H$ stretch

Table 3. Notable Vibrational Wavenumbers in the IR Spectra of [C_2C_1Im][tyr] and Comparison of Experimental Wavenumbers ω_{exp} (cm^{-1}) and Theoretical Wavenumbers (Voronoi) ω_{the} (cm^{-1})

ω_{exp} (cm^{-1})	ω_{the} (cm^{-1}) (IR)	ω_{the} (cm^{-1}) (Raman)	description
1169	1134		$C_{Im}H$ bend
1244	1219		phenyl-*O* stretch
1451		1459	$C_{Et}H$ bend
1567	1531		C_{tyr}═O stretch
2978			$C_{tyr}H$ stretch
	3143		═$C_{Im}H$ stretch

https://doi.org/10.1021/acs.jpcb.4c02555
J. Phys. Chem. B 2024, 128, 6560−6566

data agree better with experimental data than the theoretical IR, with an average error of 12 cm^{-1} in Raman (around 1375 cm^{-1}) and 33 cm^{-1} in the IR (around 1550 cm^{-1}). The averages of other peaks are 40 cm^{-1} (around 1300 cm^{-1}), 14 cm^{-1} (around 1450 cm^{-1}), and 24 cm^{-1} (around 3100 cm^{-1}).

One of the advantages of obtaining vibrational spectra theoretically is that they can be used to assign individual signals to either the cation or the anion, which is not possible in experimental spectroscopy. For instance, in theoretical IR, the strongest signal in the anion (around 1550 cm^{-1}) corresponds to the C_{an}=O stretch and the strongest signal in the cation (around 1100 cm^{-1}) corresponds to the C_{Im} bend further assisting the analysis. In addition, in the $[C_2C_1Im][tyr]$ system (Table 3), the peak of 1219 cm^{-1} can be found only in the theoretically predicted IR spectra of the anion component (Figure 3), which corresponds to the phenyl-*O* (phenol) stretch vibration. On the other hand, the experimental data of 2978 cm^{-1} show the −CH stretching due to saturated hydrocarbons in the anion. Although this signal may be difficult to detect in theoretically predicted IR, it can be predicted using theoretically generated Raman spectra. The separation of the cation and anion using theoretical data can be used to give a detailed analysis of dipole moments and polarizabilities.[43] Theoretical spectroscopic analysis shows that the IR is mainly dominated by anion vibrations, whereas Raman is predominantly composed of cationic vibrations. In addition to allowing the separation of components within the mixture, theoretically determined vibrational spectra also helped to remove contaminants, such as water. Experimental IR (Figure S2) shows a wavenumber of water at 1450 cm^{-1}. Due to the somewhat overlapping peak of CH bending in $[C_2C_1Im][pro]$ at 1461 cm^{-1}, this is not detected experimentally and requires theoretical determination. Therefore, using AIMD to predict the IR and Raman spectra on various amino acid IL systems has advantages over solely using experimental methods to characterize and understand vibrational spectra.

CONCLUSIONS

In this work, IR and Raman spectroscopy were calculated based on AIMD simulations in six amino acid-based imidazolium ILs. The results indicated that for ILs, the Voronoi tessellation method is advantageous over MLWFs for systems with significant charge transfer. The theoretical data for both IR and Raman show consistency with experimental data for the most notable peaks. The combination of theory and experiment is capable of presenting more detailed data, such as theoretical data helping to isolate ions within the mixture and removing water. In the future, this may have applications in IL spectra research using AIMD analysis and for the understanding of IL vibrational activity such as in complex mixtures or at interfaces.

ASSOCIATED CONTENT

Supporting Information

The Supporting Information is available free of charge at https://pubs.acs.org/doi/10.1021/acs.jpcb.4c02555.

Experimental methodology; figures of theoretical Raman spectrum; figures of experimental IR spectrum; and tables of notable vibrational wavenumber (PDF)

AUTHOR INFORMATION

Corresponding Author

Luke Wylie − *Mulliken Center for Theoretical Chemistry, University of Bonn, D-53115 Bonn, Germany*; orcid.org/0000-0001-8306-7400; Email: wylie@thch.uni-bonn.de

Authors

Wenbo Dong − *Mulliken Center for Theoretical Chemistry, University of Bonn, D-53115 Bonn, Germany*

Jan Blasius − *Mulliken Center for Theoretical Chemistry, University of Bonn, D-53115 Bonn, Germany*

Zhijie Fan − *Department of Chemistry, Imperial College London, London SW7 2AZ, U.K.*

Complete contact information is available at: https://pubs.acs.org/10.1021/acs.jpcb.4c02555

Notes

The authors declare no competing financial interest.

ACKNOWLEDGMENTS

The authors thank the DFG under grant project number 406232243, the China Scholarship Council (CSC) for the basis funding, as well as the support of IMPRS-RECHARGE and the computational resources and assistance in generating ideas from Barbara Kirchner.

REFERENCES

(1) Silvestrelli, P. L.; Bernasconi, M.; Parrinello, M. Ab initio infrared spectrum of liquid water. *Chem. Phys. Lett.* **1997**, *277*, 478−482.

(2) Bowman, J. M. The self-consistent-field approach to polyatomic vibrations. *Acc. Chem. Res.* **1986**, *19*, 202−208.

(3) Jung, J. O.; Gerber, R. B. Vibrational wave functions and spectroscopy of (H2O) n, n = 2, 3, 4, 5: Vibrational self-consistent field with correlation corrections. *J. Chem. Phys.* **1996**, *105*, 10332−10348.

(4) Cappelli, C.; Monti, S.; Scalmani, G.; Barone, V. On the calculation of vibrational frequencies for molecules in solution beyond the harmonic approximation. *J. Chem. Theory Comput.* **2010**, *6*, 1660−1669.

(5) Fischer, S. A.; Ueltschi, T. W.; El-Khoury, P. Z.; Mifflin, A. L.; Hess, W. P.; Wang, H.-F.; Cramer, C. J.; Govind, N. Infrared and Raman spectroscopy from ab initio molecular dynamics and static normal mode analysis: The C−H region of DMSO as a case study. *J. Phys. Chem. B* **2016**, *120*, 1429−1436.

(6) Futrelle, R.; McGinty, D. Calculation of spectra and correlation functions from molecular dynamics data using the fast Fourier transform. *Chem. Phys. Lett.* **1971**, *12*, 285−287.

(7) Wannier, G. H. The structure of electronic excitation levels in insulating crystals. *Phys. Rev.* **1937**, *52*, 191.

(8) Kirchner, B.; Hutter, J. Solvent effects on electronic properties from Wannier functions in a dimethyl sulfoxide/water mixture. *J. Chem. Phys.* **2004**, *121*, 5133−5142.

(9) Gaigeot, M.-P.; Vuilleumier, R.; Sprik, M.; Borgis, D. Infrared spectroscopy of N-methylacetamide revisited by ab initio molecular dynamics simulations. *J. Chem. Theory Comput.* **2005**, *1*, 772−789.

(10) Zahn, S.; Wendler, K.; Delle Site, L.; Kirchner, B. Depolarization of water in protic ionic liquids. *Phys. Chem. Chem. Phys.* **2011**, *13*, 15083−15093.

(11) Thomas, M.; Brehm, M.; Kirchner, B. Voronoi dipole moments for the simulation of bulk phase vibrational spectra. *Phys. Chem. Chem. Phys.* **2015**, *17*, 3207−3213.

(12) Dovesi, R.; Kirtman, B.; Maschio, L.; Maul, J.; Pascale, F.; Rérat, M. Calculation of the infrared intensity of crystalline systems. A comparison of three strategies based on Berry phase, Wannier

function, and coupled-perturbed Kohn−Sham methods. *J. Phys. Chem. C* **2019**, *123*, 8336−8346.
(13) Iftimie, R.; Tuckerman, M. E. Decomposing total IR spectra of aqueous systems into solute and solvent contributions: A computational approach using maximally localized Wannier orbitals. *J. Chem. Phys.* **2005**, *122*, 214508.
(14) Partovi-Azar, P.; Kühne, T. D. Full Assignment of Ab-Initio Raman Spectra at Finite Temperatures Using Wannier Polarizabilities: Application to Cyclohexane Molecule in Gas Phase. *Micromachines* **2021**, *12*, 1212.
(15) Manz, T. A.; Sholl, D. S. Improved atoms-in-molecule charge partitioning functional for simultaneously reproducing the electrostatic potential and chemical states in periodic and nonperiodic materials. *J. Chem. Theory Comput.* **2012**, *8*, 2844−2867.
(16) Bultinck, P.; Van Alsenoy, C.; Ayers, P. W.; Carbó-Dorca, R. Critical analysis and extension of the Hirshfeld atoms in molecules. *Chem. Phys.* **2007**, *126*, 144111.
(17) Pokojski, W.; Pokojska, P. Voronoi diagrams−inventor, method, applications. *Pol. Cartographical Rev.* **2018**, *50*, 141−150, DOI: 10.2478/pcr-2018-0009.
(18) Paschoal, V. H.; Faria, L. F.; Ribeiro, M. C. Vibrational spectroscopy of ionic liquids. *Chem. Rev.* **2017**, *117*, 7053−7112.
(19) Wulf, A.; Fumino, K.; Michalik, D.; Ludwig, R. IR and NMR properties of ionic liquids: Do they tell us the same thing? *ChemPhysChem* **2007**, *8*, 2265−2269.
(20) Yang, Y.-l.; Kou, Y. Determination of the Lewis acidity of ionic liquids by means of an IR spectroscopic probe. *Chem. Commun.* **2004**, 226−227.
(21) Wendler, K.; Brehm, M.; Malberg, F.; Kirchner, B.; Delle Site, L. Short time dynamics of ionic liquids in AIMD-based power spectra. *J. Chem. Theory Comput.* **2012**, *8*, 1570−1579.
(22) Plimpton, S. Fast parallel algorithms for short-range molecular dynamics. *J. Comput. Phys.* **1995**, *117*, 1−19.
(23) Jorgensen, W. L.; Maxwell, D. S.; Tirado-Rives, J. Development and testing of the OPLS all-atom force field on conformational energetics and properties of organic liquids. *J. Am. Chem. Soc.* **1996**, *118*, 11225−11236.
(24) Canongia Lopes, J. N.; Deschamps, J.; Pádua, A. A. Modeling ionic liquids using a systematic all-atom force field. *J. Phys. Chem. B* **2004**, *108*, 2038−2047.
(25) Canongia Lopes, J. N.; Pádua, A. Molecular force field for ionic liquids III: Imidazolium, pyridinium, and phosphonium cations; chloride, bromide, and dicyanamide anions. *J. Phys. Chem. B* **2006**, *110*, 19586−19592.
(26) Nosé, S. A unified formulation of the constant temperature molecular dynamics methods. *J. Chem. Phys.* **1984**, *81*, 511−519.
(27) Hoover, W. G. Canonical dynamics: Equilibrium phase-space distributions. *Phys. Rev. A* **1985**, *31*, 1695.
(28) Kühne, T. D.; Iannuzzi, M.; Del Ben, M.; Rybkin, V. V.; Seewald, P.; Stein, F.; Laino, T.; Khaliullin, R. Z.; Schütt, O.; Schiffmann, F.; et al. CP2K: An electronic structure and molecular dynamics software package-Quickstep: Efficient and accurate electronic structure calculations. *J. Chem. Phys.* **2020**, *152*, 194103 DOI: 10.1063/5.0007045.
(29) Perdew, J. P. Density-functional approximation for the correlation energy of the inhomogeneous electron gas. *Phys. Rev. B* **1986**, *33*, 8822.
(30) Becke, A. D. Density-functional exchange-energy approximation with correct asymptotic behavior. *Phys. Rev. A* **1988**, *38*, 3098.
(31) Goedecker, S.; Teter, M.; Hutter, J. Separable dual-space Gaussian pseudopotentials. *Phys. Rev. B* **1996**, *54*, 1703.
(32) Hartwigsen, C.; Gœdecker, S.; Hutter, J. Relativistic separable dual-space Gaussian pseudopotentials from H to Rn. *Phys. Rev. B* **1998**, *58*, 3641.
(33) Krack, M. Pseudopotentials for H to Kr optimized for gradient-corrected exchange-correlation functionals. *Theor. Chem. Acc.* **2005**, *114*, 145−152.
(34) VandeVondele, J.; Hutter, J. Gaussian basis sets for accurate calculations on molecular systems in gas and condensed phases. *J. Chem. Phys.* **2007**, *127*, 114105.
(35) Grimme, S.; Antony, J.; Ehrlich, S.; Krieg, H. A consistent and accurate ab initio parametrization of density functional dispersion correction (DFT-D) for the 94 elements H-Pu. *J. Chem. Phys.* **2010**, *132*, 154104.
(36) Grimme, S.; Ehrlich, S.; Goerigk, L. Effect of the damping function in dispersion corrected density functional theory. *J. Comput. Chem.* **2011**, *32*, 1456−1465.
(37) Aurenhammer, F. Voronoi diagrams—a survey of a fundamental geometric data structure. *ACM Comput. Surv.* **1991**, *23*, 345−405.
(38) Brehm, M.; Kirchner, B. TRAVIS-a free analyzer and visualizer for Monte Carlo and molecular dynamics trajectories. *J. Chem. Inf. Model.* **2011**, *51*, 2007−2023.
(39) Brehm, M.; Thomas, M.; Gehrke, S.; Kirchner, B. TRAVIS-A free analyzer for trajectories from molecular simulation. *J. Chem. Phys.* **2020**, *152*, 164105.
(40) Liu, H.; Wang, Y.; Bowman, J. M. Quantum calculations of the IR spectrum of liquid water using ab initio and model potential and dipole moment surfaces and comparison with experiment. *J. Chem. Phys.* **2015**, *142*, 194502.
(41) Tuschel, D.Practical group theory and Raman spectroscopy, part II: Application of polarization *Spectroscopy* 2014; Vol. *29*, pp 14−21.
(42) Thomas, M.; Brehm, M.; Fligg, R.; Vöhringer, P.; Kirchner, B. Computing vibrational spectra from ab initio molecular dynamics. *Phys. Chem. Chem. Phys.* **2013**, *15*, 6608−6622.
(43) Dong, W.; Alizadeh, V.; Blasius, J.; Wylie, L.; Dick, L.; Fan, Z.; Kirchner, B. Locality in amino-acid based imidazolium ionic liquids. *Phys. Chem. Chem. Phys.* **2023**, *25*, 24678−24685.

https://doi.org/10.1021/acs.jpcb.4c02555
J. Phys. Chem. B 2024, 128, 6560−6566

SUPPORTING INFORMATION

Vibrational spectra simulations in amino-acid based imidazolium ionic liquids

Wenbo Dong,[a] Jan Blasius,[a] Zhijie Fan[b], Luke Wylier[a*]
[a]Mulliken Center for Theoretical Chemistry, University of Bonn, Beringstr. 4+6, D-53115 Bonn, Germany
[b] Department of Chemistry, Imperial College London, South Kensington Campus, London SW7 2AZ, United Kingdom
*email: wylie@thch.uni-bonn.de

Experimental Methodology

Material and Purification

Unless stated otherwise all materials were used as received without further purification. L-alanine (≥ 99.5%), L-phenylalanine (≥ 99.5%), L-proline (≥ 99.5%), L-histidine (≥ 99.5%), L-tyrosine (≥ 99.5%), L-tryptophan (≥ 99.5%), acetic acid (≥ 99.8%), silver nitrate (≥ 99%), 1-methyl imidazole (≥ 99%), bromoethane (≥ 98%) were purchased from Sigma-Aldrich. Amberlite IRN-78, OH^- form, ion-exchange resin (particle size = 25-30 mesh, 500-600 mm) was purchased from Acros Organics. Starting materials which have been stored over a long time need to purify before use. 1-ethyl imidazole (≥ 99.9%), which was purchased from Fluorochem, and 1-methyl imidazole were stirred over potassium hydroxide overnight, followed by distillation under vacuum. Bromoethane was extracted with concentrated sulfuric acid until the acid layer remained colourless. Then the organic layer was separated and neutralised with saturated sodium bicarbonate aqueous solution, followed by washing with deionised water. The resulting organic layer was dried with anhydrous magnesium sulphate overnight, followed by distillation under vacuum. Upon purification, all reagents were stored in the nitrogen atmosphere prior to reaction.

Equipment

Infrared (IR) spectra were recorded on a Perkin Elmer 1600 series FT-IR spectrometer.

Method

The ILs were synthesized by anion-exchange method.

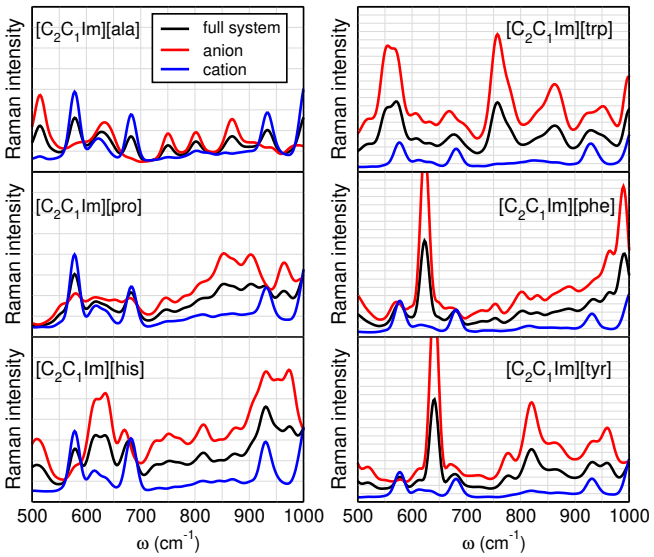

Figure S1: Part Raman for all systems as calculated theoretically using AIMD from 500 cm^{-} to 1000 cm^{-}. (The unit scale of the abscissa of left panel and right panel is: 5:2)

Table S1: Notable vibrational wavenumbers in the IR spectra of $[C_2C_1Im][pro]$. Comparison of experimental wavenumbers ω_{exp}/cm^{-1} and theoretical wavenumbers (Voronoi) ω_{the}/cm^{-1}

ω_{exp}/cm^{-1}	ω_{the}/cm^{-1} (IR)	ω_{the}/cm^{-1}(Raman)	Description
1171	1142		$C_{Im}H$ bend
1336	1317		$C_{pro}H_2$ bend
1379		1382	$C_{Et}H$ bend, $C_{Im}N$ stretch
		1461	$C_{Et}H$ bend
1450			water
1571	1545		C_{pro}=O stretch
3075	3090		=$C_{Im}H$ stretch

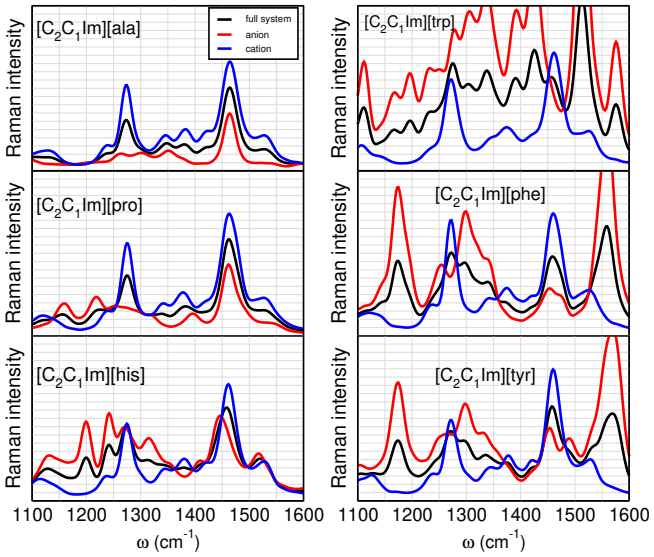

Figure S2: Part Raman for all systems as calculated theoretically using AIMD from 1100 cm^{-} to 1600 cm^{-}.

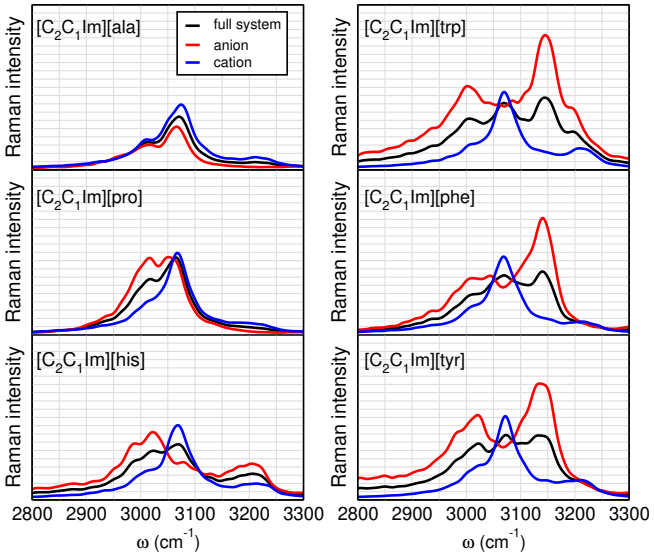

Figure S3: Part Raman for all systems as calculated theoretically using AIMD around 3000 cm^{-}.

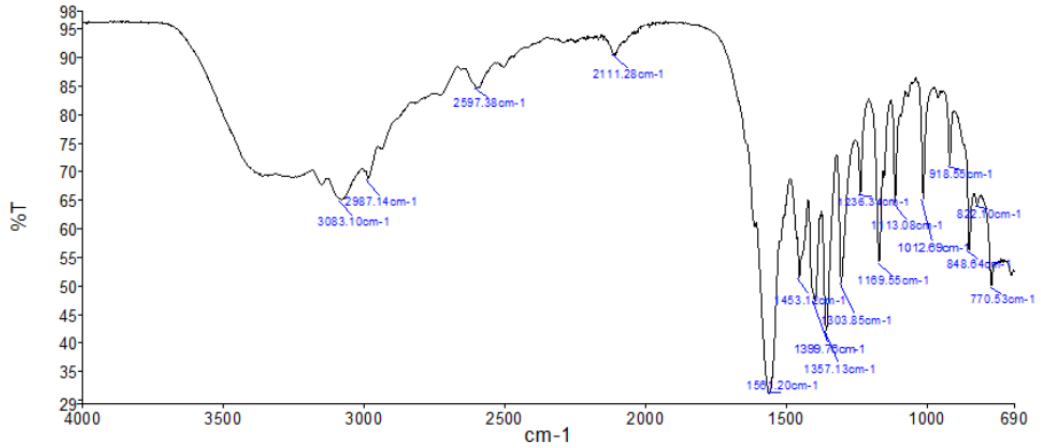

Figure S4: The experimental IR spectrum of [C_2C_1Im][ala].

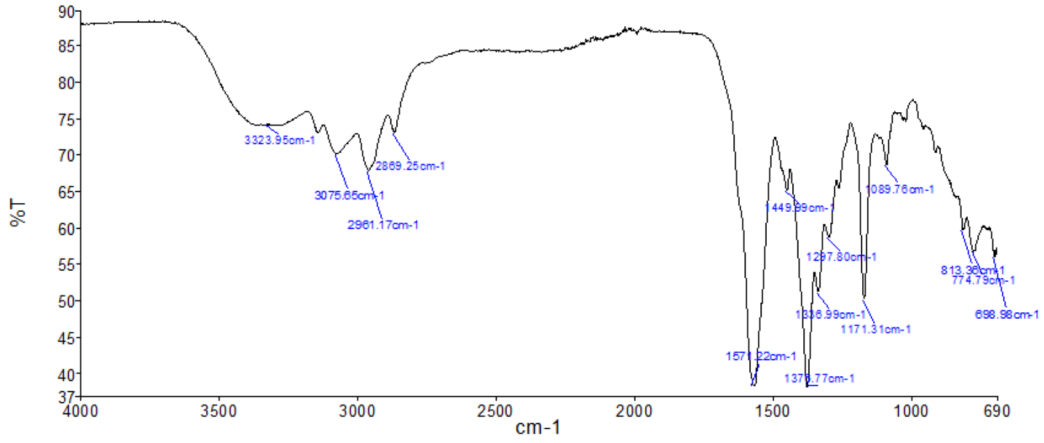

Figure S5: The experimental IR spectrum of [C_2C_1Im][pro].

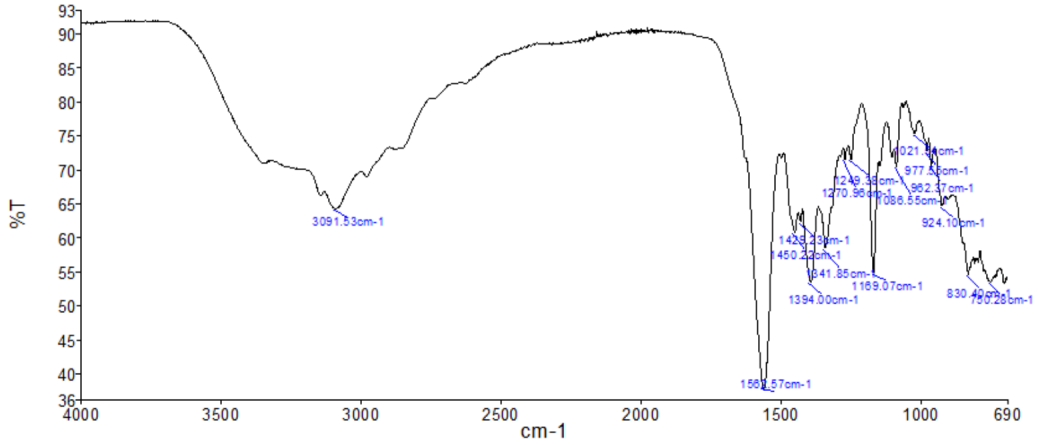

Figure S6: The experimental IR spectrum of $[C_2C_1Im][his]$.

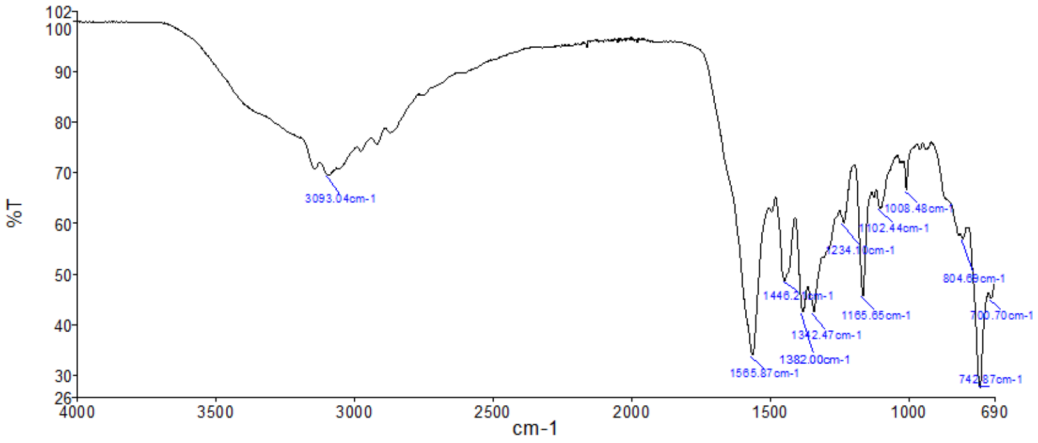

Figure S7: The experimental IR spectrum of $[C_2C_1Im][trp]$.

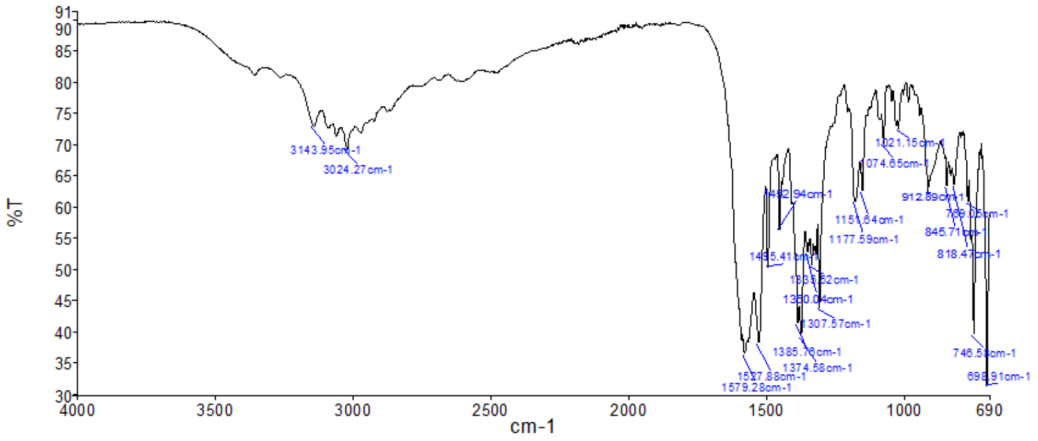

Figure S8: The experimental IR spectrum of $[C_2C_1Im][phe]$.

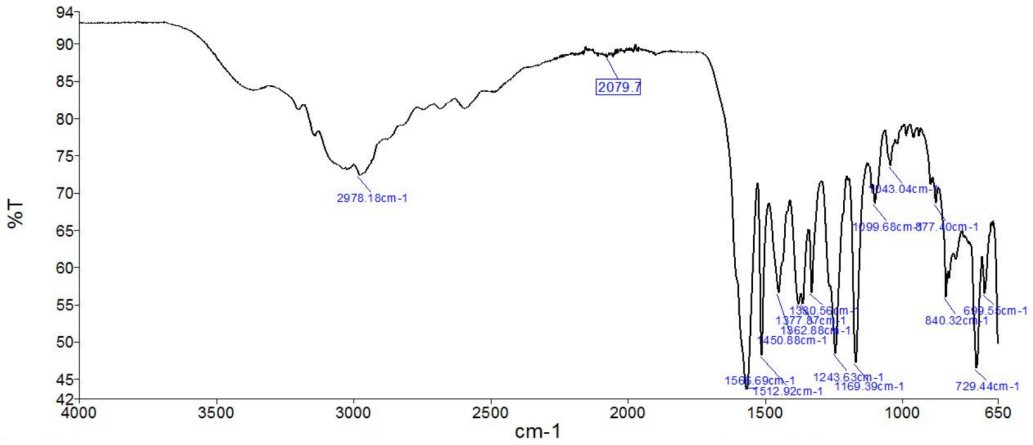

Figure S9: The experimental IR spectrum of $[C_2C_1Im][tyr]$.

Table S2: Notable vibrational wavenumbers in the IR spectra of $[C_2C_1Im][his]$. Comparison of experimental wavenumbers ω_{exp}/cm^{-1} and theoretical wavenumbers (Voronoi) ω_{the}/cm^{-1}

ω_{exp}/cm^{-1}	ω_{the}/cm^{-1} (IR)	ω_{the}/cm^{-1}(Raman)	Description
1169	1136		$C_{Im}H$ bend
1249			water
1342	1302		$C_{his}H_2$ bend
1394		1380	$C_{Et}H$ bend, $C_{Im}N$ stretch
1429		1457	$C_{Et}H$ bend
1568	1531		C_{his}=O stretch
3091	3074		=$C_{Im}H$ stretch

Table S3: Notable vibrational wavenumbers in the IR spectra of $[C_2C_1Im][trp]$. Comparison of experimental wavenumbers ω_{exp}/cm^{-1} and theoretical wavenumbers (Voronoi) ω_{the}/cm^{-1}

ω_{exp}/cm^{-1}	ω_{the}/cm^{-1} (IR)	ω_{the}/cm^{-1}(Raman)	Description
1165	1138		$C_{Im}H$ bend
1342	1294		$C_{trp}H_2$ bend
1382			$C_{Et}H$ bend, $C_{Im}N$ stretch
1446		1457	$C_{Et}H$ bend
1566	1535		C_{trp}=O stretch
3093	3082		=$C_{Im}H$ stretch

Table S4: Notable vibrational wavenumbers in the IR spectra of $[C_2C_1Im][phe]$. Comparison of experimental wavenumbers ω_{exp}/cm^{-1} and theoretical wavenumbers (Voronoi) ω_{the}/cm^{-1}

ω_{exp}/cm^{-1}	ω_{the}/cm^{-1} (IR)	ω_{the}/cm^{-1}(Raman)	Description
1178	1140		$C_{Im}H$ bend
1579	1537		C_{phe}=O stretch
3143	3086		=$C_{Im}H$ stretch

C. Aromatic-Aromatic Interactions and Hydrogen Bonding in Amino Acid Based Ionic Liquids

Wenbo Dong,* , Patrick R. Batista,* † Jan Blasius,* and Barbara Kirchner*

Received: 28 Jan 2025, First published: 31 Jan 2025.

Reproduced from Ref.

W. Dong, P. R. Batista, J. Blasius, B. Kirchner, *Phys. Chem. Chem. Phys.* **2025**, *27*, 4457-4466

doi:10.1039/D4CP04385E.

with permission from the Royal Society of Chemistry.‡

Contributions to the manuscript

- Development of the concept
- Performing all simulations, analysis, and calculations
- Interpretation of the results
- Writing of the manuscript

*Mulliken Center for Theoretical Chemistry, Clausius Institute for Physical and Theoretical Chemistry, University of Bonn, Beringstr. 4–6, 53115 Bonn, Germany

†Institute of Chemistry, University of Campinas, Monteiro Lobato, 270, Cidade Universitária, 13083-862, Campinas, São Paulo, Brazil.

PCCP

ROYAL SOCIETY OF CHEMISTRY

PAPER

View Article Online
View Journal

Cite this: DOI: 10.1039/d4cp04385e

Aromatic–aromatic interactions and hydrogen bonding in amino acid based ionic liquids†

Wenbo Dong,[a] Patrick R. Batista,[ab] Jan Blasius[a] and Barbara Kirchner *[a]

A series of six amino-acid-based imidazolium ionic liquids is computationally investigated using *ab initio* molecular dynamics. Radial pair and combined distribution functions are employed for the characterization and understanding of the interactions within these complex systems. The analyses reveal that the ionic liquids under investigation experience distinct cation–anion, cation–cation, and anion–anion interactions. It has been shown that cation–anion pairs interact predominantly through π–π interactions. Furthermore, hydrogen bonds are identified between distinct sites, with the interaction between the carboxylic acid group of the anion and the ring hydrogen atoms of the cation being the most dominant. The detailed analyses presented herein shed light on the complete spatial configuration of the investigated systems, as well as the interactions that are responsible for their structural stability. These interactions make ionic liquids particularly interesting as chiral solvents and reagents for the dissolution and stabilization of biomolecules.

Received 17th November 2024,
Accepted 28th January 2025

DOI: 10.1039/d4cp04385e

rsc.li/pccp

1 Introduction

Ionic liquids (ILs) are compounds which consist exclusively of ions and have a melting point below 100 °C.[1–5] The ability to design ILs with cations and anions that can meet the specific physical properties required for each application,[6] has made the study of ILs of considerable interest over the past three decades. Additionally, ILs can exhibit unique properties compared to standard solvents.[7] They can be involved in a variety of attractive interactions, including van der Waals,[8] dispersion forces,[9] as well as specific and anisotropic forces, such as hydrogen bonds (HB),[10] halogen bonding,[11] dipole–dipole[12] and magnetic dipole interactions.[13] One particularly interesting class of ILs is that based on amino acids (AA-ILs). The AA are chiral, having two chemically active centers suitable for modification, and possess strong hydrogen bonding ability. These features make AA-ILs more suitable as chiral solvents for the solubilization and stabilization of biomolecules in comparison to conventional ILs, which is very important in medicinal, synthetic, and pharmaceutical chemistry.[14–18]

Hardacre *et al.* have made outstanding contributions to both computational and experimental aspects of ILs, especially studying 1,3-dimethylimidazolium chloride by neutron diffraction, the structure of ILs and solute–solvent interactions and heat transfer in comparison.[19–21] In the context of molecular interaction investigation of the ILs, the -π interactions (*e.g.*, anion/cation/lone-pair-π and π–π interactions) play an important role on the structure stabilization.[22,23] For example, the study by Matthews *et al.* revealed the π–π interactions in imidazolium–chloride ILs through an analysis of energy diagrams of π^+–π^+ stacking structures, HB, and anion–π^+ interactions.[24] For the AA-ILs, both stacked and T-shaped structures are important for understanding the characteristics of the systems, since imidazolium ring constitutes the basic unit on most cations of ILs.[25] The results of π–π interactions analysis obtained using computational methods can help to elucidate the behavior and nature of the imidazolium cation–aromatic AA interaction.[25] The importance of HB interactions in pure ILs, mixtures of ionic liquids and cosolvents has been demonstrated by numerous experimental and theoretical studies.[26–29] In prior studies, AA have been selected due to the various functional groups present in AA side chains which can easily incorporate a wide range of properties such as chirality into ILs.[30] These AA-ILs were employed to investigate a series of properties, including dipole moment,[12] monopole–dipole electrostatic interaction and polarization, as well as spectroscopy[31,32] such as IR, Raman and power spectra. Furthermore, the properties of AA-ILs depend on the side groups of the amino acids involved. Typically, AA-ILs are composed of amino acids and some functional groups such as hydrogen bonding groups, charged groups or aromatic rings. Due to additional interactions between ions, some of its properties such as melting temperature or viscosity are affected by the molecular structure.[16]

[a] *Mulliken Center for Theoretical Chemistry, University of Bonn, Beringstr. 4 + 6 D-53115 Bonn, Germany. E-mail: kirchner@thch.uni-bonn.de*
[b] *Institute of Chemistry, University of Campinas, Cidade Universitária, Monteiro Lobato, 270, 13083-862, Campinas, São Paulo, Brazil*

† Electronic supplementary information (ESI) available: Electrostatic potential surface, CHELPG atomic charges, radial pair distribution functions and combined distribution functions analysis. See DOI: https://doi.org/10.1039/d4cp04385e

In order to address the physical and structural information related to the ILs, molecular dynamics (MD) simulations represents an appropriate tool.[33,34] It has previously been shown that theoretical prediction produced from simulation can accurately replicate experimentally obtained spectroscopy,[12,31] heats of vaporization and shear viscosities.[35] The study conducted by Hanke *et al.* showed that the crystal structure and liquid properties of the dimethylimidazolium chloride are influenced by the electrostatic and steric anisotropy of the structures.[36] Furthermore, combining experimental and theoretical methods, the study of ILs interactions within the ions and molecules of this ternary system has demonstrated the positive effect of [C_{16}mim][Br] on the electrolyte stability.[37] Thus, in the study presented herein, we focus on investigating the bulk structure and aromatic–aromatic interactions and HB through *ab initio* molecular dynamics (AIMD) simulations in different AA-ILs.

2 Systems investigated

In this study, we investigated six chiral AA-ILs containing the 1-ethyl-3-methylimidazolium ([C_2C_1im]$^+$) cation and a deprotonated AA as anionic counterpart, namely, L-alaninate ([ala]$^-$), L-prolinate ([pro]$^-$), L-histidinate ([his]$^-$), L-tryptophanate ([trp]$^-$), L-phenylalaninate ([phe]$^-$) and L-tyrosinate ([tyr]$^-$). The cation and amino acid anions employed are shown in Fig. 1. Each system is composed of 16 ions pairs, the sizes of the simulation boxes and the simulation times are summarized in Table 1. The cell size L is obtained from densities which were determined using classical MD in a prior study.[12] When comparing the densities from simulations and experiments,

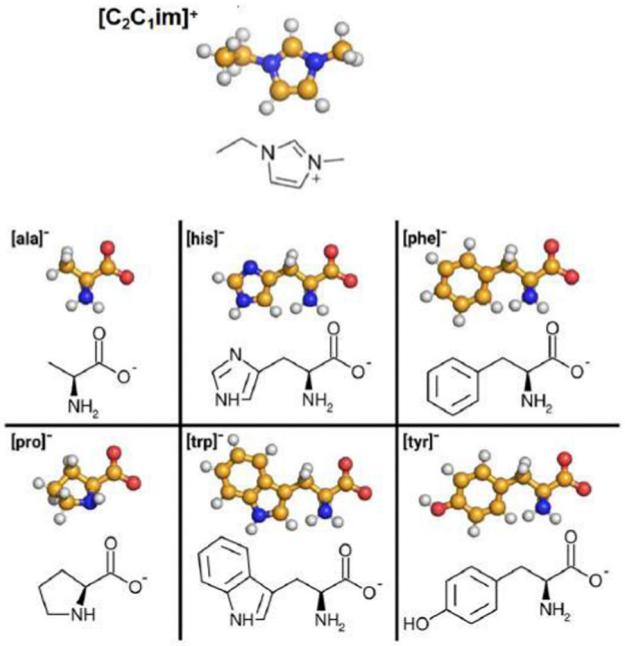

Fig. 1 Ball-and-stick images and Lewis structures of the imidazolium cation and the amino acid anions employed in the different ILs systems. The structural abbreviation is introduced in Section 2.

Table 1 System composition,[a] cell size L of the simulation boxes as well as densities from experiments ρ for the six systems investigated

System	L/Å	$\rho_{370\,K}$/g cm^{-3}	ρ^{exp}_{353K}/g cm^{-3}
[C_1C_2im][ala]	16.96	1.086	1.089
[C_1C_2im][pro]	17.66	1.070	1.109
[C_1C_2im][his]	18.65	1.064	
[C_1C_2im][trp]	19.70	1.093	
[C_1C_2im][phe]	18.89	1.089	
[C_1C_2im][tyr]	19.25	1.139	

[a] Each system is composed of 16 ion pairs.

deviations of the theoretically derived densities are small, with an error of 2,8% and 3.5%, respectively.[38] Besides, the densities decrease with higher temperatures.[38]

2.1 Computational details

The NPT ensemble was used to obtain equilibrium densities (Table 1). For each AA-IL system, a total equilibration step was performed over 10 ns using classical MD with a time step of 1 fs, a temperature of 370 K, a barostat applying 1 bar of pressure to the system, and 500 ion pairs.[39,40] These simulation boxes were equilibrated employing the CL&P force field parameters[41,42] and the LAMMPS software package.[43] Subsequently, AIMD simulations were conducted to take into account the polarization, which plays a role in the structure description of these ILs, as well as in their spectroscopy.[12]

The AIMD simulations consisted of an additional equilibration and a subsequent production run. Based on the cell dimensions shown in Table 1, simulation boxes containing 16 ion pairs were set up using PACKMOL.[44,45] The simulations were carried out based on the hybrid Gaussian and plane wave (GPW) method using the CP2K program package[46] and the QUICKSTEP[47] module implemented therein. The BLYP functional was employed with the corresponding BLYP Goedecker–Teter–Hutter pseudopotentials[48–50] together with the double-ζ basis set (MOLOPT-DZVP-SR-GTH).[51] Dispersion corrections were applied using the DFT-D3 scheme.[52,53] The convergence criterion for the SCF convergence was set to 10^{-5} and the density CUTOFF criterion was set to 280 Ry with a relative cutoff of 40 Ry and multigrids number 5 (NGRID 5). Both simulations runs were performed in the NVT ensemble using a timestep of 0.5 fs and a temperature of 370 K employing the Nosé–Hoover chain thermostat.[39,40] The equilibration run was performed for 10 ps (20 000 steps) employing massive thermostating of each atom using a thermostat coupling constant of 10 fs. The following production run was performed for 30 ps (60 000 steps) employing global thermostating and a thermostat coupling constant of 50 fs. All analyzes were performed with the open-source program TRAVIS,[54,55] which is available for download at **https://www.travis-analyzer.de**.

3 Results and discussion

3.1 Bulk structure

To evaluate the overall bulk phase structure of AA-ILs, radial pair distribution functions (RDFs) are evaluated and discussed. Fig. S9 (ESI†) shows the RDFs and the corresponding number

integrals (NIs) between the center of mass (CoM) of the amino acid anion and the ring center (CoR) of the imidazolium cation for each system investigated. In the case of $[C_2C_1im][ala]$ and $[C_2C_1im][pro]$, both anions show strong interactions with the cation and a distinct first solvation shell can be observed. Compared to $[ala]^-$ and $[pro]^-$, the four remaining anions show less pronounced solvation shells. Although all of them feature pair correlation functions with values greater than one, $[C_2C_1im]$-[his] is the only one showing a distinct peak which is located at 500 pm. However, this peak is less sharp compared to $[C_2C_1im][ala]$ and $[C_2C_1im][pro]$, and followed by a plateau up to around 700 pm. The remaining three AA-ILs, *i.e.*, $[C_2C_1im][trp]$, $[C_2C_1im][phe]$ and $[C_2C_1im][tyr]$, do not feature any pronounced peaks and rather show stretched plateaus with the $g(r)$ values for the RDFs being around 1.5, which implies that a local structure is somewhat ordered. However, the absence of distinct peaks indicates that no compact solvent shell can be observed when considering the CoM(an)–CoR(cat) RDFs, and the interactions favor generally weaker dispersion interactions than localized dipole interactions.

3.2 π−π interactions

Since $[his]^-$, $[trp]^-$, $[phe]^-$ and $[tyr]^-$ all feature aromatic ring systems, it is likely that interactions occur between these anions and the aromatic ring $[C_2C_1im]^+$. In order to investigate the potential occurrence of such interactions, Fig. 2 displays the RDFs and the corresponding NIs between the ring centers of the anions and cation.

In the case of $[C_2C_1im][pro]$, a broad plateau with values slightly above 1 is present in the CoR(an)–CoR(cat) RDF, which was expected since the $[pro]^-$ ring does not contain any π-electrons that could lead to aromatic–aromatic interactions with a cation. Conversely, the RDFs depicted in Fig. 2 for $[C_2C_1im][his]$, $[C_2C_1im][tyr]$, and $[C_2C_1im][phe]$ feature notable peaks, indicating the possible interaction between the aromatic π-systems of anions and cations. On the other hand, the $[C_2C_1im][tyr]$ does not show a distinct peak but rather a broadened plateau. This is likely due to the hydroxyl group of $[tyr]^-$, which makes it susceptible for additional HB as compared to the remaining aromatic amino acids and thus complicates the locality of interactions for this particular IL. Fig. 2 also shows that $[C_2C_1im][trp]$ exhibits a second peak with identical $g(r)$ values at 595 pm, corresponding to the phenyl ring, which composes part of the aromatic system. While the maximum distance for π–π-interactions has been proposed to be approximately 380 pm,[56] the distances observed herein are elongated by about 100 pm to 150 pm, potentially excluding the possibility of direct π–π-interactions between the aromatic anions and the cation. However, structure analyses of liquid benzene[57] and aromatic ionic liquids[58] have previously revealed that distances between aromatic rings which are greater than 500 pm play a substantial role in condensed phase structure. Additionally, several protein structure analyses have revealed that the presence of π-stacking interactions over larger distances can be relevant for the stabilization of certain protein structures.[59] In Fig. 3 the interactions between the amine group

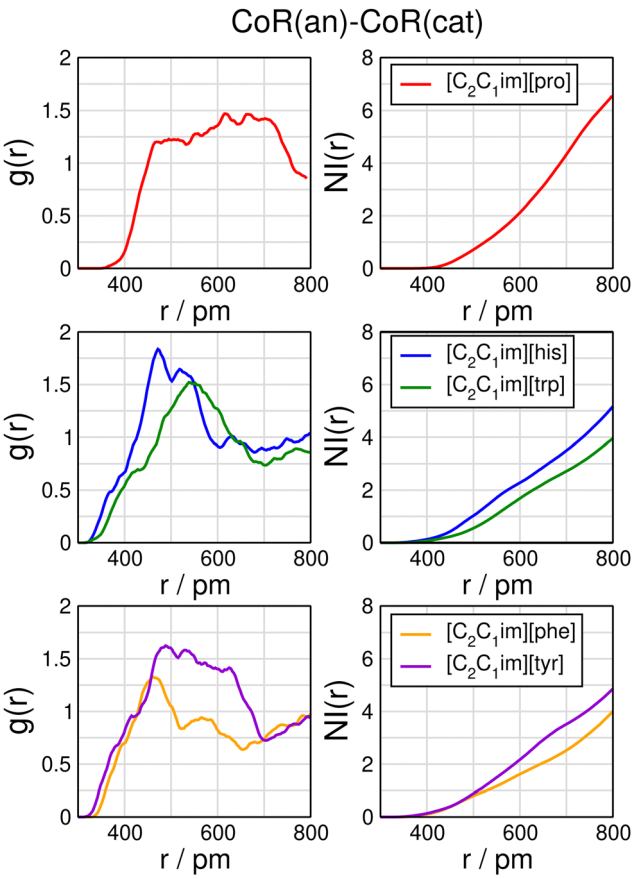

Fig. 2 Radial pair distribution functions (left) and number integrals (right) between the centers of ring of the anions and the centers of ring of the cation. Each line contains different liquids.

nitrogen atom of the anions and the π system of the cation are also shown. For each system, the distances at the first maxima are equal to 440 pm. Two distinct peaks can be observed especially in the $[C_2C_1im][ala]$, $[C_2C_1im][trp]$, $[C_2C_1im][phe]$ and $[C_2C_1im][tyr]$. When comparing the $[C_2C_1im][phe]$ and $[C_2C_1im][tyr]$, there is no substantial effect to N–H_2···π interaction for the hydroxyl group on the ring. For $[his]^-$ and $[trp]^-$, it was observed that nitrogen on the ring, which contains a hydrogen atom, does not play a significant role in the π–π interactions, as evidenced by the absence of a pronounced peak in the RDF in Fig. S10 (ESI†).

In order to investigate the orientation of the ring-to-ring interaction, Fig. 4 shows the combined distribution functions (CDFs) correlating the distance between the CoR of the anions and cation with the angle between the ring normal vector of the cation and the vector connecting the CoR of the anions and cation (see Fig. 4(b)).[58] This analysis allow us to ascertain whether the rings are preferably located: (i) on top of each other ($\alpha \approx 0^\circ$ or 180°); (ii) in a face-to-face or T-shaped conformation – an in-plane arrangement ($\alpha \approx 90^\circ$); (iii) T-shaped or a real in-plane conformation; (iv) parallel displaced orientation ($\alpha \approx 20^\circ$ or 160°). For the four aromatic amino acids investigated ($[C_2C_1im][his]$,$[C_2C_1im][trp]$, $[C_2C_1im]$-[phe] and $[C_2C_1im][tyr]$), it is seen that for distances around

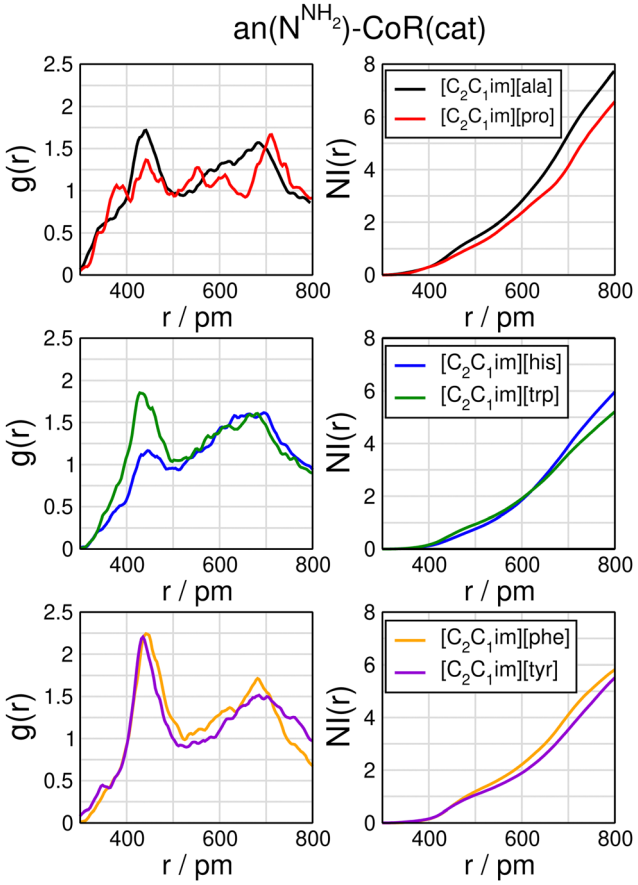

Fig. 3 Radial pair distribution functions (left) and number integrals (right) between the amine group nitrogen atoms of the anions and the centers of ring of the cation. Each line contains different liquids.

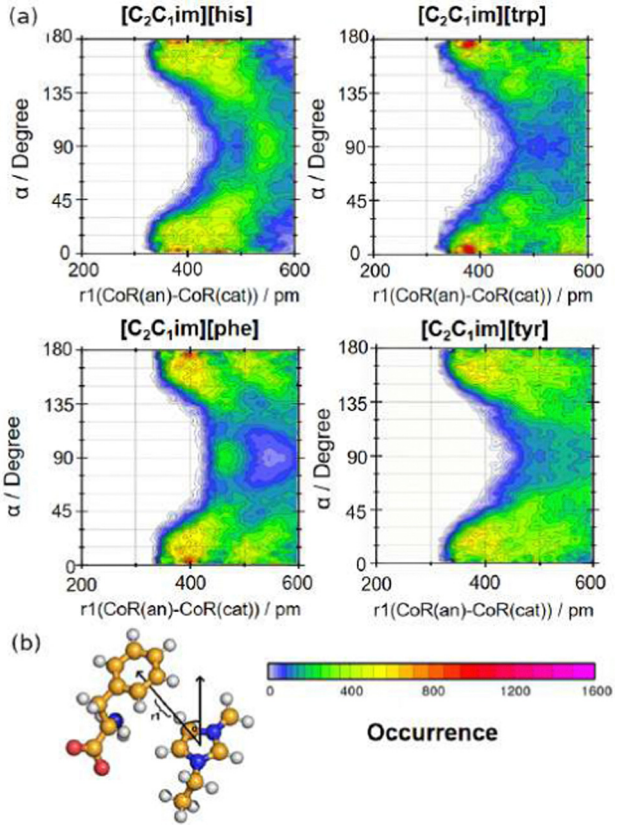

Fig. 4 (a) Combined distribution functions correlating the distance between the centers of ring of the anions and the centers of ring of the cation with the angle between the ring normal vector of the cation and the vector connecting the centers of ring of the cation and the centers of ring of the anions. (b) A representation of the interaction in a ball-and-stick model.

350 pm to 450 pm the cation and anion rings are almost exclusively located on π–π-interaction. However, although it seems that the four anions behave similarly with respect to their orientation around the cation, some differences can be observed upon closer examination. The strongest correlation is observed for [C_2C_1im][trp] at distances around 380 pm and angles close to 0° and 180°. Meanwhile, for [C_2C_1im][phe] the strongest signal is also observed for angles close to 0° and 180° and the distance between the ring centers is increased by 20 pm compared to [C_2C_1im][trp]. This suggests that for [C_2C_1im][trp] and [C_2C_1im][tyr], an on-top arrangement is the most preferred and predominant structural configuration. Similar to [C_2C_1im][trp] and [C_2C_1im][phe], [C_2C_1im][his] shows the strongest correlation around 0° and 180°. However, instead of only one maximum, two different maxima are observed, at a short distance of 380 pm and at a longer distance of 460 pm. This may be indicative of two distinct configurations in which the rings of $[his]^-$ and the cation are located on top of each other. Furthermore, the ring centers appear to be displaced, strongly suggesting a parallel displaced conformation. Therefore, it can be seen that all AA-ILs have a preference for 0°, 90°, and 180°. When the distance is shorter, 0° and 180° are preferred, while at longer distances 90° is preferred. Consequently, when the cation and the anion are close to each other, the π–π interaction is the predominant one.

To gain further insight into the orientation of anion and cation with respect to each other, Fig. S11 (ESI†) displays CDFs correlating the distance between the CoR of anion and cation with the angle between the ring normal vectors of both ions (see Fig. S11b, ESI†).[58] The combination of the analysis of Fig. 4 and Fig. S11 (ESI†) provides a better overview of the orientations of the aromatic anions with respect to the cations. Therefore, the results suggest that a minor proportion of T-shaped conformations are present and that the aromatic anions are preferably located on top of a cation. Additionally, in the case of [C_2C_1im][his] and [C_2C_1im][phe], some in-plane arrangements are also observed, although they play a minor role. In this case, indications for a small proportion of T-shaped conformations are also observed, with a stronger extent for [C_2C_1im][tyr] in comparison to the other three amino acid anions.

3.2.1 Cation–cation interaction. Fig. 5 shows RDFs between the ring centers of two cations. For the AA-ILs [C_2C_1im][ala], [C_2C_1im][pro], and [C_2C_1im][phe], the first peak is observed at distances of 380 pm, 350 pm and 374 pm, respectively. In the case of [C_2C_1im][his], the maximum of the first peak is observed at 400 pm. These distances are in agreement with previous studies of imidazolium-based ILs.[34,58] In contrast, no distinct

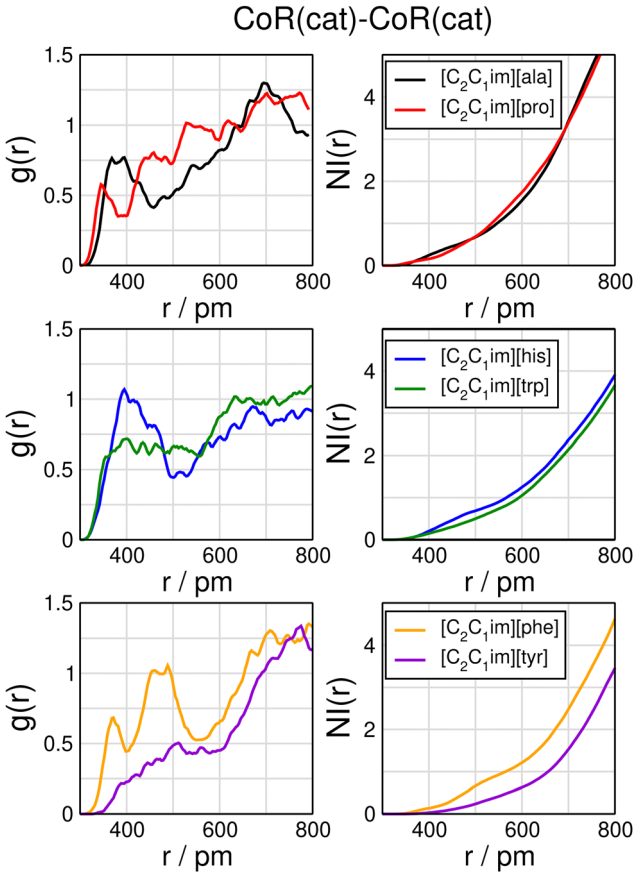

Fig. 5 Radial pair distribution functions (left) and number integrals (right) between the centers of ring of two cations. Each line contains different liquids.

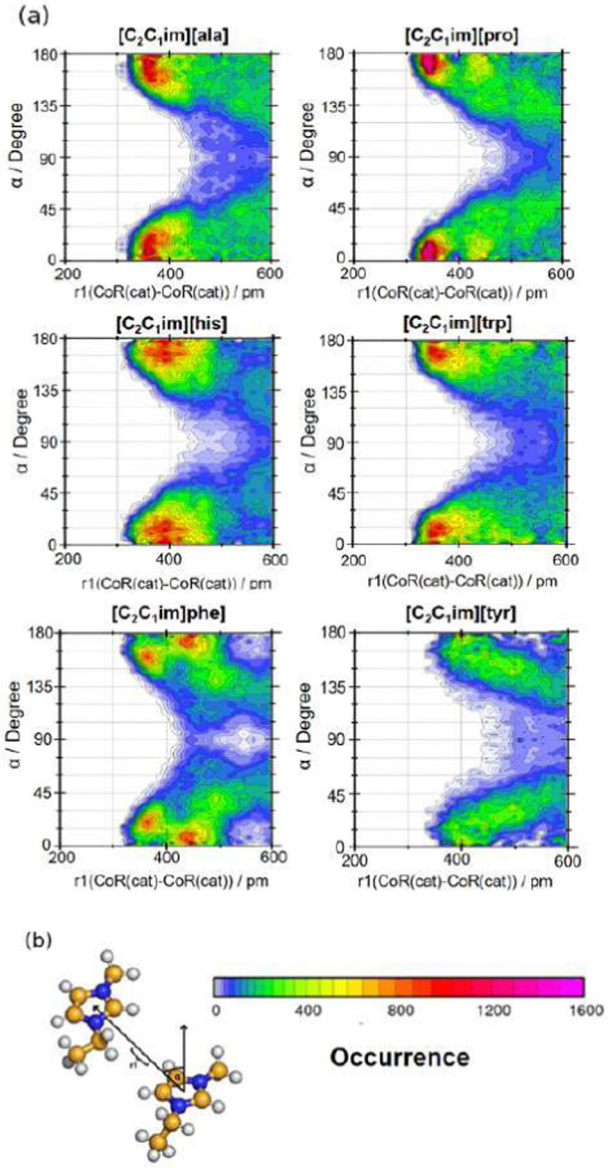

Fig. 6 (a) Combined distribution functions correlating the distance between the centers of ring of two cations with the angle between the ring normal vector of the reference cation and the vector connecting the centers of ring of both cations. (b) A representation of the interaction in a ball-and-stick model.

peaks are evident in the RDFs for [C_2C_1im][trp] and [C_2C_1im][tyr]. In comparison to the RDFs between cation and anion (Fig. 2 and Fig. S11, ESI†), the interaction between two cationic species is observed to occur at shorter distances. However, most of the peaks observed in Fig. 5 have values lower than one, indicating the presence of a weak local structure and a low probability of cation–cation interactions. This is further confirmed by the NIs of the corresponding RDFs, which only yield values of 1 at distances of approximately 550 pm to 650 pm.

Fig. 6 shows CDFs correlating the distance between the CoR of two cations with the angle between the ring normal of the reference cation and the vector connecting the ring centers of both cations (see Fig. 6(b)). The results for the AA-ILs [C_2C_1im][ala], [C_2C_1im][pro], [C_2C_1im][his] and [C_2C_1im][trp] are similar to those obtained for cation–anion interactions (Fig. 4). Thus, two cations are preferably located on top of each other, with α being between 0° and 30° or 150° and 180°, respectively. The wide angular distributions indicate a large proportion of parallel-displaced structures. In such conformations, the distances between the ring centers are predominantly around 350 pm, with [C_2C_1im][his] exhibiting a slightly larger value of approximately 400 pm. It is noteworthy that in the AA-ILs containing the non-aromatic anions, *i.e.*, [C_2C_1im][ala] and [C_2C_1im][pro], conformations with α between 0° and 150° are frequently observed. This indicates the occurrence of in-plane arrangements with larger distances between the ring centers, which may be a consequence of the interactions between amino group from anions and the π-system from the cation. In the case of [C_2C_1im][phe], multiple distinct maxima can be observed in Fig. 6. The first two maxima are located at a distance of approximately 370 pm and angles of α 20° and 160°, indicating a parallel-shifted arrangement of two cations. Two additional maxima are observed at a larger distance of approximately 440 pm with angles close to 0° and 180°, which correspond to structures in a face-to-face arrangement. Consequently, different arrangements take place in [C_2C_1im][phe] AA-IL. Furthermore, Fig. S12 (ESI†) displays CDFs correlating the distance between the ring centers of

two cations with the angle between the ring normal vectors of both ions. The results are similar to those shown in Fig. 6 for stacked arrangements. Thus, with the exception of [C_2C_1im][tyr], cation–cation interactions are observed.

3.2.2 Anion–anion orientation. To fully address the π−π interactions, the interaction between anions and their orientation towards each other was also considered. Based on the peaks with $g(r)$ values significantly greater than one shown in Fig. 7, it can be observed that pronounced interactions are present. The maximum peak at 570 pm and the NI value for [C_2C_1im][pro] suggest that approximately four other anions are present in $[pro]^-$ the first solvation shell. A similar solvation shell is noted for [C_2C_1im][phe], though the distance between the ring centers is 20 pm larger than in [C_2C_1im][pro]. For [C_2C_1im][his] and [C_2C_1im][trp], sharper peaks are observed at 528 pm and 595 pm, respectively. In the case of $[trp]^-$, a smaller peak around 400 pm may indicate interactions between two pyrrole rings. Meanwhile, the maximum at 595 pm, with an NI of approximately 3.0, suggests structures where the pyrrole ring of one $[trp]^-$ interacts with the benzene ring of another anion. On the other hand, the [C_2C_1im][tyr] does not show pronounced stacked interactions. A discrete peak is observed at approximately 633 pm, with a height of 1.14. Overall, the distances between the ring centers of two anions are notably longer than those observed between the cations and anions, which is expected to be due to electrostatic repulsion. Fig. 8 shows CDFs that highlight key differences in AA-ILs that contain aromatic anions. For [C_2C_1im][his], the angular distribution is almost uniform across all distances, indicating a significant presence of both on-top and in-plane arrangements. In contrast, [C_2C_1im][trp] displays a strong correlation at angles α close to 0° and 180° at a distance of approximately 345 pm, suggesting that many anions adopt a π−π stacking configuration. As distance increases, the angular distribution becomes more uniform, with in-plane arrangements becoming more predominant. A particularly interesting CDF is observed for [C_2C_1im][phe], which exhibits a strong preference for π–π stacking around 500 pm. Structurally, this represents intermediate orientations between on-top and in-plane arrangements. Similar to [C_2C_1im][trp], [C_2C_1im][tyr] also shows strong correlations at α angles near 0° and 180°. However, at greater distances, π–π stacking becomes less frequent, and the angular distribution becomes more dominant with angles between 35° and 135°. Fig. S13 (ESI†) shows CDFs correlating the angle between the ring

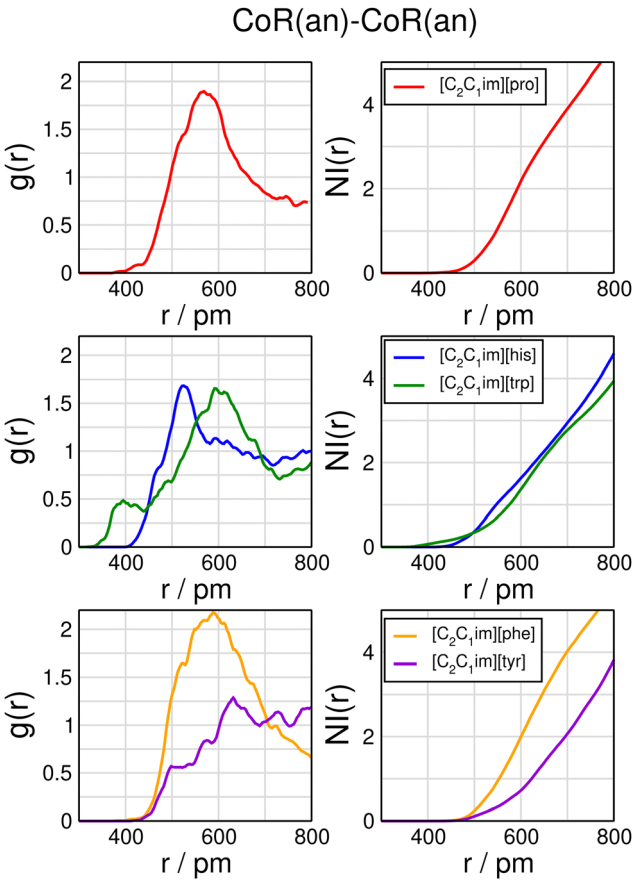

Fig. 7 Radial pair distribution functions (left) and number integrals (right) between the centers of ring of two anions. Each line contains different liquids.

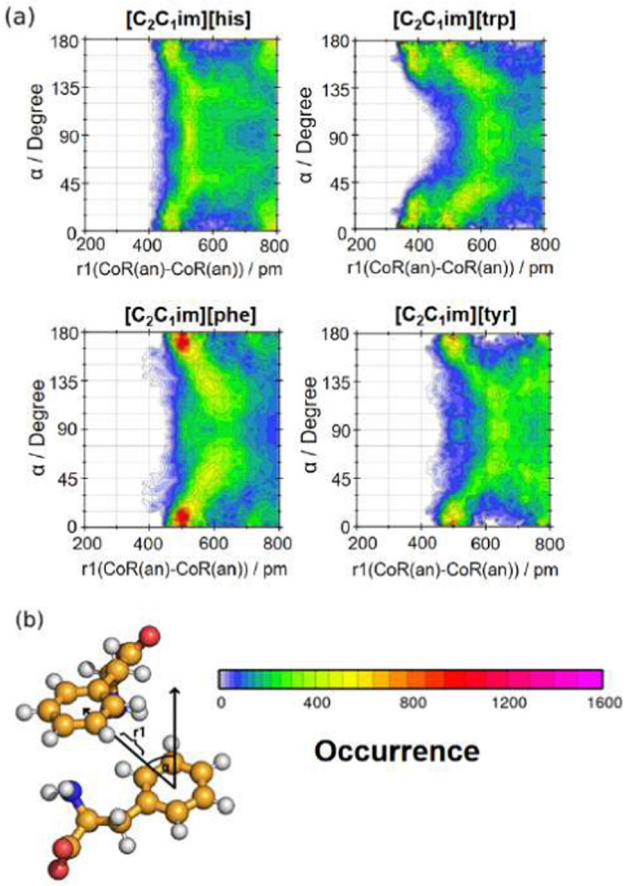

Fig. 8 (a) Combined distribution functions correlating the distance between the centers of ring of two anions with the angle between the ring normal vector of the reference anions and the vector connecting the centers of ring of both anions. (b) A representation of the interaction in a ball-and-stick model.

planes of two approaching anions in dependence on their distance to conclude about the absolute orientations. $[C_2C_1im][his]$ and $[C_2C_1im][phe]$ show a broad angular distribution, whereas in the case of $[C_2C_1im][his]$ angles α around 15° and 165° seem to be slightly preferred. Combined with the information gained from Fig. 7, some amount of stacked conformations can be observed for the histidinate anions. However, there seems to be no distinct dominance of such arrangements, as a large proportion of T-shaped and in-plane alignments also occur. The aforementioned results align with the ESP surfaces in Fig. S1 (ESI†), which show that $[his]^-$ and $[trp]^-$ exhibit charge extremes within the heterocycle. Additionally, the six-membered ring of $[trp]^-$ has lower electron density, indicating that neutral rings (green colored) favor π–π stacking. Additionally, the weaker interaction observed between [tyr]- anions compared to $[phe]^-$ can be attributed to the presence of the alcohol group in the former, which likely increases the probability of HB formation between the hydroxyl and carboxylate groups, thereby reducing the π–π stacking.

3.3 Hydrogen bond Interactions

The cation and anions possess multiple and different HB donor and acceptor sites,[60] thus allowing for a complex interaction network which, in turn, can play a role on the stabilization of these species. Therefore, it is very important to understand the HB topology and the competition for donor/acceptor positions in the investigated AA-ILs. The hydrogen atoms of the cation's ring are the most prominent donor sites, while the hydrogen atom bonded to the carbon atom that is bonded to the two nitrogen atoms is the most acidic. A straightforward estimation of the strength of a HB can be obtained from the distance and height of the first maximum in the X···H RDF along with their NI. This provides the average number of HBs formed by atom X. However, to reduce the number of RDF plots, an effective approach to represent such data is based on Sankey diagrams.[61] These diagrams (built by TRAVIS[54,55]) depict the entire HB topology in a flowchart format, which is particularly useful for visualizing pairwise RDFs written as a matrix of numbers. The matrix is structured so that its rows represent all the unique HB acceptors in the system, while its columns correspond to the HB donors. Then, a RDF is calculated for each donor–acceptor pair. When a hydrogen bond is detected, the element is colored based on a color scale that reflects the strength of the bond, which is determined by the distance and height of the RDF's first maximum. (see ref. 55 for more details).

The Sankey diagrams for all systems are presented in Fig. 9 (the labels of the donor and acceptor HB sites are indicated in the caption). HB donors are on the left side and HB acceptors on the right side. The numbers correspond to the total hydrogen bond count of the donors or acceptors. The width of the bar is proportional to the number of HBs between the two interacting atoms. It is important to note that the number of HB differs between the two sides because of the variation in the number of molecules involved in the interaction. In all AA-ILs the main acceptor of HB is $an(O^{CO_2})$, being the most pronounced interaction that occurs between $an(O^{CO_2})$ and $cat(H^{ring})$. Interestingly, the RDF shape for these interactions (see Fig. S14–S16 in the ESI†) is quite similar, with the maximum of the first peaks located around 210 pm (see Table S8 in the ESI†), regardless of the amino acid anion. This indicates that this HB is only minimally affected by amino acid residues. The second strong HB acceptor site of the amino acid anions is the $an(N^{NH_2})$ with HB numbers ranging from 1.49 in the $[C_2C_1im][trp]$ until 2.40 in the $[C_2C_1im][ala]$. Based on the RDF values presented in Table S8 (ESI†), $[C_2C_1im][ala]$, $[C_2C_1im][trp]$, $[C_2C_1im][phe]$ and $[C_2C_1im][tyr]$ show a distinct peak located at around 230 pm, indicating a HB of similar length for these AA-ILs. As expected, the pyrrole-like nitrogen, $an(N^{NH})$, in $[C_2C_1im][his]$ and $[C_2C_1im][trp]$ is a weak HB acceptor, given that its lone pair is embedded within the π-system. Consequently, the $an(H^{NH})$ is a better HB donor in $[C_2C_1im][his]$, however, in the case of $[C_2C_1im][trp]$, this HB interaction is more hindered due to the presence of the adjacent six-membered ring. On the other hand, in $[pro]^-$, where the ring is not aromatic, the nitrogen lone pair is more accessible for the formation of an HB and the $an(H^{NH})$ behaves as a weaker HB donor. For the interaction between the $cat(H^{ring})$ and the pyridine-like nitrogen atom of $[his]^-$, a HB can be observed at a distance of 232 pm (see the Fig. S17 and S18 in the ESI†).

In contrast to the other ILs, the $[C_2C_1im][tyr]$ features a unique HB site, that is, a hydroxyl group that plays a significant role in the HB network, where the $an(O^{alc})$ atom receives 2.38 HBs on average. The most predominant interactions occur with acidic ring protons of the cation, $cat(H^{ring})$, and with the hydroxyl hydrogen atom, $an(H^{alc})$, of another $[tyr]^-$ anion. A HB between $cat(H^{ring})$ and $an(O^{alc})$ is observed to have an equilibrium distance of 243 pm, as showed in Fig. S19 in the ESI.† For this interaction, the maximum at the first peak and thus the HB distance is found to be 166 pm, indicating a strong HB. However, the corresponding peak shows significantly decreased intensity in comparison to the interaction between $an(H^{alc})$ and $an(O^{CO_2})$. A similar structure has been observed for neutral [tyr] dimers[62,63] where a HB between the two hydroxyl groups was observed. In agreement with earlier observations based on Fig. S19 (ESI†), $an(N^{NH_2})$ only acts as a weak HB acceptor from the $an(H^{alc})$. Nevertheless, the HB is more favorable with $an(O^{CO_2})$. The HB interaction features are closely associated with the ESP in Fig. S1 (ESI†), as the strongest interactions take place between sites with higher positive and negative charges. Furthermore, in all systems the remaining sites referred to as $an(H^{NH})$, $cat(H^{CH_n})$, $an(H^{CH_2})$, $an(H^{CH_3})$, $an(C^{ring})$, and $cat(N^{ring})$, collectively contribute to the HB network, although each site has an HB number close to or less than 1.

Physical properties are related to the structural formation of ILs. If we assume that HB strengthens the structure of ILs, it will lead to a behavior similar to that of molecular liquids.[20,64,65] HB has a significant influence on the structure and properties of ILs, as evidenced by their melting point, viscosity and enthalpy of vaporization.[6] The surface polarization can significantly weaken HB in ILs. In addition, the analysis of the bond length, bond angle and bond energy of HB in two-dimensional surface ILs also shows that surface polarization can weaken HB.[66] Local and directional interactions by HB lead to the formation of ion pairs, which in turn manifest as reduced melting points and decreased viscosities.[67]

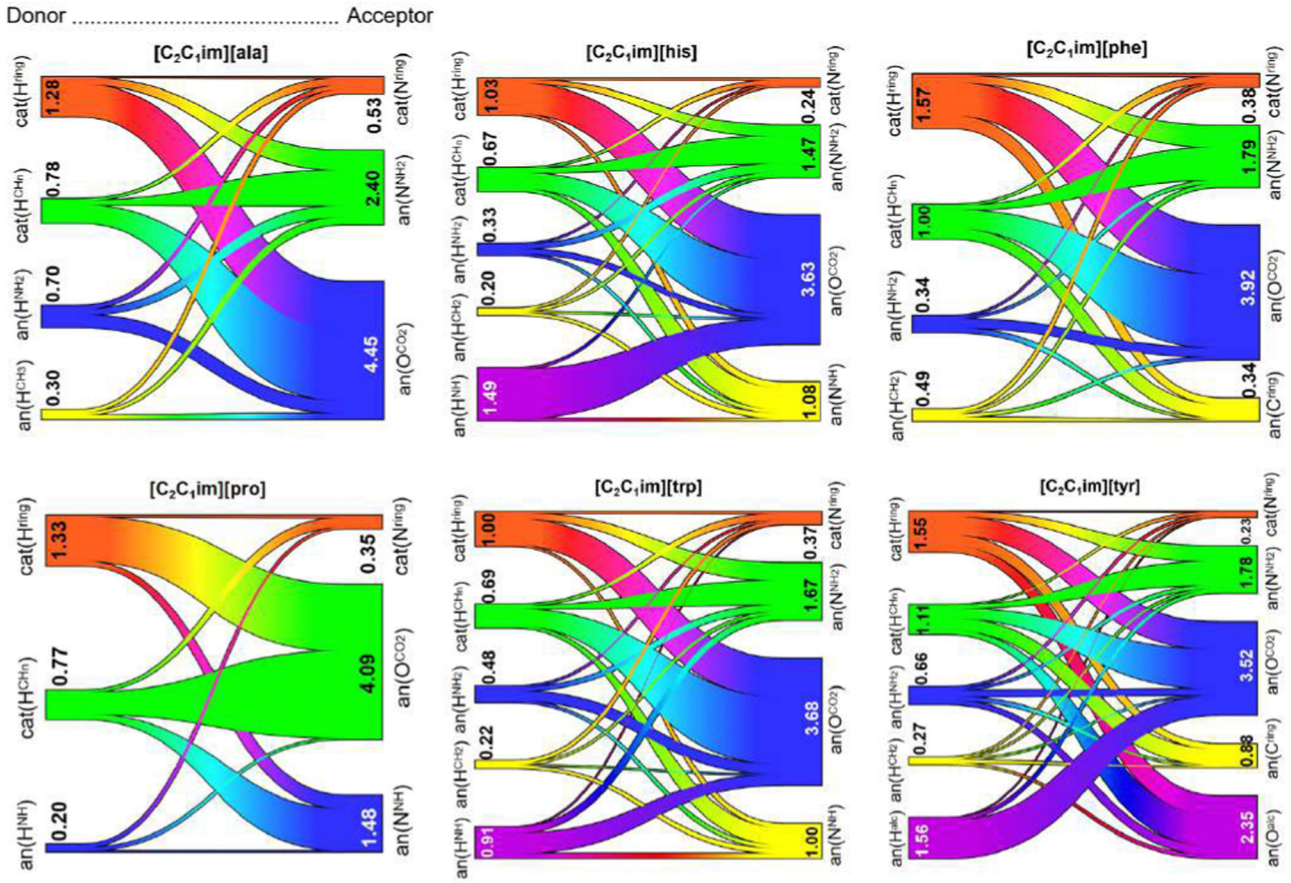

Fig. 9 Linear Sankey diagrams showing the HB topology derived from the pairwise RDF, represented as a matrix of numerical values for all AA-ILs under investigation. The labels in the diagram correspond to the following HB donor and acceptor sites: cat(H^{ring}) are the hydrogen atoms in the $[C_2C_1im]^+$ ring; cat(H^{CHn}) are the hydrogen atoms in the CHn groups of the $[C_2C_1im]^+$; cat(N^{ing}) is the nitrogen atom in the ring of $[C_2C_1im]^+$ cation; an(H^{NH_2}) (except $[C_2C_1im][pro]$) are the hydrogen atoms in NH_2 group of the anions; an(N^{NH_2}) (except $[C_2C_1im][pro]$) is the nitrogen atom in NH_2 group of the anions; an(H^{CH_2}) (except $[C_2C_1im][ala]$ and $[C_2C_1im][pro]$) are the hydrogen atoms in the chain of the anions; an(O^{CO_2}) are the oxygens in carboxyl group of the anions. For $[C_2C_1im][ala]$, an(H^{CH_3}) are the hydrogen atoms in CH_3 groups of $[ala]^-$. For $[C_2C_1im][pro]$, $[C_2C_1im][his]$, and $[C_2C_1im][trp]$, an(H^{NH}) is the hydrogen atom in NH group of the anion ring; an(N^{NH}) is the nitrogen atom in NH group of the anion ring. For $[C_2C_1im][phe]$ and $[C_2C_1im][tyr]$, an(C^{ring}) are the carbon atom in the anion ring. For $[C_2C_1im][tyr]$, an(H^{alc}) is the hydrogen atom in hydroxyl group of $[tyr]^-$; an(O^{alc}) is the oxygen atom in hydroxyl group of $[tyr]^-$. The HB donor and acceptor sites are colored in a red-green-blue color scale.

4 Conclusion

Herein, the aromatic–aromatic interactions and HB in AA-ILs were systematically investigated. For aromatic–aromatic interactions, cation–anion orientations predominantly adopt a stacked conformation (π–π interaction) across all aromatic amino acid anion–cation pairs. Among the systems examined, short-range cation–cation interactions were found to be weak. This likely results from strong cation–anion interactions, which suppress direct interactions between cations. In the case of anion–anion interactions, $[C_2C_1im][phe]$ exhibits a strong preference for π–π stacking at distances around 500 pm, as revealed by combined CDF analysis of interaction angles and distances. Conversely, in $[C_2C_1im][tyr]$, there is a tendency for in-plane alignment as the distance between anions increases. Additionally, hydrogen bonding in AA-ILs occurs primarily between the carboxylate group of the anion and the aromatic hydrogen atoms of the cation. Through these studies, the strength and tendency of the molecular interactions of AA-ILs were further revealed.

Data availability

The data supporting this article have been included as part of the ESI.† The ESI† includes electrostatic potential surface, CHELPG atomic charges, radial pair distribution functions and combined distribution functions analysis.

Conflicts of interest

There are no conflicts to declare.

Acknowledgements

The authors thank the DFG under the grant project number 406232243, the China Scholarship Council (CSC) and IMPRS-RCHARGE. This study was financed, in part, by the São Paulo Research Foundation (FAPESP), Brazil. P. R. B. would like to thank FAPESP Process Numbers #2020/10246-0, #2021/09687-5,

and #2023/00531-8; the National Laboratory for Scientific Computing (LNCC/MCTI, Brazil, SDumont supercomputer) for providing computational HPC resources. The authors gratefully acknowledges the support provided by the High Performance Computing & Analytics Lab of the University of Bonn.

Notes and references

1 M. Freemantle, *An introduction to ionic liquids*, Royal Society of Chemistry, 2010.
2 B. Kirchner and O. Hollóczki, *et al.*, *Wiley Interdiscip. Rev.: Comput. Mol. Sci.*, 2015, **5**, 202–214.
3 O. Hollóczki and F. Malberg, *et al.*, *Phys. Chem. Chem. Phys.*, 2014, **16**, 16880–16890.
4 F. Malberg and O. Hollóczki, *et al.*, *Struct. Chem.*, 2015, **26**, 1343–1349.
5 Z. Lei, B. Chen, Y.-M. Koo and D. R. MacFarlane, *Introduction: ionic liquids*, 2017.
6 S. A. Forsyth, J. M. Pringle and D. R. MacFarlane, *Aust. J. Chem.*, 2004, **57**, 113–119.
7 R. Hayes, G. G. Warr and R. Atkin, *Chem. Rev.*, 2015, **115**, 6357–6426.
8 V. A. Parsegian, *van der Waals forces: a handbook for biologists, chemists, engineers, and physicists*, Cambridge University Press, 2005.
9 F. Kohler, *Ber. Bunsenges. Phys. Chem.*, 1977, **81**, 775.
10 G. A. Jeffrey and G. A. Jeffrey, *An introduction to hydrogen bonding*, Oxford university press, New York, 1997, vol. 12.
11 P. Metrangolo and G. Resnati, *Halogen bonding: fundamentals and applications*, Springer, 2008, vol. 126.
12 W. Dong, V. Alizadeh, J. Blasius, L. Wylie, L. Dick, Z. Fan and B. Kirchner, *Phys. Chem. Chem. Phys.*, 2023, **25**, 24678–24685.
13 A. Daneshvar, M. Moosavi and H. Sabzyan, *Phys. Chem. Chem. Phys.*, 2020, **22**, 13070–13083.
14 N. Rohman, N. N. Dass and S. Mahiuddin, *J. Chem. Eng. Data*, 1999, **44**, 465–472.
15 R. Abraham, M. Abdulkhadar and C. Asokan, *J. Chem. Thermodyn.*, 2000, **32**, 1–16.
16 H. Ohno and K. Fukumoto, *Acc. Chem. Res.*, 2007, **40**, 1122–1129.
17 P. Ossowicz, J. Klebeko, B. Roman, E. Janus and Z. Rozwadowski, *Molecules*, 2019, **24**, 3252.
18 G.-h Tao, L. He, W.-s Liu, L. Xu, W. Xiong, T. Wang and Y. Kou, *Green Chem.*, 2006, **8**, 639–646.
19 C. Hardacre, J. D. Holbrey, S. J. McMath, D. T. Bowron and A. K. Soper, *J. Chem. Phys.*, 2003, **118**, 273–278.
20 C. Hardacre, J. D. Holbrey, M. Nieuwenhuyzen and T. G. Youngs, *Acc. Chem. Res.*, 2007, **40**, 1146–1155.
21 C. Nieto de Castro, M. Lourenço, A. Ribeiro, E. Langa, S. Vieira, P. Goodrich and C. Hardacre, *J. Chem. Eng. Data*, 2010, **55**, 653–661.
22 P. Kadlubanski, K. Calderon-Mojica, W. A. Rodriguez, D. Majumdar, S. Roszak and J. Leszczynski, *J. Phys. Chem. A*, 2013, **117**, 7989–8000.
23 S. S. Rao and S. P. Gejji, *J. Phys. Chem. A*, 2016, **120**, 5665–5684.
24 R. P. Matthews, T. Welton and P. A. Hunt, *Phys. Chem. Chem. Phys.*, 2015, **17**, 14437–14453.
25 A. A. Rodrguez-Sanz, E. M. Cabaleiro-Lago and J. Rodrguez-Otero, *Org. Biomol. Chem.*, 2015, **13**, 7961–7972.
26 K. Fumino, A. Wulf and R. Ludwig, *Phys. Chem. Chem. Phys.*, 2009, **11**, 8790–8794.
27 L. Cammarata, S. Kazarian, P. Salter and T. Welton, *Phys. Chem. Chem. Phys.*, 2001, **3**, 5192–5200.
28 T. Gao, J. M. Andino and J. R. Alvarez-Idaboy, *Phys. Chem. Chem. Phys.*, 2010, **12**, 9830–9838.
29 T. Seki, J.-D. Grunwaldt and A. Baiker, *J. Phys. Chem. B*, 2009, **113**, 114–122.
30 S. Kirchhecker and D. Esposito, *Curr. Opin. Green Sustainable Chem.*, 2016, **2**, 28–33.
31 W. Dong, J. Blasius, Z. Fan and L. Wylie, *J. Phys. Chem. B*, 2024, **128**, 6560–6566.
32 K. Wendler, M. Brehm, F. Malberg, B. Kirchner and L. Delle Site, *J. Chem. Theory Comput.*, 2012, **8**, 1570–1579.
33 H. Weingärtner, *Angew. Chem., Int. Ed.*, 2008, **47**, 654–670.
34 P. Hunt, *Mol. Simul.*, 2006, **32**, 1–10.
35 T. Köddermann, D. Paschek and R. Ludwig, *ChemPhysChem*, 2007, **8**, 2464–2470.
36 C. Hanke, S. Price and R. Lynden-Bell, *Mol. Phys.*, 2001, **99**, 801–809.
37 T. C. Lourenço, L. M. Barros, C. G. Anchieta, T. C. Nepel, J. P. Júlio, L. G. Dias, R. Maciel Filho, G. Doubek and J. L. Da Silva, *J. Mater. Chem. A*, 2023, **11**, 7780–7782.
38 A. S. Gouveia, L. C. Tome and I. M. Marrucho, *J. Chem. Eng. Data*, 2016, **61**, 83–93.
39 S. Nosé, *J. Chem. Phys.*, 1984, **81**, 511–519.
40 W. G. Hoover, *Phys. Rev. A: At., Mol., Opt. Phys.*, 1985, **31**, 1695.
41 J. N. Canongia Lopes, J. Deschamps and A. A. Pádua, *J. Phys. Chem. B*, 2004, **108**, 2038–2047.
42 J. N. Canongia Lopes and A. A. Pádua, *J. Phys. Chem. B*, 2006, **110**, 19586–19592.
43 S. Plimpton, *J. Comput. Phys.*, 1995, **117**, 1–19.
44 J. M. Martnez and L. Martnez, *J. Comput. Chem.*, 2003, **24**, 819–825.
45 L. Martnez, R. Andrade, E. G. Birgin and J. M. Martnez, *J. Comput. Chem.*, 2009, **30**, 2157–2164.
46 T. D. Kühne, M. Iannuzzi, M. Del Ben, V. V. Rybkin, P. Seewald, F. Stein, T. Laino, R. Z. Khaliullin, O. Schütt and F. Schiffmann, *et al.*, *J. Chem. Phys.*, 2020, **152**, 19.
47 J. VandeVondele, M. Krack, F. Mohamed, M. Parrinello, T. Chassaing and J. Hutter, *Comput. Phys. Commun.*, 2005, **167**, 103–128.
48 S. Goedecker, M. Teter and J. Hutter, *Phys. Rev. B: Condens. Matter Mater. Phys.*, 1996, **54**, 1703.
49 C. Hartwigsen, S. Gœdecker and J. Hutter, *Phys. Rev. B: Condens. Matter Mater. Phys.*, 1998, **58**, 3641.
50 M. Krack, *Theor. Chem. Acc.*, 2005, **114**, 145–152.
51 J. VandeVondele and J. Hutter, *J. Chem. Phys.*, 2007, **127**, 114105.
52 S. Grimme, J. Antony, S. Ehrlich and H. Krieg, *J. Chem. Phys.*, 2010, **132**, 154104.

53 S. Grimme, S. Ehrlich and L. Goerigk, *J. Comput. Chem.*, 2011, **32**, 1456–1465.
54 M. Brehm and B. Kirchner, *J. Chem. Inf. Model.*, 2011, **51**, 2007–2023.
55 M. Brehm, M. Thomas, S. Gehrke and B. Kirchner, *J. Chem. Phys.*, 2020, **152**, 164105.
56 C. Janiak, *J. Chem. Soc., Dalton Trans.*, 2000, 3885–3896.
57 T. F. Headen, C. A. Howard, N. T. Skipper, M. A. Wilkinson, D. T. Bowron and A. K. Soper, *J. Am. Chem. Soc.*, 2010, **132**, 5735–5742.
58 M. Brehm, H. Weber, A. S. Pensado, A. Stark and B. Kirchner, *Z. Phys. Chem.*, 2013, **227**, 177–204.
59 G. B. McGaughey, M. Gagné and A. K. Rappé, *J. Biol. Chem.*, 1998, **273**, 15458–15463.
60 S. J. Grabowski, *Chem. Commun.*, 2024, **60**, 6239–6255.
61 A. B. Kennedy and H. R. Sankey, *Minutes of the Proceedings of the Institution of Civil Engineers*, 1898, pp. 278–312.
62 R. Chelli, F. L. Gervasio, P. Procacci and V. Schettino, *J. Am. Chem. Soc.*, 2002, **124**, 6133–6143.
63 F. L. Gervasio, R. Chelli, P. Procacci and V. Schettino, *Proteins: Struct., Funct., Genet.*, 2002, **48**, 117–125.
64 P. Suarez, S. Einloft, J. Dullius, R. De Souza and J. Dupont, *J. Chim. Phys. Phys.-Chim. Biol.*, 1998, **95**, 1626–1639.
65 A. Mele, C. D. Tran and S. H. De Paoli Lacerda, *Angew. Chem., Int. Ed.*, 2003, **42**, 4364–4366.
66 K. Dong, S. Zhang and Q. Wang, *Sci. China: Chem.*, 2015, **58**, 495–500.
67 K. Fumino, T. Peppel, M. Geppert-Rybczyńska, D. H. Zaitsau, J. K. Lehmann, S. P. Verevkin, M. Köckerling and R. Ludwig, *Phys. Chem. Chem. Phys.*, 2011, **13**, 14064–14075.

SUPPORTING INFORMATION

Aromatic-aromatic interactions and hydrogen bonding in amino acid based ionic liquids

Wenbo Dong,[a] Patrick R. Batista,[a,b] Jan Blasius[a], Barbara Kirchner[a*]
[a]Mulliken Center for Theoretical Chemistry, University of Bonn, Beringstr. 4+6, D-53115 Bonn, Germany
[b]Institute of Chemistry, University of Campinas, Monteiro Lobato, 270, Cidade Universitária, 13083-862, Campinas, São Paulo, Brazil
*email:kirchner@thch.uni-bonn.de

S1 Electrostatic Potential Surface and CHELPG Atomic Charges

S1.1 Static Quantum Chemical Calculations

Quantum chemical calculations were carried out in order to obtain the electrostatic potentials (ESPs) of the amino acid anions. Therefore, geometry optimizations and frequency calculations were performed with the Orca[1] software package employing the PBEh-3c[2] composite method, which was paired with a modified def2-SV(P) basis set, termed as def2-mSVP. This level of theory includes the DFT-D3 dispersion correction scheme[3,4] and a geometrical counterpoise correction[2,5] in order to account for the intermolecular and intramolecular interactions and basis set superposition error, respectively. The grid level was chosen as 5 and a tight convergence criteria was selected for the SCF energy calculations, as well as in geometry optimizations.

S1.2 Results and Discussion

Before assessing the bulk phase structure of the different ILs, the chemical properties of the individual amino acid anions will be investigated. To achieve this, the gas phase ESPs were mapped onto the electron density as shown in Figure S1. Thus, the negative charge carried by the anions is located at the deprotonated carboxylic acid group, which makes it prone to acting as hydrogen bond acceptor. Another common feature among the amino acid anions can be observed around the amine group, where the nitrogen atom exhibits an electron excess induced by its lone pair, while the hydrogen atoms show an electron deficit, thus potentially acting as hydrogen bond donor sites. One exception regarding this observation is proline, since the amine group is enclosed in the heterocycle. Although an electron excess and deficit can still be observed at the nitrogen and hydrogen atom, respectively, the charge separation is less pronounced as compared to the other amino acid anions.
When comparing the various amino acid residues, significant differences can be observed in the electron density distribution. The terminal methyl group of $[ala]^-$ is only slightly polarized, with some electron excess and deficit around the carbon and hydrogen atoms, respectively. Therefore, this methyl group is predominantly non-polar and prone for hydrophilic interactions. $[pro]^-$, the only amino acid anion which features a non-aromatic ring, shows a dispersed distribution of the electron density around its pyrrolidine heterocycle.

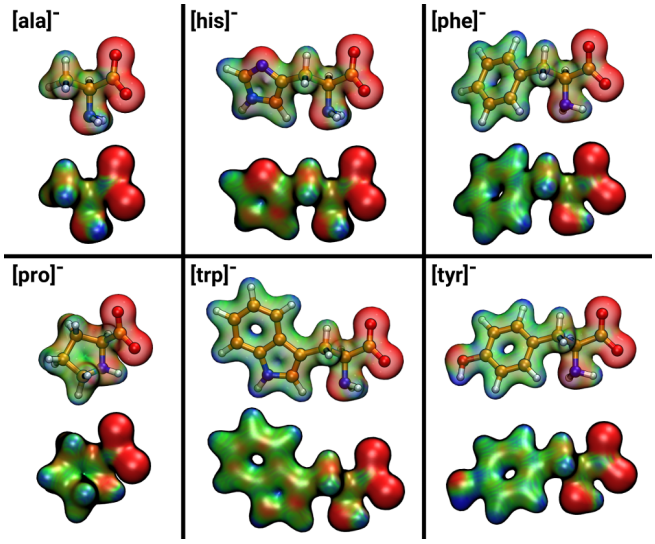

Figure S1: Gas phase electrostatic potentials of the amino acid anions mapped onto the electron density (isosurface value 0.04). The color scale is chosen from -0.1 (blue) to 0.1 (red).

The four aromatic amino acid anions display contrasting electron density distributions around their ring structures, resulting in probable differences with respect to the chemical behaviour. In the case of $[his]^-$ and $[trp]^-$, the two aromatic amino acids featuring heterocycles, the area around the nitrogen atoms exhibits a pronounced negative charge. These can also be supported by CHELPG atomic charges data. Overall, the nitrogen atoms within the ring lowers the π-electron density and thus the aromaticity. Many studies have attempted to gain insight into the aromaticity of a particular heterocycle by comparing its bond lengths with those of related molecules.[6] The Bird index can be easily derived from experimentally determined bond lengths. The utility of this index is reflected in its application to five-membered heterocycles and their mesoionic derivatives. This is also reflected by the Bird indexes of imidazole and indole, which are calculated as 64[6] and 70[7], respectively. For comparison, the Bird index of benzene equals to 100[8] and is chosen as reference. Bird indices smaller than 100 indicate a decreased aromaticity as compared to benzene. Additionally, both anions show a slight negative charge between the C-C bonds within the rings which most likely occurs due to the partial double bond character of the aromatic C-C bonds. The same is observed for $[phe]^-$ and $[tyr]^-$, inasmuch as the C-C bonds within the rings show a slight increase in the electron density. Among the six amino acid anions discussed, $[tyr]^-$ is the only one containing a hydroxyl group. From the electrostatic potential plots, it becomes evident that the hydroxyl oxygen and hydrogen atoms show a pronounced bond donor and acceptor characteristics, respectively. Thus, this additional hydrogen bond interaction site may affect the bulk phase structure significantly.
The CHELPG atomic charges for each atom of the cation and anions are listed in Tables S1–S7, along with the corresponding atom numbers in Figures S2–S8. In the case of anions, the amine nitrogen atoms of the anions always shows the most negative number, even above 1 (except $[pro]^-$, the amine in [pro] is a secondary one). Besides, the carboxylate group carbons and the carbons linked to the nitrogen atoms give more positive data. A significant increase in the electron density can be observed around the ring carbon atom attached to the carboxylate group compared to the other ring carbon atoms. While the hydrogen atoms show decreased electron density, some electron excess is located around the C-C bonds. A significant increase in the electron density can be observed around the ring carbon atom attached to the carboxylate group compared to the other ring carbon atoms in $[C_2C_1im][his]$ and $[C_2C_1im][phe]$.

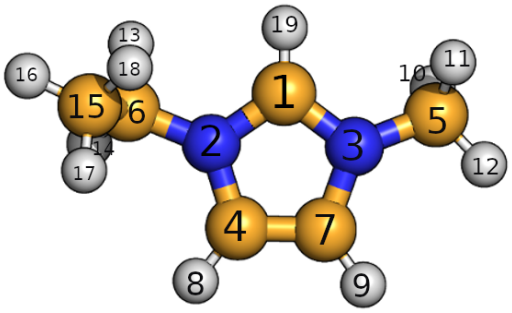

Figure S2: Atomic number of $[C_2C_1im]^+$.

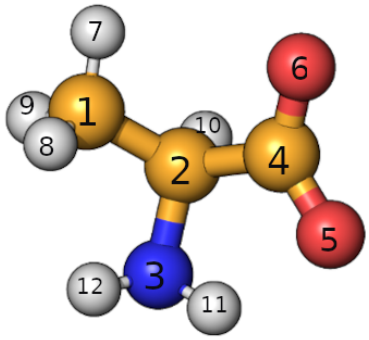

Figure S3: Atomic number of $[ala]^-$.

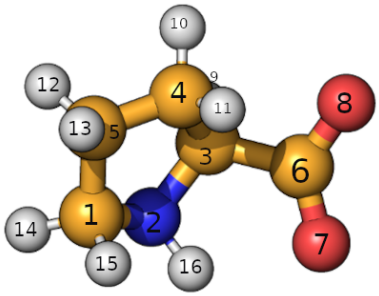

Figure S4: Atomic number of $[pro]^-$.

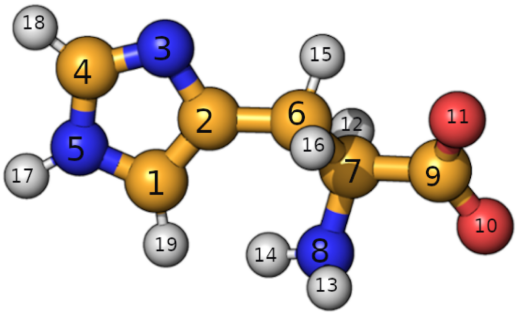

Figure S5: Atomic number of $[his]^-$.

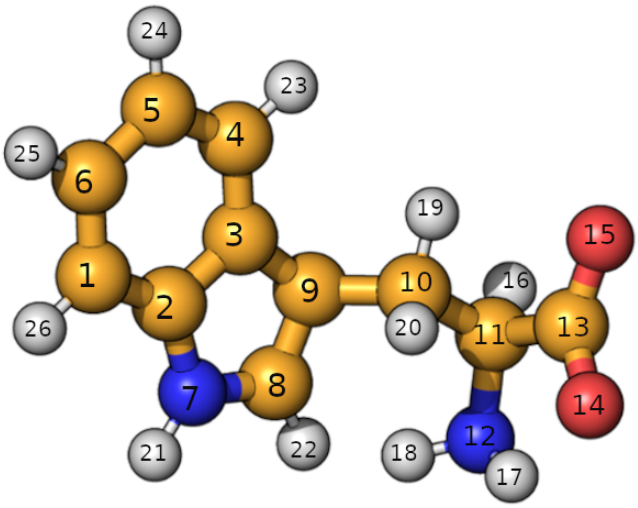

Figure S6: Atomic number of $[trp]^-$.

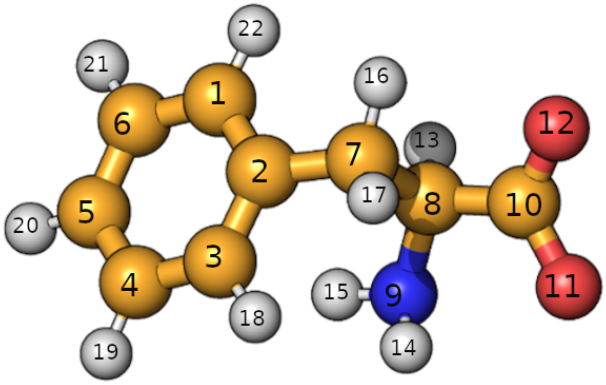

Figure S7: Atomic number of $[phe]^-$.

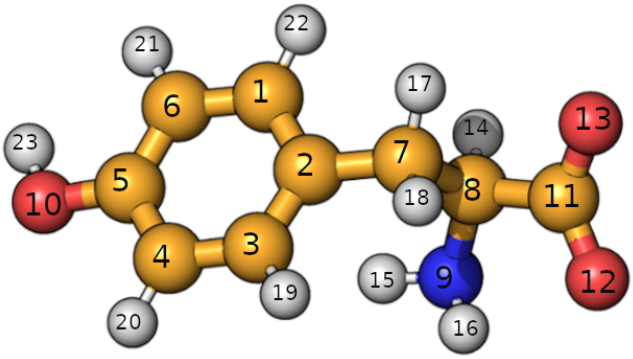

Figure S8: Atomic number of $[tyr]^-$.

Table S1: Partial CHELPG atomic charges of $[C_2C_1im]^+$.

Atomic Number	Atom	Charge
1	C	-0.13
2	N	0.09
3	N	0.31
4	C	-0.21
5	C	-0.44
6	C	0.08
7	C	-0.26
8	H	0.26
9	H	0.26
10	H	0.20
11	H	0.19
12	H	0.19
13	H	0.07
14	H	0.08
15	C	-0.23
16	H	0.11
17	H	0.09
18	H	0.09
19	H	0.25

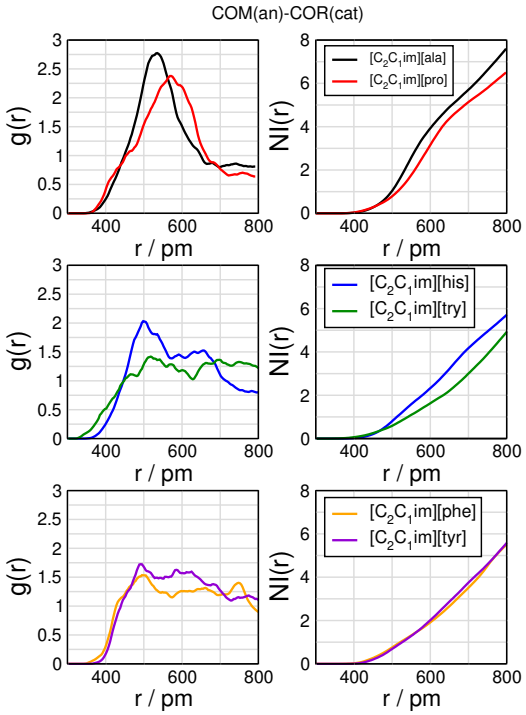

Figure S9: Radial pair distribution functions and number integrals between the center of mass of the anion and the center of ring of the cation. an: anion; cat: cation.

Table S2: Partial CHELPG atomic charges of $[ala]^-$.

Atomic Number	Atom	Charge
1	C	-0.40
2	C	0.66
3	N	-1.03
4	C	0.62
5	O	-0.78
6	O	-0.8
7	H	0.06
8	H	0.10
9	H	0.04
10	H	-0.11
11	H	0.30
12	H	0.33

Table S3: Partial CHELPG atomic charges of $[pro]^-$.

Atomic Number	Atom	Charge
1	C	0.32
2	N	-0.83
3	C	0.25
4	C	0.09
5	C	-0.19
6	C	0.82
7	O	-0.81
8	O	-0.86
9	H	-0.03
10	H	-0.05
11	H	0.01
12	H	0.05
13	H	-0.01
14	H	-0.05
15	H	-0.03
16	H	0.33

Table S4: Partial CHELPG atomic charges of $[his]^-$.

Atomic Number	Atom	Charge
1	C	-0.24
2	C	0.46
3	N	-0.63
4	C	0.20
5	N	-0.43
6	C	-0.33
7	C	0.43
8	N	-1.03
9	C	0.71
10	O	-0.79
11	O	-0.81
12	H	-0.05
13	H	0.33
14	H	0.35
15	H	0.11
16	H	0.10
17	H	0.34
18	H	0.11
19	H	0.18

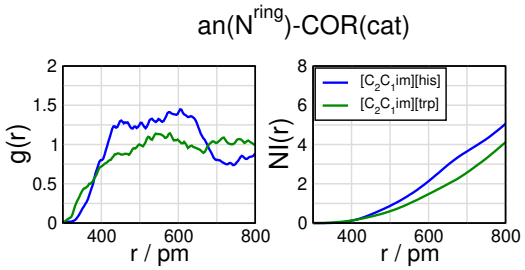

Figure S10: Radial pair distribution functions and number integrals between the ring nitrogen atom of [his] and [trp] which feature a hydrogen atom and the center of ring of the cation.

Table S5: Partial CHELPG atomic charges of $[trp]^-$.

Atomic Number	Atom	Charge
1	C	-0.40
2	C	0.33
3	C	0.15
4	C	-0.25
5	C	-0.24
6	C	-0.13
7	N	-0.58
8	C	0.02
9	C	-0.24
10	C	-0.06
11	C	0.47
12	N	-0.96
13	C	0.64
14	O	-0.77
15	O	-0.80
16	H	-0.06
17	H	0.30
18	H	0.32
19	H	0.04
20	H	0.06
21	H	0.37
22	H	0.14
23	H	0.19
24	H	0.14
25	H	0.13
26	H	0.17

Table S6: Partial CHELPG atomic charges of $[phe]^-$.

Atomic Number	Atom	Charge
1	C	-0.15
2	C	0.10
3	C	-0.14
4	C	-0.17
5	C	-0.18
6	C	-0.19
7	C	-0.20
8	C	0.65
9	N	-0.96
10	C	0.59
11	O	-0.75
12	O	-0.77
13	H	-0.13
14	H	0.30
15	H	0.30
16	H	0.03
17	H	0.06
18	H	0.11
19	H	0.13
20	H	0.12
21	H	0.13
22	H	0.13

Table S7: Partial CHELPG atomic charges of $[tyr]^-$.

Atomic Number	Atom	Charge
1	C	-0.10
2	C	-0.08
3	C	0.05
4	C	-0.55
5	C	0.53
6	C	-0.40
7	C	-0.10
8	C	0.62
9	N	-0.98
10	O	-0.65
11	C	0.59
12	O	-0.75
13	O	-0.78
14	H	-0.11
15	H	0.30
16	H	0.31
17	H	0.02
18	H	0.04
19	H	0.10
20	H	0.19
21	H	0.20
22	H	0.14
23	H	0.41

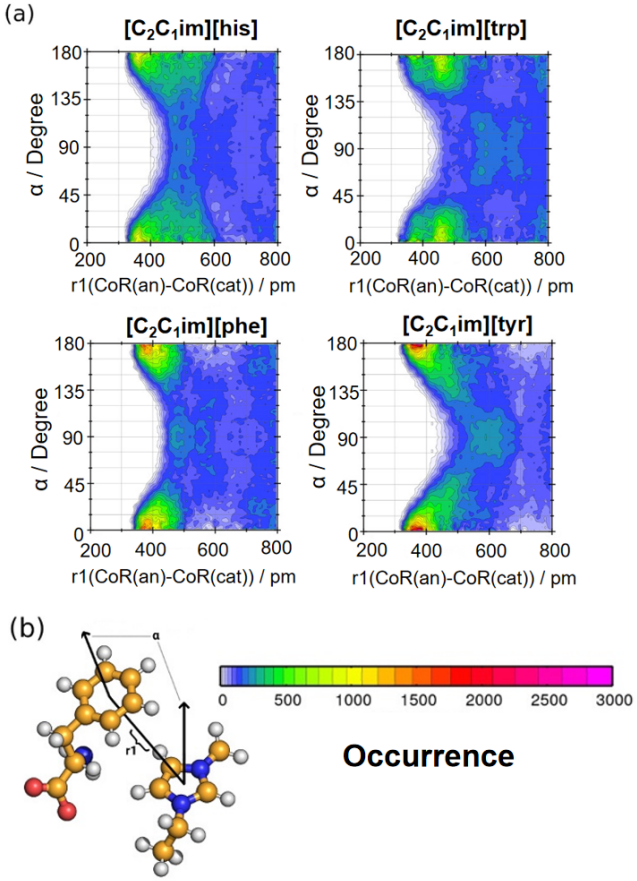

Figure S11: (a) Combined distribution functions correlating the distance between the center of ring of the anion and the center of ring of the cation with the angle between the ring normal vectors of cation and anion. (b) A representation of the interaction in a ball-and-stick model.

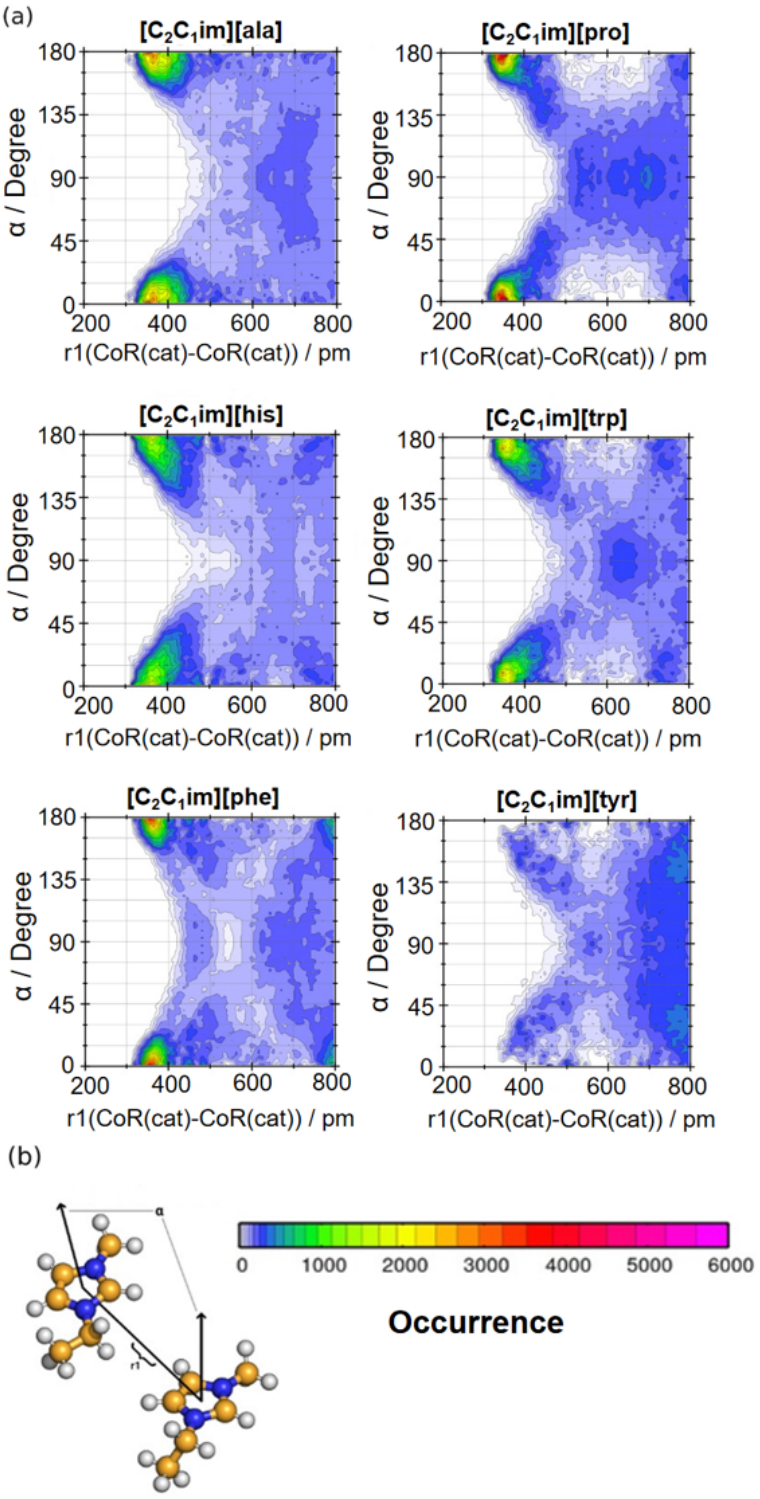

Figure S12: (a) Combined distribution functions correlating the distance between the centers of ring of two cations with the angle between the ring normal vectors of both cations. (b) A representation of the interaction in a ball-and-stick model.

Table S8: The r range values, maximum distances, the g(r) values and the integral number on the g(r)max of the first peaks of the first peaks from the radial distribution functions for four kinds of HB: i) between the carboxylate group oxygen atoms of the anion and the ring hydrogen atoms of the cation; ii) between the amine group nitrogen atom of the anion and the ring hydrogen atoms of the cation; iii) between the carboxylate group oxygen atoms of the anion and the amine group hydrogen atoms of the anion; iv) between the ring hydrogen atoms of the cation and the ring nitrogen atom of $[his]^-$ which does not feature a hydrogen atom.

ion pair	range/pm,(rmax, g(r)max/pm),[NI]			
	an(O^{CO_2})-cat(H^{ring})	an(N^{NH_2})-cat(H^{ring})	an(O^{CO_2})-cat(H^{NH_2})	an(N^{ring})-cat(H^{ring})
$[C_2C_1im][ala]$	160< *r* <300(205, 2.9),[0.4]	170< *r* <280 (228, 1.0),[0.2]	160< *r* <280(215, 1.0),[0.1]	
$[C_2C_1im][pro]$	160< *r* <300(205, 3.9),[0.5]			
$[C_2C_1im][his]$	160< *r* <300(208, 3.2),[0.3]			170< *r* <350(232, 1.25),[0.1]
$[C_2C_1im][trp]$	160< *r* <300(198, 3.2),[0.3]	170< *r* <260(228, 1.2),[0.2]	160< *r* <280(208, 1.1),[0.1]	
$[C_2C_1im][phe]$	160< *r* <300(208, 3.7),[0.3]	170< *r* <260(238, 1.2),[0.2]	160< *r* <280(218, 0.9),[0.1]	
$[C_2C_1im][tyr]$	160< *r* <300(222, 2.0),[0.2]	170< *r* <300(228, 1.3),[0.3]	160< *r* <300(218, 0.8),[0.1]	

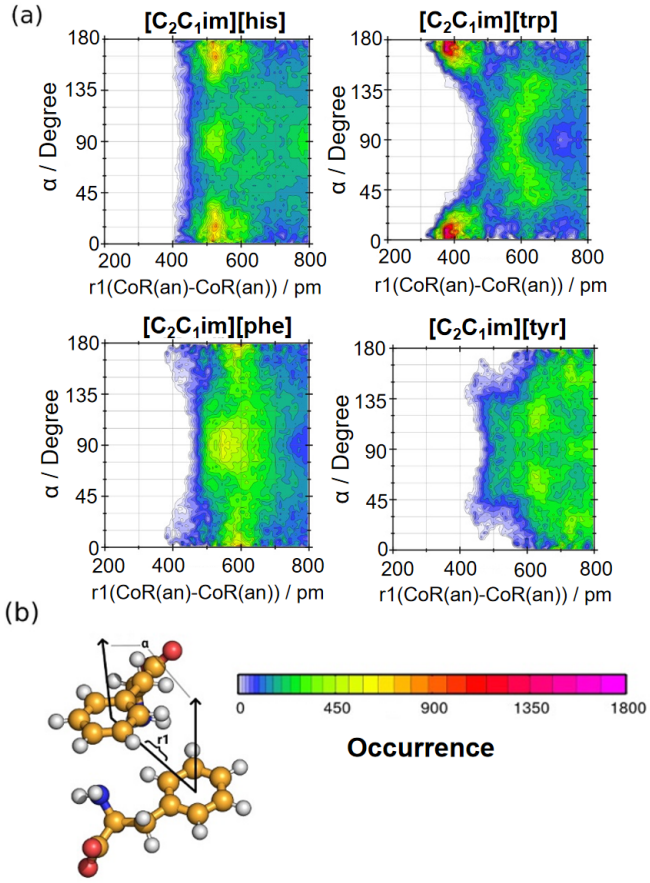

Figure S13: (a) Combined distribution functions correlating the distance between the centers of ring of two anions with the angle between the ring normal vectors of both anions. (b) A representation of the interaction in a ball-and-stick model.

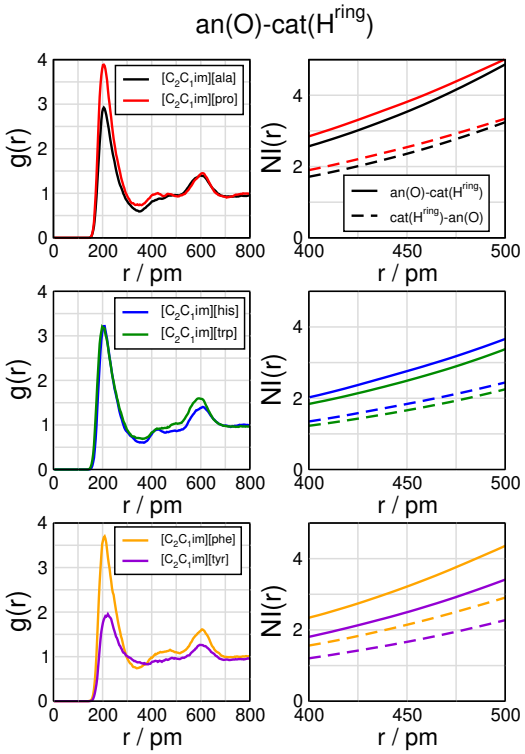

Figure S14: Radial pair distribution functions and number integrals between the carboxylate group oxygen atoms of the anion and the ring hydrogen atoms of the cation.

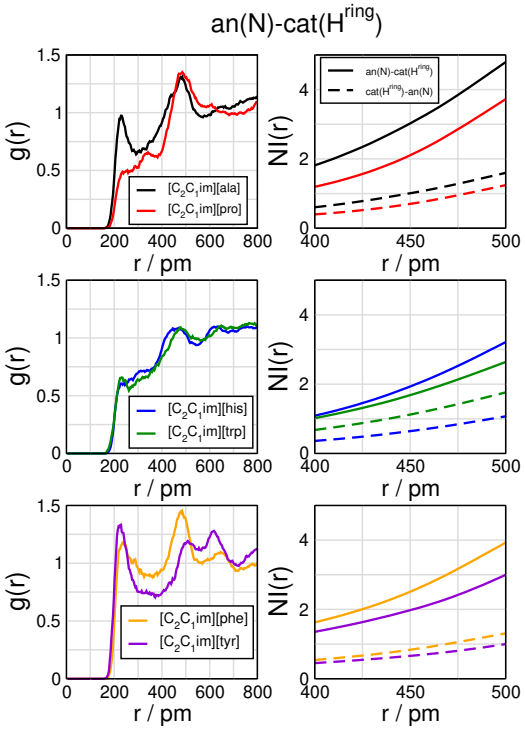

Figure S15: Radial pair distribution functions and number integrals between the amine group nitrogen atom of the anion and the ring hydrogen atoms of the cation.

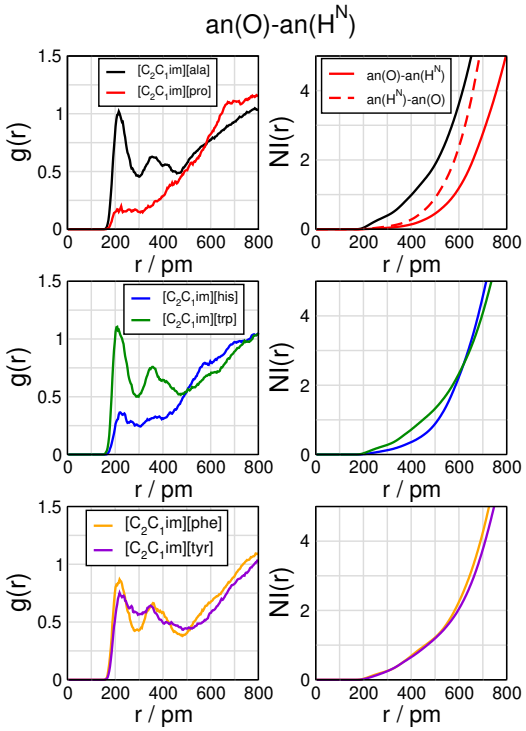

Figure S16: Radial pair distribution functions and number integrals between the carboxylate group oxygen atoms of the anion and the amine group hydrogen atoms of the anion.

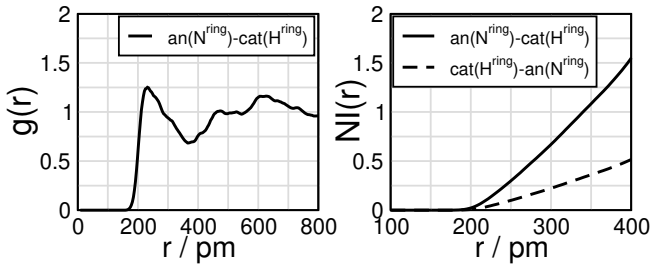

Figure S17: Radial pair distribution functions and number integrals between the ring hydrogen atoms of the cation and the ring nitrogen atom of $[his]^-$ which does not feature a hydrogen atom.

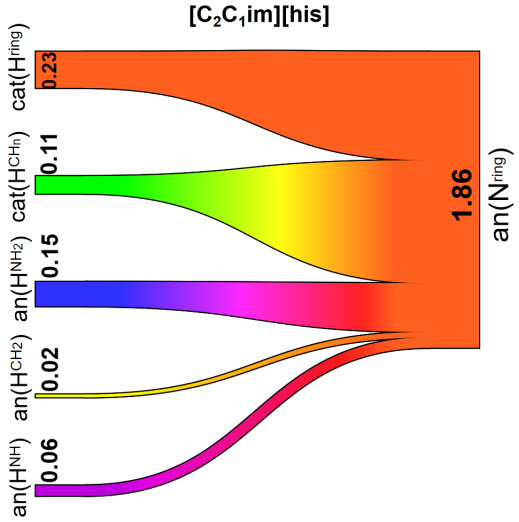

Figure S18: Linear Sankey diagram showing the hydrogen bond topology for $[C_2C_1im][his]$. The labels in the diagram correspond to the following HB donor and acceptor sites: cat(H^{ring}) are the hydrogen atoms in the $[C_2C_1im]^+$ ring; cat(H^{CHn}) are the hydrogen atoms in the CHn groups of the $[C_2C_1im]^+$; an(H^{NH2}) are the hydrogen atoms in NH_2 group of [his]; an(H^{CH2}) are the hydrogen atoms in the chain of the [his]; an(H^{NH}) is the hydrogen atom in NH group of the [his] ring and an(N^{ring}) is the nitrogen atom on the [his] ring without hydrogen.

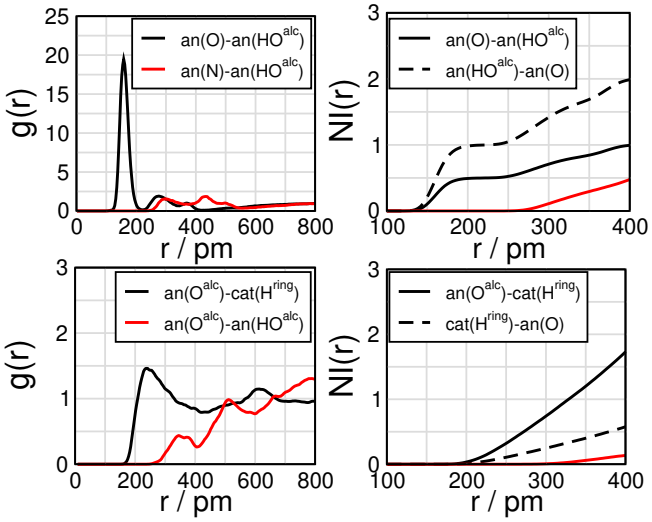

Figure S19: Radial pair distribution functions and number integrals between the carboxylate group oxygen atoms and the hydrogen atom of the alcohol group of the $[tyr]^-$ anion (top); between the amine group nitrogen atom and the hydrogen atom of the alcohol group of the $[tyr]^-$ anion (top); between the alcohol group oxygen atom of the $[tyr]^-$ anion and the ring hydrogen atoms of the cation (bottom); between the alcohol group oxygen atom and the alcohol group hydrogen atom of the $[tyr]^-$

References

(1) Neese, F. The ORCA program system. *WIREs Comp. Mol. Sci.* **2012**, *2*, 73–78.

(2) Grimme, S.; Brandenburg, J. G.; Bannwarth, C.; Hansen, A. Consistent structures and interactions by density functional theory with small atomic orbital basis sets. *J. Chem. Phys.* **2015**, *143*, 054107.

(3) Grimme, S.; Antony, J.; Ehrlich, S.; Krieg, H. A consistent and accurate ab initio parametrization of density functional dispersion correction (DFT-D) for the 94 elements H-Pu. *J. Chem. Phys.* **2010**, *132*, 154104.

(4) Grimme, S.; Ehrlich, S.; Goerigk, L. Effect of the damping function in dispersion corrected density functional theory. *J. Comput. Chem.* **2011**, *32*, 1456–1465.

(5) Kruse, H.; Grimme, S. A geometrical correction for the inter-and intra-molecular basis set superposition error in Hartree-Fock and density functional theory calculations for large systems. *J. Chem. Phys.* **2012**, *136*, 04B613.

(6) Bird, C. A new aromaticity index and its application to five-membered ring heterocycles. *Tetrahedron* **1985**, *41*, 1409–1414.

(7) Bird, C. The application of a new aromaticity index to some bicyclic heterocycles. *Tetrahedron* **1987**, *43*, 4725–4730.

(8) Bird, C. The application of a new aromaticity index to six-membered ring heterocycles. *Tetrahedron* **1986**, *42*, 89–92.

Acknowledgements

Ich möchte meinen Eltern und Freunden für ihre bedingungslose Unterstützung und Ermutigung danken. Mein aufrichtiger Dank gilt auch Prof. Dr. Babara Kirchner, Prof. Dr. Thomas Bredow, Prof. Dr. Connie C. Lu, und Priv.-Doz. Dr. Gregor Hagelüken für ihre Zeit und wertvollen Rückmeldungen. Ein besonderer Dank geht an meine Kolleginnen und Kollegen für ihre Zusammenarbeit und Unterstützung während meiner Forschungszeit.
Mein tief empfundener Dank gilt außerdem meiner Betreuerin, Prof. Dr. Babara Kirchner, die mir geholfen hat, eine größere Welt zu entdecken. Schließlich danke ich meinen beiden Katzen, Pepsi und Coco, die mich mit ihrer Gesellschaft durch diese Zeit begleitet haben.